



저작자표시-비영리-변경금지 2.0 대한민국

이용자는 아래의 조건을 따르는 경우에 한하여 자유롭게

- 이 저작물을 복제, 배포, 전송, 전시, 공연 및 방송할 수 있습니다.

다음과 같은 조건을 따라야 합니다:



저작자표시. 귀하는 원저작자를 표시하여야 합니다.



비영리. 귀하는 이 저작물을 영리 목적으로 이용할 수 없습니다.



변경금지. 귀하는 이 저작물을 개작, 변형 또는 가공할 수 없습니다.

- 귀하는, 이 저작물의 재이용이나 배포의 경우, 이 저작물에 적용된 이용허락조건을 명확하게 나타내어야 합니다.
- 저작권자로부터 별도의 허가를 받으면 이러한 조건들은 적용되지 않습니다.

저작권법에 따른 이용자의 권리는 위의 내용에 의하여 영향을 받지 않습니다.

이것은 [이용허락규약\(Legal Code\)](#)을 이해하기 쉽게 요약한 것입니다.

[Disclaimer](#)

공학박사학위논문

텅스텐 및 텅스텐 복합재의
열화학적 삭마 모델 개발

Development of a Thermochemical Ablation
Model for Tungsten and Tungsten Composites

2019년 8월

서울대학교 대학원

기계항공공학부

노성준

텅스텐 및 텅스텐 복합재의 열화학적 삭마 모델 개발

Development of a Thermochemical Ablation
Model for Tungsten and Tungsten Composites

지도 교수 김 규 홍

이 논문을 공학박사 학위논문으로 제출함
2019 년 5 월

서울대학교 대학원
기계항공공학부
노 성 준

노성준의 공학박사 학위논문을 인준함
2019 년 6 월

위 원 장 _____ (인)

부위원장 _____ (인)

위 원 _____ (인)

위 원 _____ (인)

위 원 _____ (인)

Abstract

Development of a Thermochemical Ablation Model for Tungsten and Tungsten Composites

Sungjun Noh

School of Mechanical and Aerospace Engineering

The Graduate School

Seoul National University

In order to develop an ablation model for tungsten and tungsten composites in high temperature environment supposed hypersonic flight and rocket nozzle, in which oxidation causes the ablation mainly, ablation tests on pure tungsten and tungsten composite specimens were conducted in a 150-kW arc heater.

For pure tungsten, ten different flow conditions were tested, then changes in length and mass of the specimens were measured after the tests. Changes in shape of the specimen due to ablation were captured during the experiment by a high-speed camera, from which the recession rate over time was calculated.

For tungsten composites specimens, HfC and ZrC were used as a reinforcement. W-HfC and W-ZrC with various contents of the reinforcements was tested in the same test condition, and the increase of ablation resistance by adding the reinforcement was investigated.

A numerical simulation on the test conditions was performed by an axi-symmetric non-equilibrium flow solver to calculate surface heat transfer rate and species mass fraction which could not be measured by the experiment because of the limitations of the arc heater facility. In addition, the numerical simulation was used to investigate

the effects of shape changes, particularly position and radius of the specimen, on heat transfer rate during the test. The study confirmed that the change in shape of the specimen alone could reduce the stagnation point heat transfer rate by approximately 35% during the test.

Finally, a thermochemical ablation model and an ablation analysis program for tungsten which consist of a non-equilibrium flow solver coupled with a solid thermal response solver were developed. The program simulated the ablation test result of pure tungsten decently, including the stagnation point recession rate and the shape changes of the specimen over time.

Keyword : Tungsten, Ablation, Oxidation, Arc Heater, CFD
Student Number : 2012-30169

Table of Contents

Abstract	i
Table of Contents	iii
List of Figures	iv
List of Tables	vi
Chapter 1. Introduction	1
1.1 Tungsten	1
1.2 Related Researches on Tungsten Ablation	3
1.3 Motivation	6
Chapter 2. Ablation Experiments	10
2.1 Experimental Setup	10
2.2 Ablation Test with Pure Tungsten Specimens	14
2.3 Ablation Test with W-HfC Specimens	27
2.4 Ablation Test with W-ZrC Specimens	33
Chapter 3. Numerical Approach	40
3.1 Flow Governing Equation	40
3.2 Solid Governing Equation	47
3.3 Ablation Model	48
3.4 Numerical Schemes	61
Chapter 4. Numerical Results	66
4.1 Non-equilibrium flow solver validation	66
4.2 Numerical calculation on ablation test conditions	73
4.3 Parametric study on ablation test conditions	79
4.4 Simulation of Tungsten Ablation	90
Chapter 5. Conclusion	100
Appendix	103
A. Coefficients for non-equilibrium reaction rates.	103
B. Milikan and White coefficients for vibrational relaxation	110
C. Transport properties for each species	111
References	113
국문초록	118

List of Figures

Fig. 1 Tungsten applications against high enthalpy environment.....	1
Fig. 2 Ablation mechanism of Tungsten	2
Fig. 3 Schematic flow chart of the 150-kW arc heater facility	10
Fig. 4 Schematic of tungsten ablation test.	10
Fig. 5 Schematic of tungsten specimen	11
Fig. 6 Picture of tungsten ablation test captured by a video camera.....	12
Fig. 7 Cross section of flat-ended specimens after ablation test.	13
Fig. 8 Tungsten test specimens.	16
Fig. 9 High-speed camera images for 5 s intervals (Run3).....	17
Fig. 10 High-speed camera images for 5 s intervals (Run6).....	17
Fig. 11 High-speed camera images for 5 s intervals (Run9).....	18
Fig. 12 Recession rate Base cases	19
Fig. 13 Extraction of surface line and stagnation point (Run6).....	20
Fig. 14 Stagnation point recession versus time.	21
Fig. 15 Stagnation point recession rate versus time.....	21
Fig. 16 Mass reduction rate and recession rate (VM and VC cases)	25
Fig. 17. Mass reduction rate and recession rate by distance (Dist cases)	26
Fig. 18 W-HfC specimens after ablation tests	28
Fig. 19 Ablation depth versus time against different HfC contents	28
Fig. 20 Increment of ablation resistance by increasing HfC vol%	29
Fig. 21 X-ray diffraction after ablation test of W-HfC specimens.....	30
Fig. 22 Surface microstructure of W-HfC specimens after the ablation test	31
Fig. 23 EDS analysis result of the surface microstructure of W-HfC specimens	32
Fig. 24 Recession of various W-ZrC/HfC samples after ablation test.	34
Fig. 25 XRD patterns after the ablation test on various composites.....	35
Fig. 26 FE-SEM images of ablated surface (left : SE / right : BSE mode).....	36
Fig. 27 FE-SEM images of cross-sections of the specimens.	38
Fig. 28 Mass balance at wall	49
Fig. 29 Graphs of the oxidation probability functions with different coefficients.....	56
Fig. 30 Energy balance at wall	57
Fig. 31 Points used to calculate the temperature gradient at the surface	59
Fig. 32 Iteration strategy of the ablation solver	62
Fig. 33 Flow chart of SAGT	64
Fig. 34 Grid deformation process of SAGT	65
Fig. 35 SAGT applied during an ablation calculation	65
Fig. 36 Initial grid system for Gokcen's case	67
Fig. 37 Translational and rotational temperature along the centerline.....	67
Fig. 38 Mass fraction of oxygen along the centerline.....	68
Fig. 39 Surface heat transfer rate.....	68
Fig. 40 Grid system for Suzuki case.....	70
Fig. 41 Pressure contour in original grid (left) and SAGT applied grid (right)	70
Fig. 42 Heat transfer distribution along the surface.....	71
Fig. 43 The net heat flux at stagnation point along time.	72
Fig. 44 Surface recession at t = 30 sec.	72

Fig. 45 Grid systems for heat transfer rate calculation.....	73
Fig. 46 Density distribution and streamlines (Base1).....	76
Fig. 47 Pressure distributions around the specimen (Base1).....	76
Fig. 48 Heat transfer rate at the surface in different test cases.....	77
Fig. 49 Recession rate versus stagnation point heatflux.....	77
Fig. 50 Mass ablation rate versus stagnation point heatflux.....	77
Fig. 51 Mass fraction of O along the centerline.....	80
Fig. 52 Heat transfer rate along surface line on 300 K fully and non-catalytic surface.....	81
Fig. 53 Stagnation point heat transfer rate versus surface temperature.....	82
Fig. 54 Stagnation point heat transfer rate versus oxidation coefficient.....	83
Fig. 55 Shape parameters for different grid systems.....	84
Fig. 56 Stagnation point heat transfer rate versus specimen distance.....	85
Fig. 57 Pressure distribution along the center line for different distances.....	85
Fig. 58 Mach number distribution along the center line for different distances.....	86
Fig. 59 Stagnation point heat flux versus nose radius of the specimen.....	87
Fig. 60 Stagnation point heat flux versus inverse root of nose radius.....	88
Fig. 61 Grids near the specimen with different shape.....	89
Fig. 62 Grid systems for ablation calculation.....	90
Fig. 63 Grid system of solid specimen (skip=4).....	91
Fig. 64 Pressure contour on whole region (Base1).....	92
Fig. 65 Mach number contour on whole region (Base1).....	92
Fig. 66 Centerline mass fraction at different time steps (Base1).....	93
Fig. 67 Pressure contours around specimen over time.....	94
Fig. 68 Calculated specimen shapes and internal temperatures over time.....	96
Fig. 69 Calculated stagnation point heat flux and temperature versus time.....	97
Fig. 70 Calculated mass flow rate at stagnation point versus time.....	97
Fig. 71 Calculated pressure contours and high speed camera images (Base1).....	99
Fig. 72 Calculated pressure contours and high speed camera images (Base2).....	99
Fig. 73 Calculated pressure contours and high speed camera images (Base3).....	99

List of Tables

Table 1 Specification of 150 kW arc heater.....	11
Table 2 Experimental condition of Base cases	14
Table 3 Ablation test results of Base cases	18
Table 4 Experimental condition VM and VC cases.....	23
Table 5 Ablation test results of VM and VC cases	24
Table 6 Experimental conditions of Dist cases	25
Table 7 Contents of W-HfC composites	27
Table 8 Samples for tungsten composite ablation test	33
Table 9 Surface reactions.....	48
Table 10 Freestream flow conditions of the 7.2 MJ/kg arc jet.....	66
Table 11 Freestream condition of Suzuki case	69
Table 12 Heater chamber conditions and stagnation point pressure	74
Table 13 Heater chamber conditions calculated by equilibrium assumption.....	75
Table 14 Flow conditions at the center of nozzle exit	79

Chapter 1. Introduction

1.1 Tungsten

Tungsten is a refractory metal with remarkable heat resistance and mechanical properties. Due to its high melting point (3,695K), tungsten, and its composites, is used as a thermal protection material in extreme-temperature aerospace applications, such as heat shield of hypersonic vehicle and projectile, inner surface of rocket engine nozzle, and gas turbine engine rotor blades, where both heat resistance and mechanical properties are critical requirements [1-6].

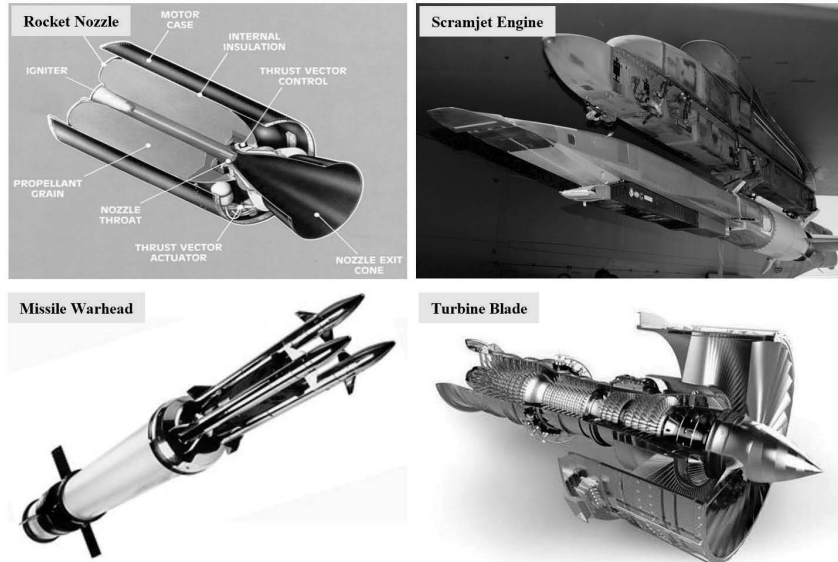


Fig. 1 Tungsten applications against high enthalpy environment.

However, when exposed to oxygen at high temperatures, tungsten undergoes oxidation. Tungsten oxides melt and evaporate at much lower temperatures than pure tungsten, causing degradation of mechanical properties and heat resistance characteristics, and consequently mass loss due to surface ablation.

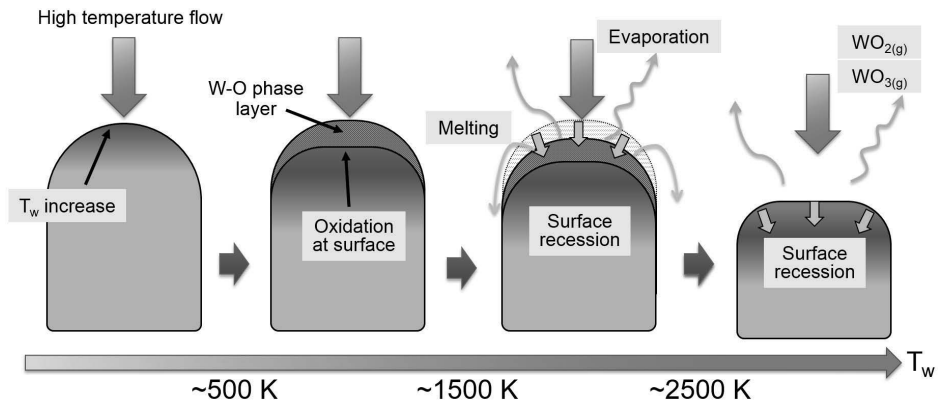


Fig. 2 Ablation mechanism of tungsten.

The mechanism of tungsten surface ablation in a high enthalpy flow changes with surface temperature among other parameters. At temperature regimes below 1,500K, the gas species react with the surface of tungsten to form condensed products, mostly oxides. These condensed-phase oxides settle on the tungsten surface form a thin layer suppresses further oxidation—a phenomenon called passive oxidation. As surface temperature increases, the upper oxide layer begins to melt, and liquid-phase oxides flow along the surface while condensed-phase oxides form inside.

When the surface temperature increases further above 2,000 K, the condensed-phase oxide layer evaporates and volatile oxides begin to form directly—a phenomenon called active oxidation. This in turn causes the continuous mass loss of tungsten. At the beginning of this temperature regime, ablation rate increases as the reaction rate increases with temperature. As the temperature increases further, ablation rate is controlled by the rate of diffusion, which transports the reactants and products to the boundary layer from the surface. Finally, as the surface temperature reaches the melting point of tungsten—approximately 3,695 K—ablation proceeds rapidly due to melting.

1.2 Related Researches on Tungsten Ablation

Since the mechanism varies with temperature range, tungsten ablation characteristics have been studied with various methods, categorized by applications and heat flux regimes. These methods include ablation test using arc heaters and oxyacetylene torches, filaments test, and thermogravimetric analysis (TGA).

Arc heaters

Several researchers conducted ablation tests on pure tungsten with arc heaters. [7-12] For instance, Auerbach conducted ablation tests in the Sandia 2 MW and McDonnell Douglas HIP arc-heated-jet facilities [7]. The stagnation pressure range and enthalpy range used in the test were 2.2–17.9 MPa and 4.63–5.89 MJ/kg, respectively. Solid, porous, and copper-infiltrated tungsten, non-tungsten metal carbide composites, and ATJ-S-grade graphite were tested as ablative materials. The test found that the ablation performance of those metals is proportional to the melting point of the material—a result of using melting as the major component in ablation mechanism.

In a similar study, Moody et al. performed ablation tests on tungsten and molybdenum for atmospheric re-entry applications using low/high pressure arc jet (stagnation pressure of 7 / 6,000–10,000 kPa) and ballistic range facility, and then compared the results with those obtained from a computer program developed for the purpose at that time [8, 9]. The program simulated the experimental results well. However in all the three experiments, the major ablation mechanism was melting.

Sherman and Schutzler conducted an ablation test for various nose-cone designs through segmented concept using an AFFDL 50 MW arc heater, with a stagnation point pressure of 7,600 kPa and an enthalpy of 14 MJ/kg [10]. The time frame of the test was less than two seconds. Since the above studies were conducted with extremely high enthalpy flow facilities to simulating hypersonic and re-entry flow regimes, the main ablation process in these experiments again was dominated by

melting, and only momentarily by chemical reactions.

Recently in Korea, 400 kW plasma wind tunnel and 55 kW vacuum plasma spraying facilities were constructed, and ablation properties of tungsten coated materials were tested with those facilities [11]. After the test, microstructure of the test specimen was investigated. Thermal ablation occurred prominently on the specimen without tungsten (W) coating, while only cracks and pores in W layer was observed and ablation was suppressed by the W layer on the coated specimen.

Oxyacetylene torches

Oxyacetylene torch is also one of the widely used ablation test facility since it is easy to operate, relatively inexpensive, and provide quantitative and reproducible results. Various research on ablation of tungsten and its composites have been conducted with oxyacetylene torches [13-18]. Since the combustion products of an oxyacetylene torch more closely resemble the environment generated in rocket motors, this test method is more applicable to screening materials for rocket nozzles and liners than for aerodynamic heating [19]. Therefore, studies have been conducted using this equipment to investigate the ablation performance of various materials including tungsten composites and coatings. Guo et al. investigated ablation performance of supersonic atmosphere plasma sprayed tungsten coating under oxyacetylene torch and plasma torch [13]. The tungsten coating protected C/C composites successfully for 60 s under heat flux of 2.4 MW/m², however erosion by oxidation destroyed the coating and led to final failure when the heat flux of oxyacetylene torch raised to 4.2 MW/m². While in plasma ablation test with argon for working gas, W coating successfully protected the substrate above the 40 s in much higher temperature and scouring force than those of oxyacetylene torch, due to the absence of oxidation.

Lee et al. investigated the effect of hafnium carbide (HfC) particles on the ablation resistance of HfC-W composites using an oxyacetylene torch [14]. This experiment confirmed that the addition of HfC particles improves ablation resistance remarkably.

The mass ablation rate of the HfC-W composite with 30 vol% loading of HfC particles was 6.7 times smaller than that of monolithic tungsten. Similarly, Umer et al. investigated the effect of zirconium nitride (ZrN) particles on the ablation resistance of ZrN-W composites [15]. The ablation resistance increased with an increasing volume fraction of ZrN. In particular, the effect was significant when the content of ZrN particles was 30 vol%; that concentration of ZrN was sufficient to cover the entire surface of the specimen with the oxide film.

Wang et al. investigated ablation properties of tungsten-zirconium carbide (W-ZrC) composites with W contents from 48 to 68 vol% using oxyacetylene torch [16]. Ablation resistance is remarkably influenced by W contents in the composite and when the W contents are less than 50 vol%, the composite is prone to crack during the initial heating.

Filament tests and TGA

A study on surface ablation of tungsten by chemical reactions in a temperature range below its melting point was conducted with equipment other than arc heater [20-29]. Various researchers conducted tungsten filament test to figure out reaction kinetics at its surface. Batty and Stickney had proposed a theoretical model for the determination of tungsten oxidation rate, which used reaction probability function and the impingement rate of oxygen molecules derived from a tungsten filament experiment under low pressure conditions ($6.0 \times 10^{-5} < P_{O_2} < 1500$ Pa) [21]. Harvey measured the rate of volatilization of tungsten wires by high-temperature oxidation in O₂-Ar mixture, which contained 20–150 ppm O₂ at a total pressure of 80 kPa [22]. In a more recent study, Sabourin and Yetter conducted a thermogravimetric analysis (TGA) to study the heterogeneous reaction of tungsten at the surface of a rocket nozzle subjected to oxidizing gas species such as CO₂, H₂O, and CO [23]. The gas total pressure for the analysis was approximately 100 kPa. The partial pressure of reactants, on the other hand, was 1 kPa or less as in the filament tests.

1.3 Motivation

In order to increase the availability of tungsten in high temperature applications, it is necessary to understand the ablation characteristics of tungsten and predict the ablation accurately. In those high temperature applications where tungsten or tungsten composites are used,—except the extremely high enthalpy application such as the re-entry or Tokamak—the most problematic phenomena is thermochemical ablation. Therefore, thermochemical ablation, which is mainly caused by oxidation, should be understood and modeled adequately in order to increase the availability of tungsten in high temperature applications.

In this situation, we tried to develop thermochemical ablation models of tungsten and its composites which can simulate and predict ablation amount by high enthalpy flows. To do this, ablation data coupled with accurate flow values applied to the tungsten surface were needed. Especially, the amount of heat transfer rate and partial pressures of chemical species causing surface reactions were essential. The surface temperature during the test should coincide with the range where the ablation rate is dominated by chemical reactions.

As mentioned above, ablation characteristics of tungsten by high enthalpy flows have been investigated in different temperature ranges with various experimental methods. However, those precedent researches are rather insufficient to be used for development of a thermochemical ablation model considering actual environment of the high enthalpy applications for tungsten. First, early studies using arc heaters were more focused on the melting of tungsten than thermochemical ablation, since the main application at that time was TPS for the reentry vehicles. Those arc heaters for re-entry simulations generated extremely high enthalpy flow, so that melting was the main mechanism of the ablation; thermochemical ablation only appeared momentarily.

Meanwhile, researches using oxyacetylene torches are mostly focused on the material response and properties at microstructure level. The flow parameters such

as heat fluxes and species mass fractions incident on the surface and the effect of surface reactions were not analyzed precisely. In addition, in the above papers, an ablation rate was calculated by simply dividing the total ablation amount by the test time. However, in order to develop an ablation model including surface chemistry, the ablation rate should be measured with respect to time. Moreover, many other parameters such as surface temperatures, mass fractions of the chemical species, and heat fluxes at the surface should also be considered over time to find and analyze the correlations between the parameters and the ablation rate.

In the filament tests, the research groups were able to measure the reaction rate of tungsten for specific oxidizing species. However, most of the experiments were carried out under very low reactant partial pressures in order to prevent the diffusion rate of reactants or products from affecting or limiting the ablation rate. In this diffusion-free condition, the ablation rate of tungsten and the reaction speed at the surface increased with temperature. In practical applications, however, the pressure applied at the surface is much greater than that applied in experimental conditions. This leads to the conclusion that the ablation rate is limited by diffusion rate [30]. Moreover, in order to develop an ablation model that could predict and describe the ablation rate of tungsten in a high enthalpy flow regime, the experimental data that could validate ablation rate in a high enthalpy flow are required. In order to obtain the data, an ablation test with pressure values, relatively higher than those in a filament test, was needed.

In this study, to obtain the data needed to develop an ablation model, the ablation rate of tungsten and tungsten composites exposed to high temperature and high pressure flow regimes has been investigated. A 150-kW arc heated jet was used to test several specimens made of tungsten and tungsten composites. Here, oxidation was the primary cause of ablation and the effects of diffusion were pronounced. These conditions are closer to the real conditions of tungsten applications in practical hypersonic re-entry flow regimes in aerospace. The ablation data were successfully

obtained from the experiment. However, since this facility is relatively small, it faces limitations, namely difficulty in measuring surface heat flux and species composition at the surface. The flow conditions could also not be measured directly because of the size limit of the facility and measuring devices.

When conducting ablation tests, measuring the rate of surface heat transfer and partial pressure of reacting species, or mass fraction, is important; these are primary parameters that determine the ablation characteristics. However, because the temperature conditions of the flow regime are extreme—generally over 3,000 K after shock—measuring the flow properties during the test poses several challenges, especially when the facility is small.

For example, under high temperature conditions, a typical non-cooling-type heat flux gauge can measure heat flux into the specimen only for the first few seconds. Furthermore, since the heat flux at the stagnation point increases with the decrease in nose radius of the specimen [31], measuring the heat transfer rate in a small facility poses technical difficulties since the specimen or the gauge should also be small. Although a cooling-type heat flux gauge can cover the longest test time, unless the size of the facility is large enough, securing space for an inner cooling system inside the measuring equipment is not possible.

Measurements of stagnation pressure and mass fractions face similar technical difficulties for the same reasons. Gas compositions in front of the specimen can be estimated by optical methods. These optical measurement methods, however, have resolution limits. Therefore, if the facility size is small, the species composition determined by optical methods will be significantly different from the real composition. Furthermore, when ablation occurs, it is difficult to focus the target point of measurement, as the stagnation point constantly recedes over time.

For these reasons, studies to quantify and predict the flow conditions in the experimental devices numerically have been conducted. Recently, a CFD model was developed at NASA Langley Research Center for the arcjet nozzle and the freejet

portion of the flowfield in a Hypersonic Materials Environment Test System (HYMET), for improving test capabilities and knowledge of the test article environment [32]. By assuming a parabolic form of enthalpy profile at the plenum, it was possible to predict nozzle inlet condition. After this the flowfield from the nozzle to the calibration probe was calculated with a non-equilibrium CFD. Through iterative analysis, stagnation point pressure and bulk enthalpy were obtained and compared to the measured data.

Similarly, in this study, those limitations in 150-kW arc heater facility were surpassed through rigorous computer simulations of flow conditions and other parameters that were difficult to measure during the experiment. Through the simulation, the parameters needed to develop an ablation model such as the rate of heat transfer and gas species composition of the flow applied to a specimen were calculated successfully. Finally, with the help of those computer simulations with the 150-kW arc heater tests, thermochemical ablation model of tungsten was suggested.

Chapter 2. Ablation Experiments

2.1 Experimental Setup

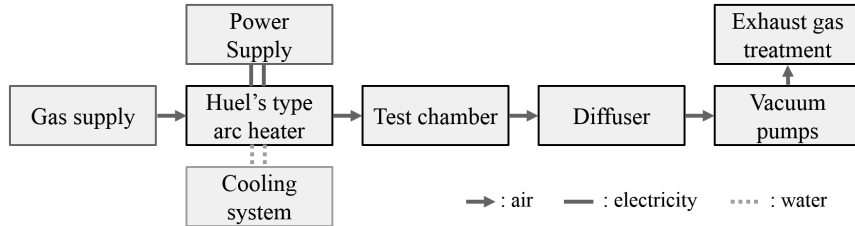


Fig. 3 Schematic flow chart of the 150-kW arc heater facility.

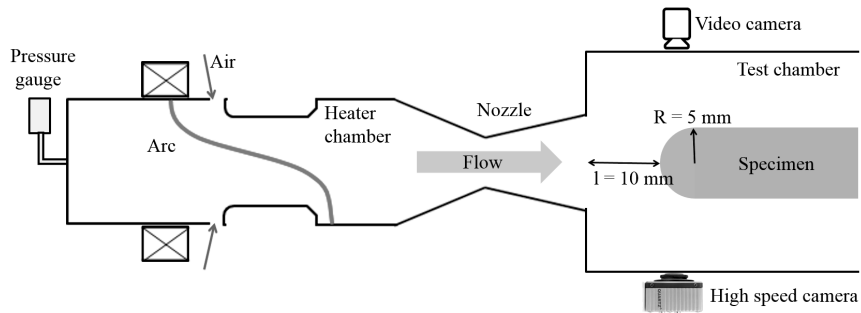


Fig. 4 Schematic of tungsten ablation test.

Ablation test was conducted with a 150-kW Huel's type arc heater [33]. Fig. 1 is a schematic flow chart of the entire facility, and Fig. 2 is a schematic diagram of the ablation test. The arc heater used in the experiments consists of two serial cylindrical electrodes made of copper, a gas inlet chamber between the electrodes, and a converging-diverging nozzle. As shown in the Fig. 1, electricity, air, and water for cooling are supplied to the arc heater by independent supply systems. Air used as working gas was injected from a constrictor located between an anode and a cathode. The electric potential difference of two electrodes generated an arc rotating via electromagnetic force. The injected air was heated to extremely high temperatures by the electric energy of the arc and changed into plasma state. The air was then flown into the test chamber through a converging-diverging (CD) nozzle. The pressure of heater chamber was measured by a pressure gauge mounted at the

upstream of the electrodes. The test chamber was connected to a diffuser and a vacuum pump, which kept the pressure of the test chamber low enough to create the operating conditions required for the test.

Table 1 Specification of 150 kW arc heater

Length of constrictor	42 mm
Diameter of constrictor	15 mm
Diameter of nozzle throat	6 mm / 7.5 mm
Nozzle area ratio	4 / 7.1
Nozzle expansion angle	24 °
Arc current	320–380 A
Air flow rate	6–12 g/s
Enthalpy range	5–12 MJ/kg

Some of the specifications of the 150-kW arc heater facility are listed in Table 1. In the facility, the flow conditions were controlled by varying the arc current and the mass flow rate of the injected air. According to the facility specifications, the arc current could vary from 320–380 A, and the air flow rate could vary from 6–12 g/s, resulting enthalpy range of 5–12 MJ/kg. According to the target flow conditions, two types of nozzle were used. They were simple converging-diverging nozzles whose expansion angle was 24°. The diameters of the nozzles were 6 mm and 7.5 mm, and the nozzle area ratios were 4 and 7.1 respectively.

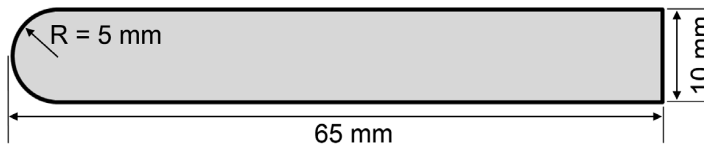


Fig. 5 Schematic of tungsten specimen.

Fig. 5 shows the schematic of a tungsten specimen used in the test. The specimen was a cylindrical rod of length 65 mm, diameter 10 mm, and weight 95.6 g. The nose end of the specimen was manufactured hemispherical. The specimen was mounted on the transportation system, which moves in the vertical direction. Since the flow quality was unstable shortly after arc ignition, the specimen was placed into the test

section a few seconds after ignition when the flow stabilized.

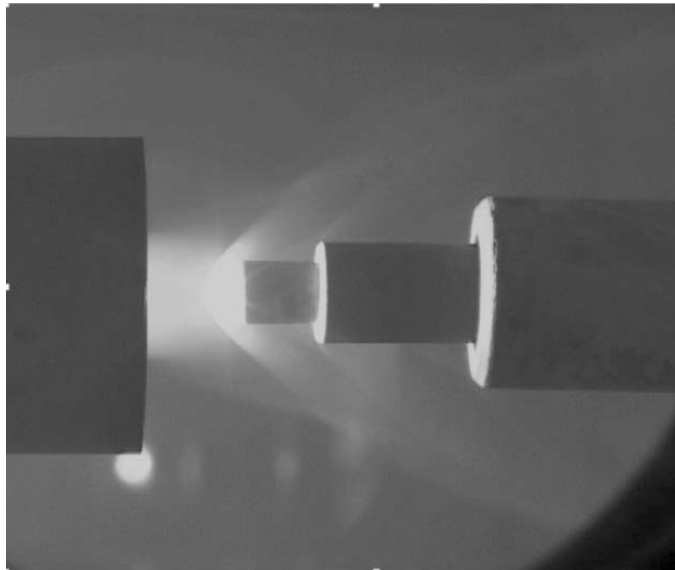


Fig. 6 Picture of tungsten ablation test captured by a video camera.

Fig. 6 is a picture captured by a video camera during the ablation test. The nozzle is located on the left side of the figure, and a tungsten specimen inserted in the graphite holder is mounted on the transportation system that is located on the right side of the figure. During the tests, the changes in shape of the specimen due to the ablation process was filmed through a window of the test chamber using a high-speed camera mounted outside the chamber. The changes in the length and mass of the specimen were measured to examine the total quantity of the ablated surface after the tests.

The nose end of the specimen was manufactured blunt because we confirmed in a previous ablation test the irregular progress of the ablation process and the undesired fluctuations in the stagnation points of flat-ended cylindrical specimens.

Fig. 7 shows the cross section of the flat-ended cylindrical specimen after the test. In the figure, it can be observed that the surface ablation starts from the top and its shape becomes irregular over different flow conditions. This irregular shape could

change the surface heat transfer rate considerably and increase the error in the test.

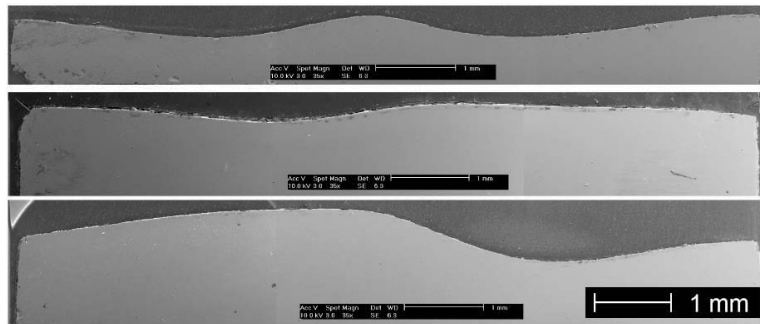


Fig. 7 Cross section of flat-ended specimens after ablation test.

By making the tip of the specimen to hemispherical shape, the stagnation point was more stabilized in contrast to the experiment with the flat-ended specimen. Moreover, unlike with the flat-ended specimen test, in which only the change in specimen length could be measured, the change in bluntness of the hemisphere-nosed specimen with time could be measured as well. Thus, in the test with hemispherical-ended specimen, it was possible to obtain more reliable data to develop an ablation model because the ablation data at several points along the surface could be measured simultaneously in one experiment. On the other hand, in the test with flat-ended specimen, only the change in length could be obtained. However, since the change in shape of the hemisphere-nosed specimen affects the heat transfer rate into the stagnation points, it should be considered carefully. These effects due to shape change during the ablation test were investigated via numerical simulation.

2.2 Ablation Test with Pure Tungsten Specimens

In order to obtain the ablation data needed to develop an ablation model, several ablation tests were conducted. To investigate the parameters which are related on ablation speed, different operational conditions were tested; Test time, arc current, air flow rate, and distance of the specimen from nozzle exit were changed in each ablation test. Detailed conditions of the experiment are as follows.

A. Base

At first, we conducted 9 runs of ablation tests at 3 different flow conditions and named the flow conditions Base1, Base2, and Base3. In each flow condition, 3 runs of the test were performed with different test times of 10, 30, and 60 seconds. Detailed test conditions are shown in table 2. In the facility, arc current and air flow rate are controllable independently, but arc voltage is automatically decided by the operation condition of the arc heater facility. The arc current was set to 360 A in Base1, and the arc current was set to 330 A in Base2 and Base3. While, the air flow rate was set to about 10 g/s in Base1 and Base2, and it was set to about 9 g/s in Base3. Test time, which the specimen is exposed to the flow, was controlled by the specimen transportation system. The distance from the nozzle exit to the specimen was 10 mm. Only in the Base cases, the nozzle area ratio was 4.

Table 2 Experimental condition of Base cases

Test number	Arc current (A)	Arc voltage (V)	Flow rate (g/s)	Test time (s)	
Base1	Run1	364.3	401.0	10.09	10
	Run2	364.4	398.6	10.12	30
	Run3	363.9	389.6	10.07	60
Base2	Run4	332.9	475.5	10.10	10
	Run5	332.9	475.5	10.10	30
	Run6	333.0	486.0	10.24	60
Base3	Run7	334.1	428.5	9.01	10
	Run8	333.7	424.0	9.03	30
	Run9	333.8	422.5	8.97	60

In the experiment, only the current and flow rate were independent variables that

could be adjusted to vary the flow conditions applied, while the voltage was automatically determined. The arc current values were 360 A and 330 A, and the mass flow rate was 10 g/s and 9 g/s. As shown in Table 2, Base1 has relatively high current values and high flow rates, while Base3 has relatively low current values and low flow rates. Base2 has low current values but high flow rates. The amount of ablation was confirmed to have changed significantly by varying the operational conditions slightly. Under each flow condition, three runs of tests were performed with different test times, 10, 30, and 60 seconds. The test time, which the specimen was subjected to the flow, can be controlled by the specimen transportation system. The distance from the nozzle exit to the specimen was kept at 10 mm initially.

In order to analyze ablation test results and develop an ablation model, the flow conditions generated from the arc heater need to be calculated first. As shown in Fig. 4, the air was heated by the arc in the heater chamber. Inside the heater chamber, since the temperature and pressure of the flow were high, whereas the velocity was almost zero, the flow could be assumed to be in thermochemical equilibrium state. The equilibrium flow can be characterized by two different thermodynamic properties—pressure and enthalpy. In the experiment, however, only the pressure of the heater chamber could be measured. The second thermodynamic property, enthalpy, was decided by Winovich’s empirical formula [34]. Winovich’s formula represents the enthalpy of flow generated by an arc heater as a function of the chamber pressure, the nozzle throat area and the mass flow rate. Winovich’s empirical formula can be written as follows:

$$h_t = 0.045337 \times \left[\frac{A^* P_t}{\dot{m}} \right]^{2.5189} \quad [J / kg] \quad (1)$$

Here, A^* is the nozzle throat area, P_t is the heater chamber pressure, and \dot{m} is the mass flow rate. From Eq. (1), the enthalpy of the heater chamber was calculated for all the test cases. Eq. (1) is known to be valid for the enthalpy range of 2.3–23 MJ/kg.



Fig. 8 Tungsten test specimens.

Fig. 8 is a picture of the specimens after and before the ablation tests. In the figure, the specimens are placed in order of the test run from the left to right. The specimen on the rightmost is the one before the test. It can be observed that the color of the surface exposed to the flow has turned dark blue from silver gray due to surface oxidation. It can also be observed that a few specimens have a yellow substance deposited on the sides after the tests. This yellow deposit was found to be WO_3 . The gaseous WO_3 generated by oxidation on the frontal surface condensed and reattached to the side surface whose temperature was lower than the frontal surface. This yellow substance was noticeable on a wider area of the specimens when the test time was shorter. In the cases with longer test time, the WO_3 seemed to have been partially condensed and reattached to the surface as the surface temperature increased over time. While, in the case of the specimen on the leftmost, it is thought that the surface temperature had not increased enough to produce the gaseous WO_3 due to the insufficient test time and weakest flow conditions. In this study, we aimed to develop a surface ablation model in the temperature range in which tungsten oxides are formed in their gaseous phase. Therefore, we focused on the cases with the test time of 60 seconds, in which the surface temperature could be increased to a sufficiently

high temperature region.

In order to observe shape changes due to ablation, a high-speed camera was mounted beside the test chamber. The images of the specimen were filmed by the camera at 60 frames per second (fps).

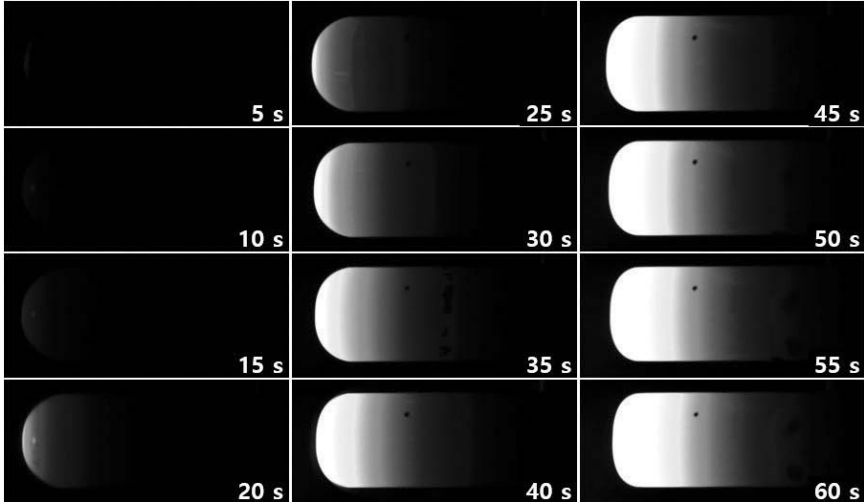


Fig. 9 High-speed camera images for 5 s intervals (Run3).

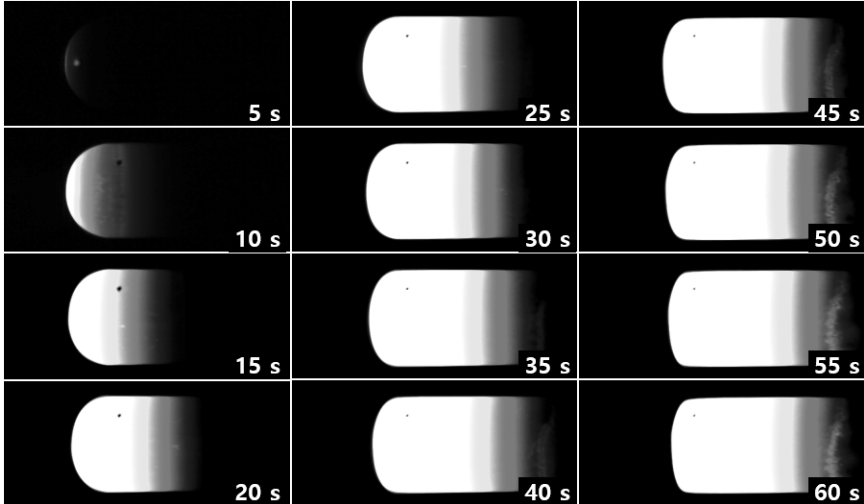


Fig. 10 High-speed camera images for 5 s intervals (Run6).

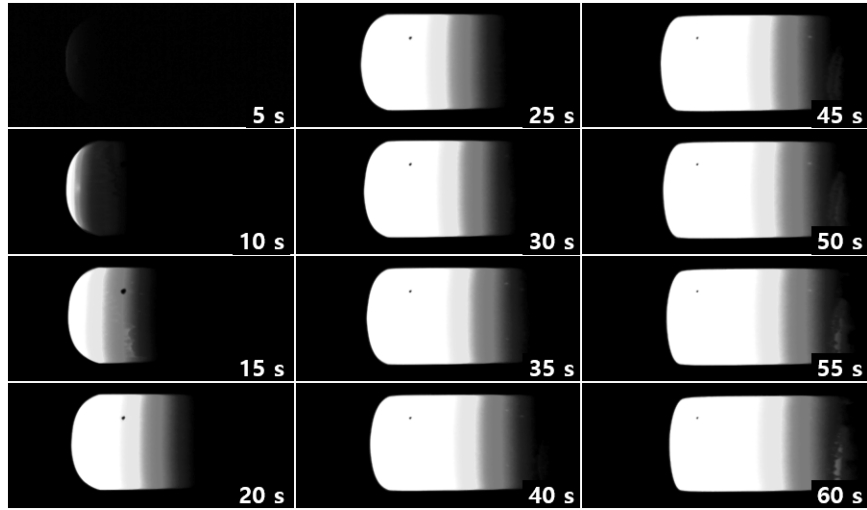


Fig. 11 High-speed camera images for 5 s intervals (Run9).

Fig. 9–Fig. 11 show the images taken by the high-speed camera within 5-second intervals. In the figures, the specimen exposed to the flow glows brighter as the exposure time is increased. The shape of the specimen changes from hemisphere to flat-nosed blunt shape due to the ablation over time. This indicates that ablation occurred most actively at the stagnation point.

Table 3 Ablation test results of Base cases

Test number	Test time (s)	Mass loss (g)	Recession (mm)	Mass ablation rate (g/s)	Recession rate (mm/s)
Base1	Run1	10	0.3	0.030	0.013
	Run2	30	0.6	0.020	0.021
	Run3	60	2.3	0.038	0.035
Base2	Run4	10	0.1	0.010	0.021
	Run5	30	1.8	0.060	0.056
	Run6	60	4.3	0.072	0.059
Base3	Run7	10	0.2	0.020	0.023
	Run8	30	1.6	0.053	0.046
	Run9	60	4.3	0.072	0.054

After the test, change of mass and length of test specimen were measured. Table 3 shows ablation test results of Base cases. Mass ablation rate and recession rate were calculated by dividing the total ablation amount by test time, and they are also listed in the table.

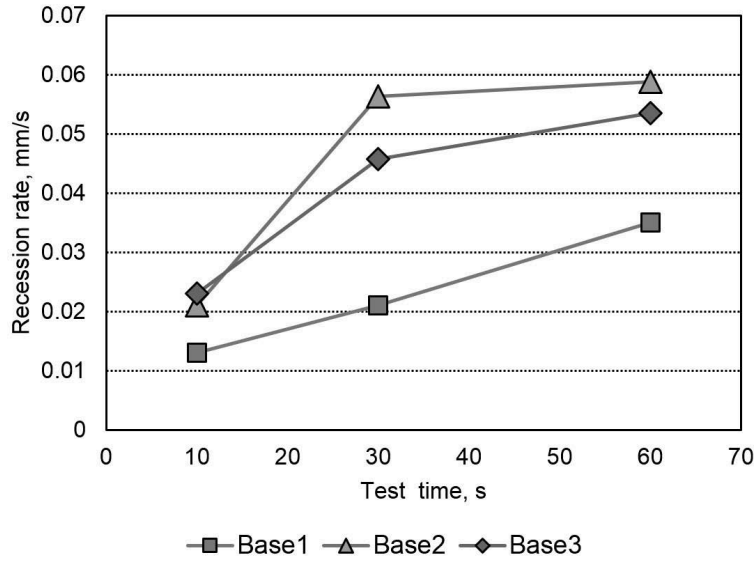


Fig. 12 Recession rate of Base cases.

Fig. 12 shows calculated recession rate of each run. The recession rate increased as the test time increased. It was the highest in Base2, since enthalpy and pressure of Base2 case were highest. While, the recession rate was lowest in Base1, of which flow condition was the weakest. When the flow condition was strong, the recession rate was almost saturated after 30 seconds as in Base2, since the surface temperature was saturated quickly. While in Base1, the recession rate increased as the test time increased, since the surface temperature needs more time to be saturated by the flow.

To develop an ablation model describing thermochemical ablation of tungsten surface, more detailed ablation data than just dividing total ablation amount to test time is needed. Actually, the ablation rate of the tungsten specimen changes during the test process continuously, since the surface temperature, the reaction coefficients, and the shape of specimen changes during the ablation test process. Thus, the data which can be used to extract the ablation rate at a certain moment was deduced from the high speed camera images.

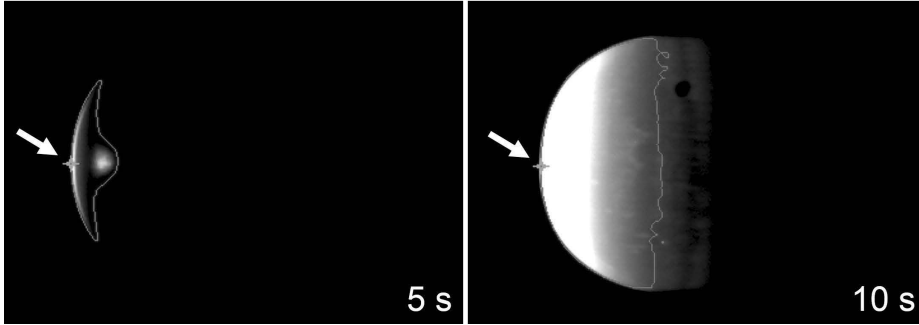


Fig. 13 Extraction of surface line and stagnation point (Run6).

From the high-speed camera images, stagnation point recession data on three test runs, Run3, Run6, and Run9 in Base case, were obtained. This data had been capture as time progressed. A simple MATLAB program was written to complete the image processing. After converting the high-speed camera images to grayscale, the surface lines were extracted from the gradient of brightness. Fig. 13 shows surface lines and stagnation points extracted by the program from the images captured at 5 second and 10 second in Run6 case. Since a total of 300 images were used for each test case, the time interval between any two stagnation point data was 0.2 seconds. The resolution of the image was 1024×512 pixels, and one pixel corresponded to about 0.05 mm of the specimen. After correcting the data of extracted stagnation points at successive points in time with the final recession data measured after the test, the graphs of stagnation point recession versus time and recession rate versus time were obtained. They are shown in Fig. 14 and Fig. 15 respectively.

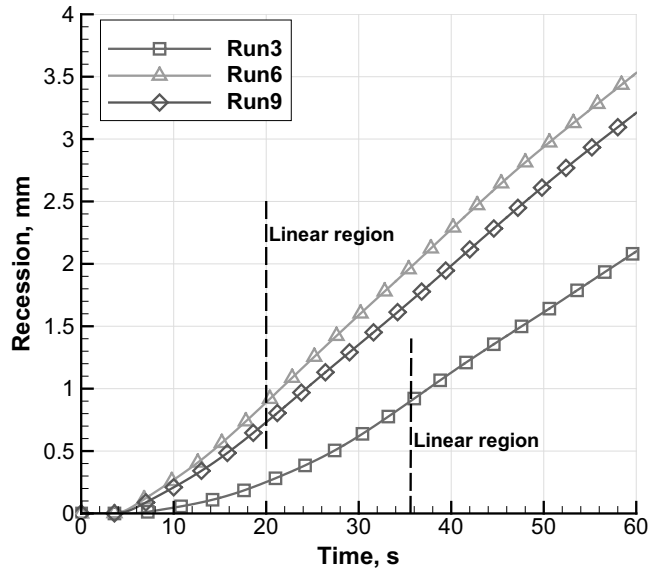


Fig. 14 Stagnation point recession versus time.

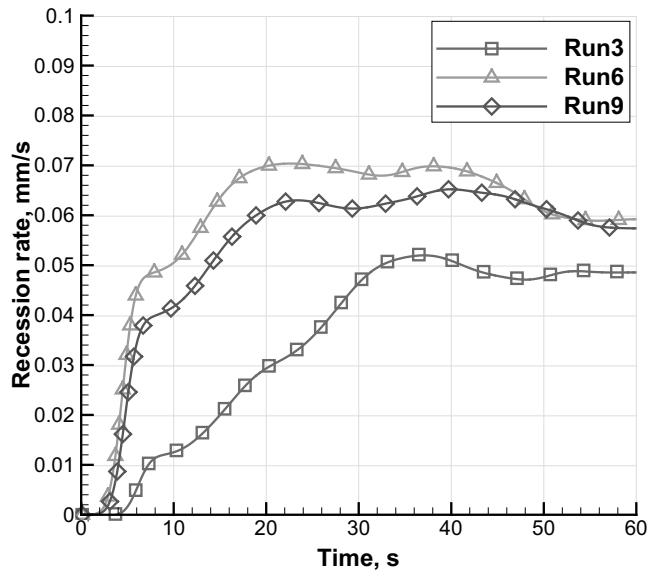


Fig. 15 Stagnation point recession rate versus time.

Fig. 14 shows recession versus time at the stagnation point in three different flow conditions. The test time window is 60 seconds. As shown in the figure, the stagnation point was recessed gradually from approximately 5 seconds as the surface temperature of the specimen increased with time, and after a certain point, it increased almost linearly. In the case of Run3, a linear region appears after

approximately 35 seconds, and in the case of Run6 and Run9, the region appears after 20 seconds. These results are clearer in the recession rate versus time plot shown in Fig. 15. The recession rate was the greatest in Run6 and marginally smaller in Run9. The recession and recession rate of Run3 were the smallest and were largely different from those in the other two cases. This observation may be due to the lower enthalpy condition of Run3. In Run6 and Run9, the recession rate rapidly increased at the beginning, only to saturate and become constant after 20 seconds. It decreased marginally towards the end. In the initial section, as the surface temperature increased with time, the ablation rate, too, increased due to the increase in surface reaction. After the completion of the middle stage, the chemical reaction rate no longer increased due to the diffusion limit, and the surface reached thermal equilibrium. Therefore, it seemed that the decrease in the recession rate in the latter section was due to a physical cause rather than chemical, as shown in the previous section: the retraction of position and the increase of nose radius of the specimen.

B. Varying Conditions over Time (VM, VC)

Additional ablation tests with the time-varying flow conditions were performed after the Base experiments. The mass flow rate and the arc current changed over time by 3 steps of 20 seconds in a single run. When the one variable changed, another variable was fixed. The mass flow rate changed from 8 g/s to 10 g/s to 12 g/s over time while the arc current were fixed to 340 A and 360 A in each of the flow conditions named VM1 and VM2 respectively.

Similarly, while the mass flow rate was fixed to 8 g/s and 12 g/s, arc current changed from 320 to 340 to 360 A over time. These flow conditions were labeled as VC1 and VC2 respectively. In each flow conditions, tests were repeated three times.

The distance between the nozzle exit and the specimen was 10 mm. Nozzle area ratio was 7.11. Detailed test conditions are shown in the following table.

Table 4 Experimental condition VM and VC cases

Test number		Arc current (A)	Arc voltage (V)	Air flow rate (g/s)	Test time (s)
VM1	Run1	343	357.2	7.38	0-20
			531.6	10.08	20-40
			589.8	11.79	40-60
	Run2	343	352.3	7.50	0-20
			538.9	10.29	20-40
			586.2	11.71	40-60
	Run3	343.1	372.9	7.84	0-20
			541.8	10.26	20-40
			585.0	11.72	40-60
VM2	Run4	363.6	361.9	7.96	0-20
			508.4	10.43	20-40
			570.8	11.88	40-60
	Run5	363.5	340.9	7.60	0-20
			510.5	10.29	20-40
			558.6	11.89	40-60
	Run6	363.3	351.3	7.84	0-20
			497.1	10.40	20-40
			566.1	11.98	40-60
VC1	Run1	323.1	419.6	8.30	0-20
			343.3	400.0	20-40
			363.5	388.8	40-60
	Run2	322.9	431.6	8.20	0-20
			342.8	411.1	20-40
			363.2	394.2	40-60
	Run3	322.9	435.4	8.30	0-20
			342.8	414.0	20-40
			363.6	400.3	40-60
VC2	Run4	323	606.5	12.08	0-20
			343.6	590.5	20-40
			363.7	573.9	40-60
	Run5	322.5	611.3	12.17	0-20
			343.2	591.7	20-40
			363.5	573.2	40-60
	Run6	323	609.0	12.18	0-20
			342.8	594.1	20-40
			363.2	577.4	40-60

After the tests, similar to Base case, change of mass and length of the specimens were measured, then the rates of changes to time were calculated. They are listed in Table 5.

Additionally, in these VM and VC cases, the tests were repeated three times. From this results, the repeatability and reproducibility of the ablation test in 150-kW arc heater was checked. From the results of repetitive tests, it was confirmed that the

shapes of ablated specimens were almost identical to one another. The maximum standard deviations of the changes in length and mass by ablation were 0.08 mm and 0.08 g, which were equivalent to 1.3% and 2.0% of the total recession and mass reduction respectively.

Table 5 Ablation test results of VM and VC cases

Test number		Test time (s)	Mass loss (g)	Recession (mm)	Mass ablation rate (g/s)	Recession rate (mm/s)
VM1	Run1	60	6.2	4.04	0.1033	0.0673
	Run2		6.3	4.08	0.1050	0.0680
	Run3		6.2	4.23	0.1033	0.0705
VM2	Run4	60	6.5	4.2	0.1083	0.0700
	Run5		6.3	4.21	0.1050	0.0702
	Run6		6.4	4.27	0.1067	0.0712
VC1	Run1	60	5.7	3.67	0.0950	0.0612
	Run2		5.8	3.68	0.0967	0.0613
	Run3		5.7	3.72	0.0950	0.0620
VC2	Run4	60	6.9	4.65	0.1150	0.0775
	Run5		6.8	4.55	0.1133	0.0758
	Run6		6.9	4.53	0.1150	0.0755

Mass reduction rate and recession rate of VM1, VM2, VC1, and VC2 are shown in Fig. 16. These four cases are initially designed to figure out the effect of time-varying variables on the ablation. However, as we stated in Base experiment, since the ablation rate was affected by the surface temperature, finding a correlation between the time-varying variables and the ablation rate of each step was not simple. Instead, we figured out effects of fixed variables, the arc current and the mass flow rate, by comparing VM1 to VM2 and VC1 to VC2 respectively. Comparing the results of VM1 to those of VM2, as the arc current increases, the mass reduction rate and the recession rate increases very slightly. However, by comparing the VC1 to VC2, as the mass flow rate increases, both the mass reduction rate and the recession rate increases clearly. In other words, the increment of the mass flow rates increased the ablation rates clearly while the change of the arc current affects little the ablation rate. This result was thought as the characteristics of the facility rather than general.

This is because the range of current change was not sufficiently wide to increase flow enthalpy due to the operational limit of the facility.

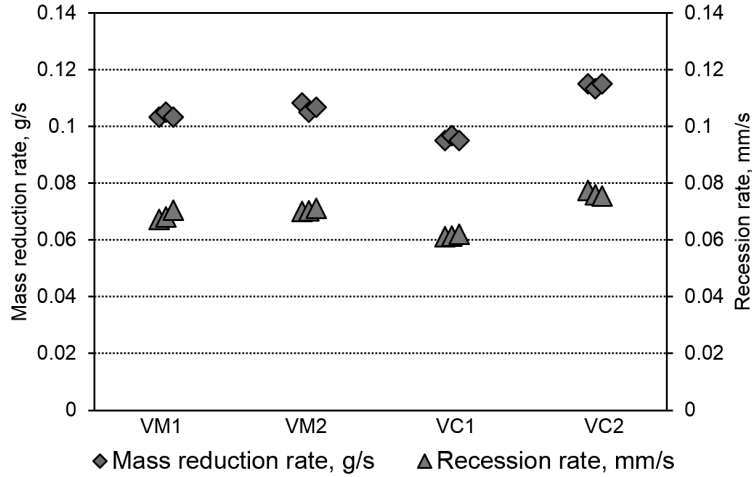


Fig. 16 Mass reduction rate and recession rate (VM and VC cases).

C. Distance (Dist)

The ablation tests were conducted with three different specimen positions. In each test case, the distance from the nozzle exit to the specimen was 10, 20, and 30 mm and we named them Dist1, Dist2, and Dist3 respectively. The air flow rate and the arc current were fixed at about 340 A and 11.5 g/s. At the same distance, the tests were repeated twice. The test time was 30 seconds in all the cases. Detailed test conditions and the ablation results are shown in Table 6.

Table 6 Experimental conditions of Dist cases

Test number	Arc current (A)	Arc voltage (V)	Air flow rate (g/s)	Distance (mm)	Stag. Pressure (kPa)	Mass ablation (g)	
Dist1	Run1	343.6	575.0	11.22	10	83.33	3.2
	Run2	343.1	595.7	11.84			3.3
Dist2	Run3	342.8	586.0	11.69	20	56.60	2.4
	Run4	342.8	586.0	11.69			2.5
Dist3	Run5	343.0	581.6	11.65	30	40.46	1.6
	Run6	343.1	583.1	11.65			1.5

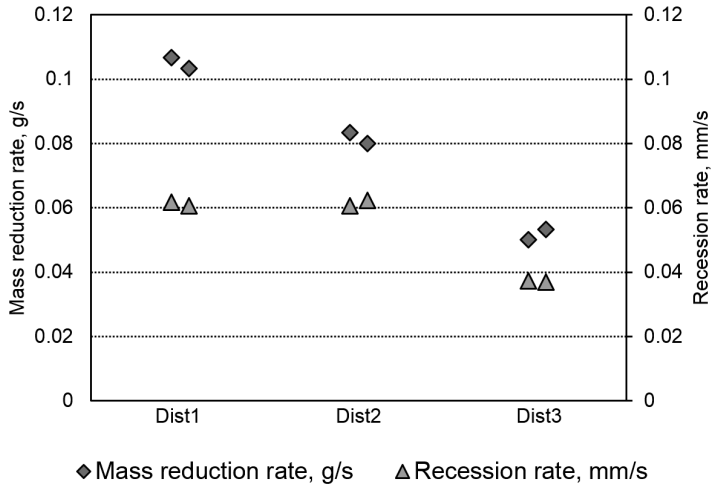


Fig. 17. Mass reduction rate and recession rate by distance (Dist cases).

Fig. 17 shows results of Dist experiments. The mass reduction rates and the recession rates versus the distance from the nozzle exit to the specimen are plotted. As shown in fig. 8, the mass reduction rate increased as the distance decreased. The recession rate showed a similar tendency, but the recession rate when the distance was 10 mm was almost same as the recession rate when the distance was 20 mm. The difference in ablation shape may have contributed to this discordance between the recession rate and the mass reduction rate. The ablation shape of Dist2 case was more flat than that of Dist3 case. That is, since the ablation occurred more actively at the stagnation point than at the shoulder, stagnation point recession in Dist2 was almost the same as that of Dist3 even the mass reduction was smaller.

2.3 Ablation Test with W-HfC Specimens

After the ablation tests on pure tungsten specimens, additional ablation tests on tungsten composites were performed with the 150-kW arc heater facility. First, tungsten composites reinforced with various contents of hafnium carbide were tested. Four kinds of specimens with different compositions were prepared by ADD, and those are listed in the following table.

Table 7 Contents of W-HfC composites

No.	W volume contents (%)	HfC volume contents (%)
1	97	3
2	90	10
3	80	20
4	70	30

The specimen was a cylindrical rod of length 40 mm, diameter 10 mm. Operating conditions of the arc heater was set to arc current of 360 A and mass flow rate of 10 g/s. Test time were 5, 10, and 15 seconds respectively.

Fig. 18 shows the specimens after the test. After the ablation test, discoloration by the fine particles supposed to be the oxides of hafnium was clearly observed over the surface of the specimens. Similar to that of the pure tungsten specimens, degradation of the surface was measured, and it became greater as the exposure time increased.

Fig. 19 is a graph of ablation depth versus time against different HfC contents. As shown in the figure, maximum 0.88mm of ablation in depth occurred, and as the test time increased, ablation depth increased as well. Meanwhile, as HfC contents increased, ablation in depth decreased due to the effect of HfC.

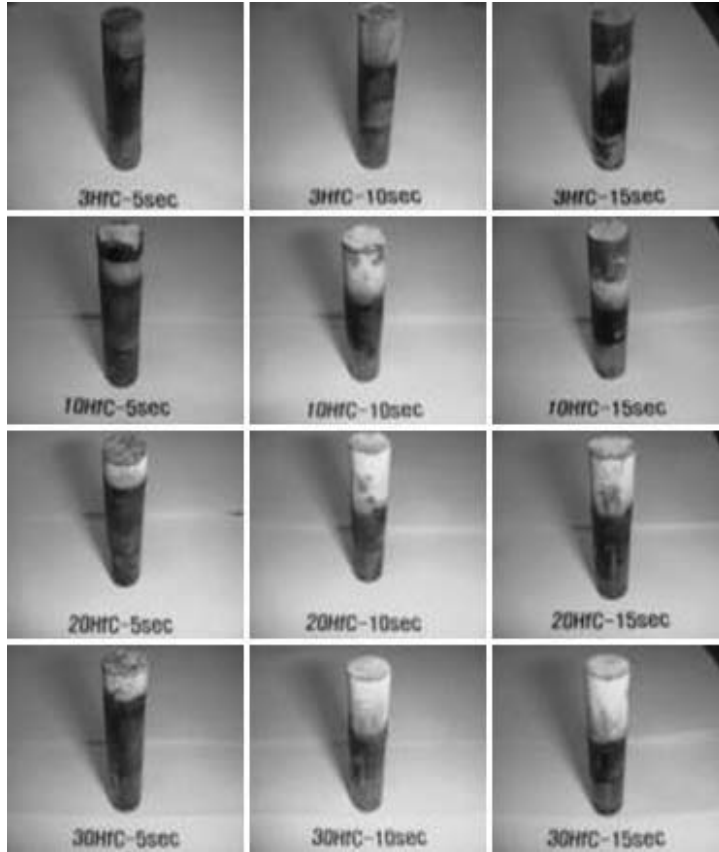


Fig. 18 W-HfC specimens after ablation tests.

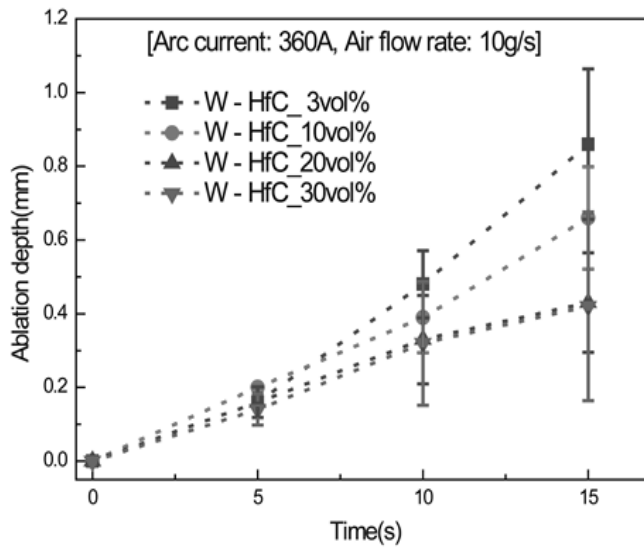


Fig. 19 Ablation depth versus time against different HfC contents.

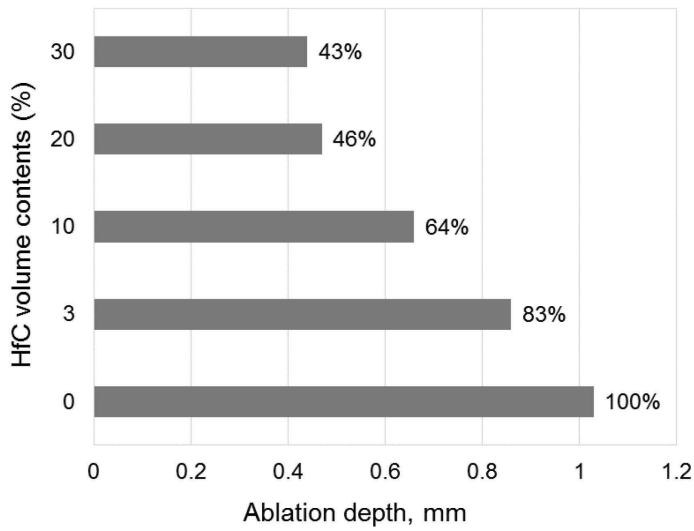


Fig. 20 Increment of ablation resistance by increasing HfC vol%.

In order to figure out the effect of HfC contents on ablation resistance, the results were compared to that of the pure tungsten specimen. Fig. 20 shows the ratio of the decreased ablation depth of W-HfC composite specimens to the total ablation depth of pure tungsten specimen under the same test condition. In the figure, the ablation resistance increases to about 60% by increasing HfC contents until it reaches 20%. It means that in the same condition, the ablation depth of the W(80vol%)-HfC(20vol%) specimen is correspond to the 40% of pure tungsten. When the contents of HfC increased over 20%, ablation resistance didn't increased anymore. From the above results, we confirmed that the addition of the hafnium carbide raises ablation resistance of tungsten almost linearly until the volume contents of HfC reaches about 20%.

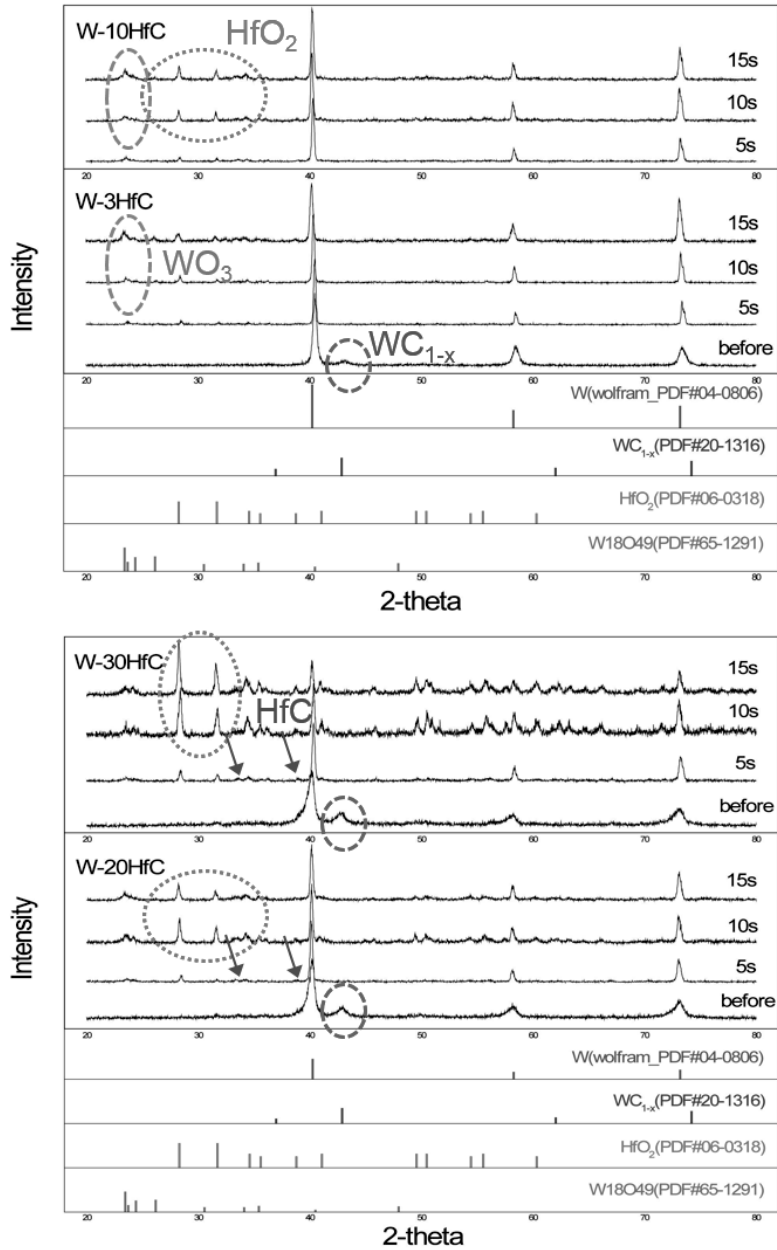


Fig. 21 X-ray diffraction after ablation test of W-HfC specimens.

Phase analysis through X-ray diffraction were performed before and after the ablation test. Fig. 21 represents X-ray diffraction patterns of the specimens with different compositions. Before the specimens were tested, only tungsten phase pattern, HfC phase pattern, and small amount of tungsten carbide phase pattern were

observed. While, as the test time increased, oxidation occurred actively at the surface, resulting in increment of the peaks of $W_{18}O_{49}$ and HfO_2 . In the high temperature environment, HfO_2 was the most stable oxide phase generated during ablation.

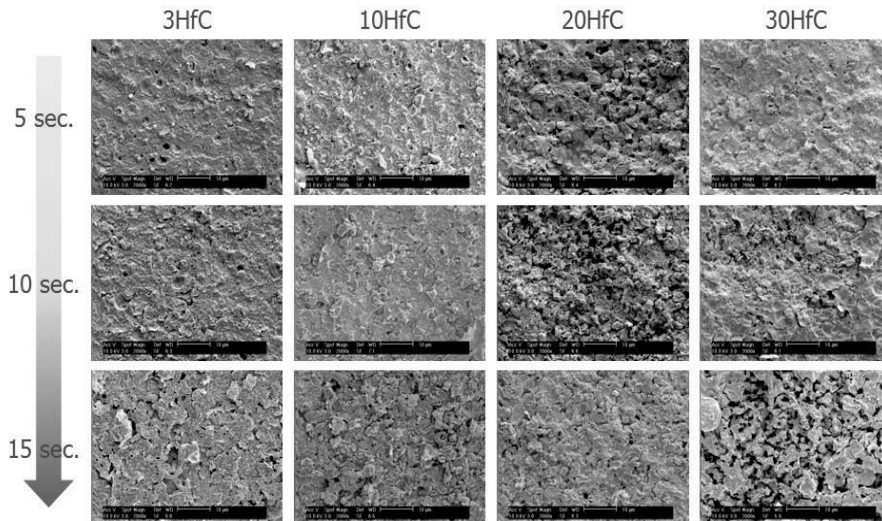


Fig. 22 Surface microstructure of W-HfC specimens after the ablation test.

Fig. 22 is a picture showing microstructure of the W-HfC specimens after the test. As the HfC contents increased, porosity of the surface increased. When the contents of HfC is small, mostly tungsten oxides are generated on the surface, then they melt and blown away due to relatively low melting points (WO_2 :1973 K, WO_3 :1746 K), resulting in smooth surface. When the HfC contents increases, more HfO_2 produced, then suppress the ablation by the melting and evaporation of tungsten oxides because the melting point of HfO_2 is much higher (3031 K). As the tungsten oxides are melted away between the HfO_2 in solid phase, pores are generated as shown in the figure.

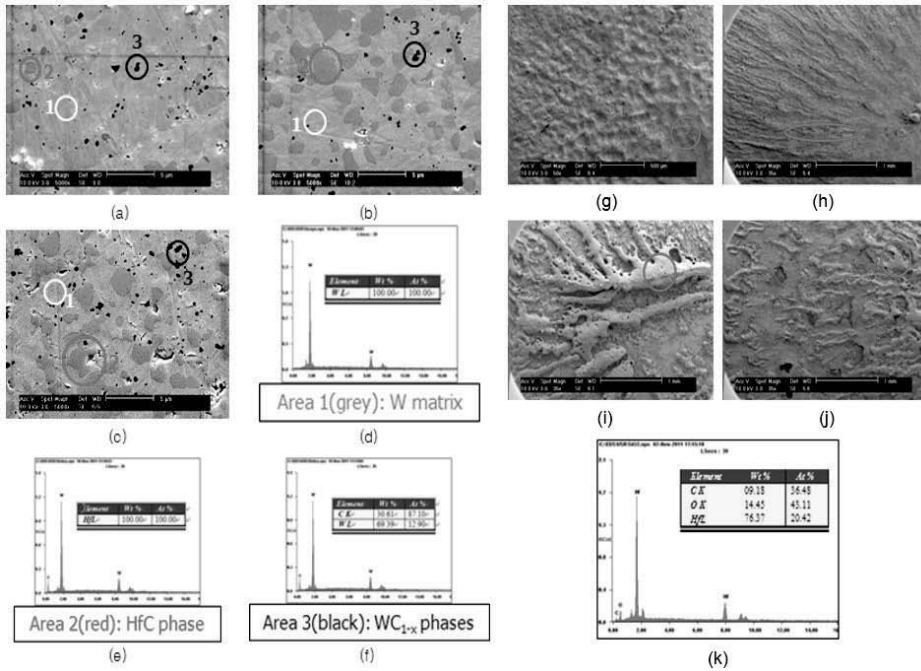


Fig. 23 EDS analysis result of the surface microstructure of W-HfC specimens.

For more detailed analysis, EDS (Energy Dispersive X-ray Spectroscopy) analysis was performed. Fig. 23 shows the EDS results on the specimens before and after the tests. In the figure, (a)-(f) are the results before the test. In all the compositions, three types of grains with different shades were observed. From the EDS results, it was confirmed that 1st (gray) grain was tungsten matrix phase, 2nd (red) grain was HfC phase, and 3rd (black) grain was WC_{1-x} phase.

In the figure, (g)-(k) show the EDS results on the points where the traces of liquid phase were observed. In the specimens with high contents of HfC, wave-shaped traces were found which seems to be generated by the flow of melt layer, and from the EDS, they are turned out to be HfO₂.

2.4 Ablation Test with W-ZrC Specimens

Tungsten composites reinforced with zirconium carbide (ZrC) of various contents were tested. The effect of manufacturing methods, also, were tested. Total eight different samples were tested, and they are listed in Table 8.

Table 8 Samples for tungsten composite ablation test

No.	Samples
1	W
2	W-10vol%ZrC (I)
3	W-20vol%ZrC (I)
4	W-30vol%ZrC (I)
5	W-10vol%HfC (I)
6	W-30vol%(Zr,W0.12)C (H)
7	W-30vol%(Zr,W0.3)C (H)

No. 1 is a pure tungsten samples. Samples 1–7 were sintered for two hours by hot press method under the conditions of 1,900 °C, 30–50 Mpa. Those samples can be divided into three types. Sample No.1 was sintered with the tungsten powder purchased at TaeguTec. Samples No. 2–4 were manufacture by the in-situ process: The samples were sintered from the tungsten composite powder made by high energy milling and carbonization-reduction of tungsten oxide powder and graphite powder in a vacuum furnace (W-ZrC: 1500 °C, 2 hours, W-HfC: 1600 °C, 1 hour). No.5 sample was made to be compared with the W-ZrC composite made by the same process. Samples 6–7 are made by the hybrid process: The samples were sintered from the tungsten composite powder made by simply mixing the commercial tungsten powder and solid-solution phase (Zr,W)C made by high energy milling and carbonization-reduction. These samples showed great characteristics in terms of strength.

After the ablation test in the same conditions, change in length were compared. Fig. 24 shows the recession of each specimen based on the recession of sample No.1 (pure tungsten, 100%).

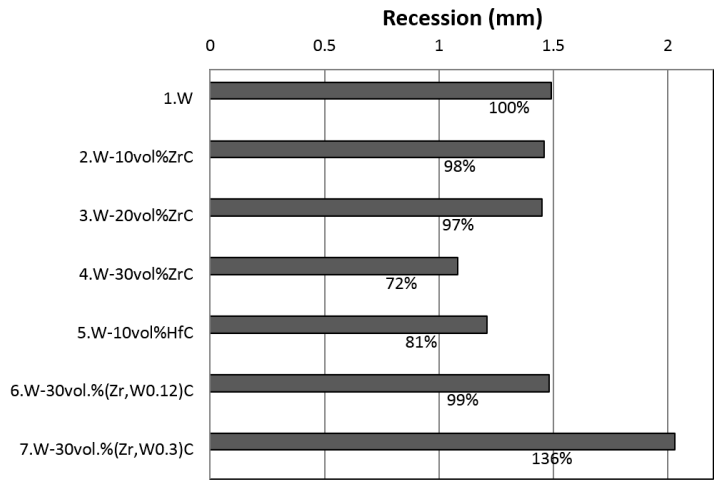


Fig. 24 Recession of various W-ZrC/HfC samples after ablation test.

As a result, sample No.4 (W-30vol%ZrC(I)) showed the least recession among the samples. Compared with other samples made by the in-situ process, it was confirmed that as the ZrC volume contents increased, ablation resistance increased. This results was also observed in the previous section, when the HfC was used as a reinforcement. When we compared the recession of the samples with the same contents but different reinforcement materials, No.2 and No.5, sample No.5 (W-10vol%HfC) showed superior ablation resistance. In addition, samples which were made by the hybrid process showed rather worse ablation resistance than the pure tungsten samples. This reveals that the higher mechanical strength does not imply the higher thermal resistance.

To investigate the physics occurring during the ablation process, various post analysis were performed to the specimens after the test. First, to figure out which species are formed and vanished during the ablation, phase analysis using XRD patterns was performed.

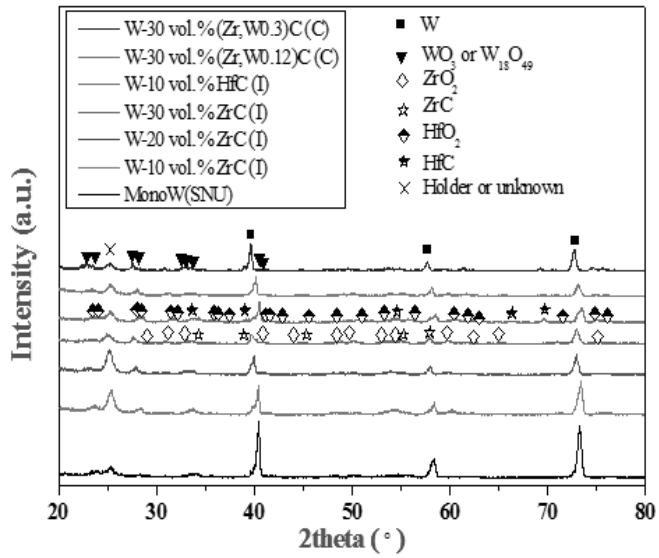


Fig. 25 XRD patterns after the ablation test on various composites.

As shown in Fig. 25, since the surface react with the oxygen actively at high temperature, carbide phases (ZrC, HfC) which existed before the test vanishes and oxide phases (ZrO₂, HfO₂) are newly formed. It is noticeable that tungsten oxides such as WO₃ are also formed from the XRD patterns. In addition, it can be deduced that the crystallinity of tungsten decreased from the reduction of peak of W.

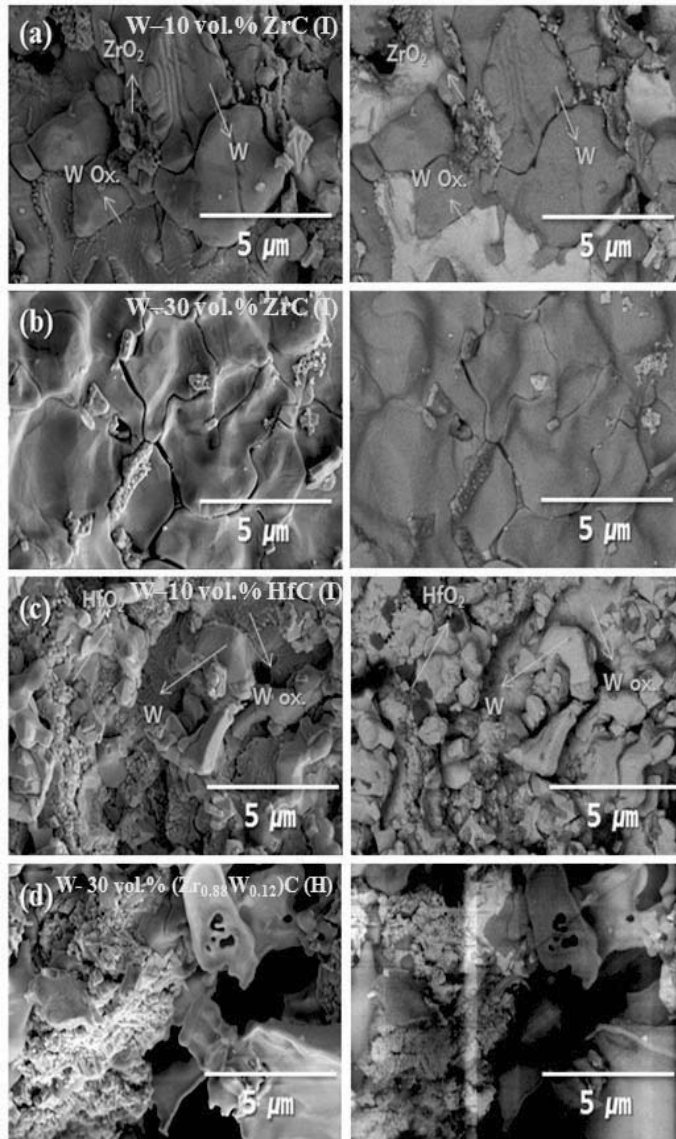


Fig. 26 FE-SEM images of ablated surface (left : SE / right : BSE mode).

Microstructure of the ablated surface of the specimens was investigated through the Field Emission Scanning Electron Microscopy (FESEM). In the W-ZrC system samples, tungsten re-crystallized after melt during the ablation process. During the tungsten recrystallizes, all the carbides in the grain boundary oxidize and flow out and form oxides. These oxides agglomerate each other then cover the surface of the tungsten, and protect it from the high enthalpy flows. This suppress the oxidation of

the tungsten and consequently prevent ablation.

When we compared the sample with the same volume contents but different materials, in situ W-HfC and W-ZrC ((a) and(c) in the figure), the amount of oxides formed at the surface were large and the grain size was small in W-HfC specimen than those in W-ZrC specimen. The grain size of re-crystallized tungsten was also small in W-HfC specimen. From these, HfC forms more superior oxides shields on the tungsten composite surface. This is because W and Hf can form metal phase (W,Hf) through mutual diffusion, while W and Zr cannot because the mutual diffusion doesn't occur between W and Zr. It is possible to understand that since the interfacial reactivity between W and Hf is better than that between W and Zr, W-HfC composites has better ablation resistance.

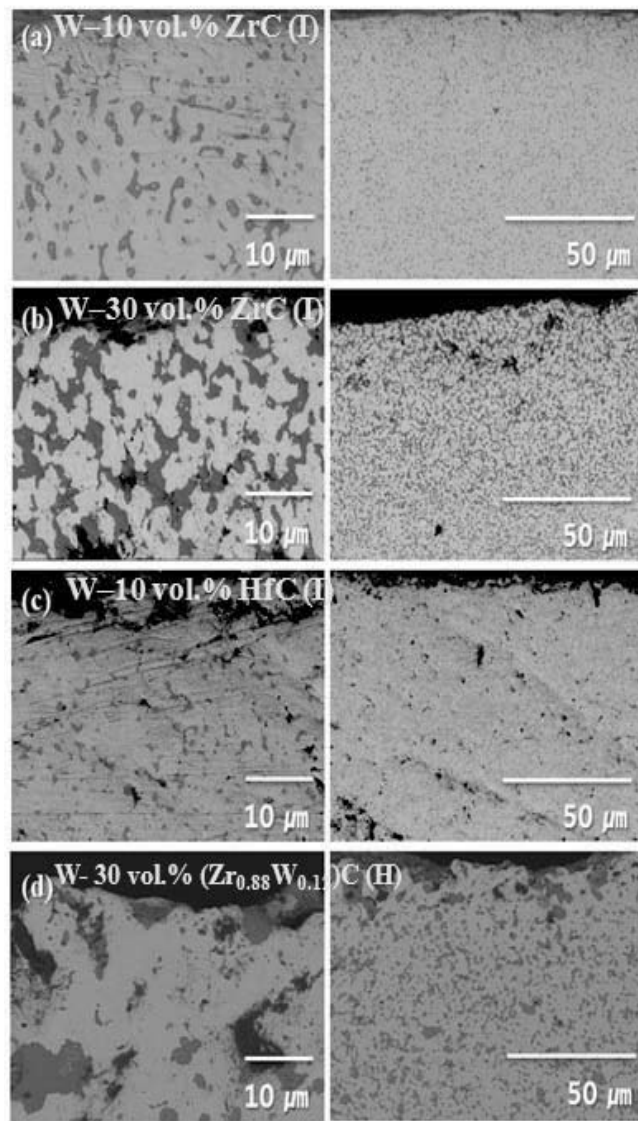


Fig. 27 FE-SEM images of cross-sections of the specimens.

Fig. 27 shows FE-SEM images of cross-sections of the specimens after the test. In the figure, coalescence of ZrC is observed noticeably in W-10vol%ZrC(I) and W-30vol%ZrC(I) samples. Particularly, as the diffusion of grain boundary processed actively, a number of ZrC deformed in a long shape were found. Inside the ZrC, tungsten seemed as gray dots precipitated. These are thought to be formed from the solid-solution phased $(Zr_{1-x}W_x)C$ closed by the ZrC while the specimen cooled down

fast after the test.

In the figure, the grain size of HfC in W-10vol%HfC(I) specimen was much smaller than that of ZrC in W-10vol%ZrC(I) specimen. This is because the grain growth of HfC by coalescence or diffusion was little since thermal stability of HfC is higher than ZrC.

In the W-30vol%(Zr,W_{0.12})C(H) specimen, pores (black) and carbides (dark gray) are clustered, and the size of them are much bigger than other samples. These are thought to be generated by the drastic oxidation during the ablation.

Chapter 3. Numerical Approach

3.1 Flow Governing Equation

Dimensionless 2-dimensional/axi-symmetric non-equilibrium Navier-Stokes equations are as follows.

$$\frac{\partial Q}{\partial t} + \frac{\partial E}{\partial x} + \frac{\partial F}{\partial y} = \frac{\partial E_v}{\partial x} + \frac{\partial F_v}{\partial y} + S + \alpha(H_v - H) \quad (2)$$

$$Q = \begin{pmatrix} \rho \\ \rho u \\ \rho v \\ \rho e_t \\ \rho_i \\ \vdots \\ \sum_s \rho e_{v,s} \end{pmatrix}, E = \begin{pmatrix} \rho u \\ \rho u^2 + p \\ \rho uv \\ (\rho e_t + p)u \\ \rho_i u \\ \vdots \\ \sum_s \rho e_{v,s} u \end{pmatrix}, F = \begin{pmatrix} \rho v \\ \rho uv \\ \rho v^2 + p \\ (\rho e_t + p)v \\ \rho_i v \\ \vdots \\ \sum_s \rho e_{v,s} v \end{pmatrix},$$

$$S = \begin{pmatrix} 0 \\ 0 \\ 0 \\ 0 \\ W_i \\ \vdots \\ \sum_s W_s e_{v,s} + \sum_s W_{v,s} \end{pmatrix}, H = \frac{1}{y} \begin{pmatrix} \rho v \\ \rho uv \\ \rho v^2 \\ (\rho e_t + p)v \\ \rho_i v \\ \vdots \\ \sum_s \rho e_{v,s} v \end{pmatrix},$$

$$E_v = \frac{Ma_\infty}{Re_\infty} \begin{pmatrix} 0 \\ \tau_{xx} \\ \tau_{xy} \\ \tau_{xx}u + \tau_{xy}v - \frac{1}{Pr_\infty(\gamma_\infty - 1)}(q_x + q_{vx}) - \sum_{s=1}^{nsp} h_s J_{Dx,s} \\ -J_{Dx,i} \\ \vdots \\ -\frac{1}{Pr_\infty(\gamma_\infty - 1)}q_{vx} - \sum_{s=1}^{nsp} e_{v,s} J_{Dx,s} \end{pmatrix},$$

$$F_v = \frac{Ma_\infty}{Re_\infty} \begin{pmatrix} 0 \\ \tau_{xy} \\ \tau_{yy} \\ \tau_{xy}u + \tau_{yy}v - \frac{1}{Pr_\infty(\gamma_\infty - 1)}(q_y + q_{vy}) - \sum_{s=1}^{nsp} h_s J_{Dy,s} \\ -J_{Dy,i} \\ \vdots \\ -\frac{1}{Pr_\infty(\gamma_\infty - 1)}q_{vy} - \sum_{s=1}^{nsp} e_{v,s} J_{Dy,s} \end{pmatrix},$$

$$H_v = \frac{1}{y} \frac{Ma_\infty}{Re_\infty} \begin{pmatrix} 0 \\ \tau_{xy} - \frac{2}{3}y \frac{\partial}{\partial x} \left(\mu \frac{v}{y} \right) \\ \tau_{yy} - \tau_{\theta\theta} - \frac{2}{3} \left(\mu \frac{v}{y} \right) - \frac{2}{3}y \frac{\partial}{\partial y} \left(\mu \frac{v}{y} \right) \\ u\tau_{xy} + v\tau_{yy} - \frac{1}{Pr_\infty(\gamma_\infty - 1)}(q_y + q_{vy}) - \sum_{s=1}^{nsp} h_s J_{Dy,s} + \Omega \\ -J_{Dy,i} \\ \vdots \\ -\frac{1}{Pr_\infty(\gamma_\infty - 1)}q_{vy} - \sum_{s=1}^{nsp} (e_{v,s} J_{Dy,s}) \end{pmatrix} \quad (3)$$

Here, α is the coefficients for axi-symmetric calculation. If α equals zero, Eq. (2) becomes the governing equations for 2-D plain flow, and if α equals unity, it becomes axi-symmetric flow. Ω in vector H_v in Eq. (3) is as follows:

$$\Omega = -\frac{2}{3} \left[\mu \frac{v^2}{y} + y \frac{\partial}{\partial y} \left(\mu \frac{v^2}{y} \right) + y \frac{\partial}{\partial x} \left(\mu \frac{uv}{y} \right) \right] \quad (4)$$

The relation between the non-dimensionalized value (without subscript) and the real value (subscript R) is as follows.

$$\begin{aligned}
t_R &= t \times (L_\infty / c_\infty), & x_R &= x \times L_\infty, & y_R &= y \times L_\infty, & \rho_R &= \rho \times \rho_\infty, \\
u_R &= u \times c_\infty, & v_R &= v \times c_\infty, & p_R &= p \times (\rho_\infty c_\infty^2), & T_R &= T \times T_\infty, \\
e_R &= e \times c_\infty^2, & h_R &= h \times c_\infty^2, & \mu_R &= \mu \times \mu_\infty, & k_R &= k \times k_\infty, \\
k_{vR} &= k_v \times k_\infty, & D_R &= D \times (\rho_\infty / \mu_\infty)
\end{aligned} \quad (5)$$

A. Energy for non-equilibrium flow

e_t represents the total energy of flow per unit mass and it can be expressed as follows:

$$e_t = e_{trans} + e_{rot} + e_{hof} + e_{vib} + e_{kin} \quad (6)$$

$$e_{trans} = \frac{3}{2} \sum_i \frac{\bar{R}}{M_i} \alpha_i T \quad (7)$$

$$e_{rot} = \sum_j \frac{\bar{R}}{M_j} \alpha_j T \quad (8)$$

$$e_{hof} = \sum_i A_f H_i^0 \alpha_i \quad (9)$$

$$e_{vib} = \sum_j e_{v,j} \alpha_j \quad (10)$$

$$e_{v,j} = \frac{\bar{R}}{M_j} \left(\frac{\theta_j}{\exp(\theta_j / T_v) - 1} \right) \quad (11)$$

$$e_{kin} = \frac{1}{2} (u^2 + v^2) \quad (12)$$

$$\bar{R} = 8314.4598 \quad [J / kmol \cdot K] \quad (13)$$

B. Viscous term

In viscous flow, the array E_v and F_v in Eq. (2) should be considered. Heat transfer rates by translational-rotational conduction and vibrational conduction are given as follows:

$$q_x = -k \frac{\partial T}{\partial x}, \quad q_y = -k \frac{\partial T}{\partial y} \quad (14)$$

$$q_{vx} = -k_v \frac{\partial T_v}{\partial x}, \quad q_{vy} = -k_v \frac{\partial T_v}{\partial y} \quad (15)$$

In certain references, heat transfer by vibrational energy is expressed as follows:

$$q_{vx} = -\mu \frac{\partial e_v}{\partial x}, \quad q_{vy} = -\mu_v \frac{\partial e_v}{\partial y} \quad (16)$$

Viscous stress tensors are calculated as follows:

$$\tau_{xx} = \frac{4}{3}\mu \frac{\partial u}{\partial x} - \frac{2}{3}\mu \frac{\partial v}{\partial y} \quad (17)$$

$$\tau_{yy} = \frac{4}{3}\mu \frac{\partial v}{\partial y} - \frac{2}{3}\mu \frac{\partial u}{\partial x} \quad (18)$$

$$\tau_{xy} = \tau_{yx} = \mu \left(\frac{\partial u}{\partial x} + \frac{\partial v}{\partial y} \right) \quad (19)$$

Mass fluxes by molecular diffusion of each species except electron are calculated by modified Fick's law as follows:

$$J_{Dx,i \neq e} = -\rho D_i \frac{\partial \alpha_i}{\partial x} - \alpha_i \sum_{s \neq e} \left(-\rho D_s \frac{\partial \alpha_s}{\partial x} \right) \quad (20)$$

$$J_{Dy,i \neq e} = -\rho D_i \frac{\partial \alpha_i}{\partial y} - \alpha_i \sum_{s \neq e} \left(-\rho D_s \frac{\partial \alpha_s}{\partial y} \right) \quad (21)$$

The mass flux of electron is calculated assuming ambipolar diffusion to satisfy charge neutrality of the flow as follows[35, 36]:

$$J_{D,e} = \frac{1}{q_e} \sum_{s \neq e} J_{D,s} q_s \quad (22)$$

Here, q_i represents electric charge of species i per unit mass.

C. Source term

W_i is a source term for the mass generation of species i by chemical reactions.



When the above reaction equation was considered, the change in time of the concentration of a species can be expressed as follows:

$$\frac{d[X_i]}{dt} = (v_i'' - v_i') \left\{ k_f \prod_i [X_i]^{v_i'} - k_b \prod_i [X_i]^{v_i''} \right\} \quad (24)$$

Here, k_f and k_b represent forward and backward reaction rate coefficients respectively. Several models exist for the values of them, and Park's model [37-42] and Gupta's model [43] were considered in this study. Detailed values are described in the appendix.

Finally, W_i in Eq. (3) is calculated as follows:

$$W_i = M_i \frac{d[X_i]}{dt} \quad (25)$$

$W_{v,i}$ represents energy relaxation from translational-rotational energy to vibrational energy, and it can be written by the Landau-Teller equation as follows:

$$W_{v,i} = \rho_i \frac{e_{v,i}(T) - e_{v,i}(T_v)}{\tau_i} \quad (26)$$

Here, $e_{v,i}$ is a vibrational energy of species i and can be calculated with vibrational characteristic temperature θ_i as follows:

$$e_{v,i}(T) = \frac{\bar{R}}{M_i} \frac{\theta_i}{\exp(\theta_i / T) - 1} \quad (27)$$

τ_i , vibrational relaxation time is calculated as the sum of Landau-Teller vibrational relaxation time, $\tau_{LT,i}$ and a correction term, $\tau_{c,i}$, considering limited value of collision cross section at high temperature environment.

$$\tau_i = \tau_{LT,i} + \tau_{c,i} \quad (28)$$

$$\tau_{LT,i} = \frac{\sum_s X_s}{\sum_s X_s / \tau_{is}} \quad (29)$$

Here, τ_{is} is the relaxation time when species i and s collide with each other and it is calculated with the model of Milikan and White [44].

$$\tau_{is} = \frac{101325}{p_i} \exp \left[A_{is} \left(T^{-1/3} - B_{is} \right) - 18.42 \right] \quad (30)$$

Here, p_i is the pressure of species i in Pa . The values for A_{is} and B_{is} can be found from tabulated data in Appendix, or can be deduced from simple equations as follows:

$$A_{is} = 1.16 \times 10^{-3} \mu_{is}^{1/2} \theta_{v,i}^{4/3} \quad (31)$$

$$B_{is} = 0.015 \mu_{is}^{1/4} \quad (32)$$

$$\mu_{is} = \frac{M_i M_s}{M_i + M_s} \quad (33)$$

In Eq. (28), $\tau_{c,i}$ is a correction term for unrealistically large cross section at high temperature regimes. It is calculated as follows:

$$\tau_{c,i} = \frac{1}{c_i \sigma_v N_t} \quad (34)$$

Here, c_i is an average molecular speed of the species i , σ_v is the limiting cross section, and N_t is the number density of the mixture.

$$c_i = \sqrt{\frac{8kT}{\pi m_i}} = \sqrt{\frac{8RT}{\pi M_i}} \quad [m/s] \quad (35)$$

$$\sigma_v = 10^{-21} \left(\frac{50,000}{T} \right)^2 \quad [m^2] \quad (36)$$

$$N_t = \frac{\rho}{M_t} N_A \times 1000 \quad [1/m^3] \quad (37)$$

Considering diffusive nature of vibrational relaxation in high temperature range, a correction term would be applied as follows[38, 39]:

$$W_{v,i} = \rho_i \frac{e_{v,i}(T) - e_{v,i}(T_v)}{\tau_i} \times \left| \frac{T_s - T_v}{T_s - T_{vs}} \right|^{s-1} \quad (38)$$

$$s = 3.5 \times \exp(-5000 / T_s) \quad (39)$$

Here, T_s and T_{vs} are translational-rotational temperature and vibrational temperature right behind the shock. In the computation, T_s is taken to be the peak value after the shock along i direction—surface normal direction with same j index—and T_{vs} is taken to be the vibrational temperature at the same point of the peak T_s .

D. Transport property

In chemically non-equilibrium flow, the transport properties used in Eq. (2) — viscosity, thermal conductivity, and diffusivity—vary with not only temperature, but also species composition. In this study, to obtain transport properties of gas mixture, Wilke’s mixing rule[45] was adopted.

$$\mu = \sum_i \frac{X_i \mu_i}{\Phi_i}, \quad k = \sum_i \frac{X_i k_i}{\Phi_i} \quad (40)$$

$$\Phi_i = \sum_r X_r \left[1 + \sqrt{\frac{\mu_s}{\mu_r}} \left(\frac{M_r}{M_s} \right)^{1/4} \right]^2 \left[\sqrt{8 \left(1 + \frac{M_s}{M_r} \right)} \right]^{-1} \quad (41)$$

Transport properties of each chemical species was obtained by Blottner’s curve[46] fit or Svehla’s table[47, 48]. Detailed values for the transport properties of each species in both methods are described in the appendix.

3.2 Solid Governing Equation

In the experiment, as the temperature of the specimen increases with time and the change of surface temperature influences the boundary layer and the heat transfer rate into the surface. In order to calculate the temperature change of the tungsten specimen with time, a heat conduction equation for axi-symmetric shape were considered.

$$\frac{\partial \rho_s c_s T_s}{\partial t} + \frac{\partial q_{sx}}{\partial x} + \frac{\partial q_{sy}}{\partial y} + \alpha \frac{q_{sy}}{y} = S_s \quad (42)$$

Here, q_{sx} and q_{sy} represent heat transfer to x and y direction respectively by conduction inside tungsten.

$$q_{sx} = -k_s \frac{\partial T_s}{\partial x}, \quad q_{sy} = -k_s \frac{\partial T_s}{\partial y} \quad (43)$$

S_s is a heat source term and equals zero in this study since there is no heat generation phenomenon such as pyrolysis. Since density change due to thermal expansion was ignored, ρ_s is a constant.

3.3 Ablation Model

In this study, an ablation model is applied as a boundary condition at the interface between flow and solid calculation. At the interface, mass and heat transferred and various chemical reactions occur. In the flow solver, a mass balance equation including the chemical ablation model is solved, and the mass fractions and chemical reaction rates are calculated. Based on the calculated reaction rates, the ablation amount at each surface point is decided, then the grid are regenerated with a new surface line. Meanwhile, in the solid solver, the energy balance equation is solved, then surface temperature is calculated.

a. Mass balance at the surface

In this study, we tried to predict ablation rate of tungsten from arc heater experiment with a simplified model. Basic catalytic recombination at the surface, the recombination of oxygen and nitrogen was considered. Total for different tungsten oxides were considered. The reactions between tungsten oxides and the reactions including NO molecules were ignored. The reactions considered in this paper are presented in Table 9. In the table, reaction 1 and 2 represent catalytic recombination of oxygen and nitrogen respectively. Reaction 3–6 represent oxidation of tungsten at the surface. These oxidation reactions are primary cause of ablation at the surface in the range of this study.

Table 9 Surface reactions

No.	Reaction	Reaction energy (kJ/mol of product)
Catalytic recombination		
1	$O_{(g)} + O_{(g)} \leftrightarrow O_{2(g)}$	493.6
2	$N_{(g)} + N_{(g)} \leftrightarrow N_{2(g)}$	941.6
Oxidation		
3	$O_{(g)} + W_{(s)} \leftrightarrow WO_{(g)}$	-150.0
4	$2O_{(g)} + W_{(s)} \leftrightarrow WO_{2(g)}$	466.6
5	$3O_{(g)} + W_{(s)} \leftrightarrow WO_{3(g)}$	1060.3
6	$6O_{(g)} + 2W_{(s)} \leftrightarrow W_2O_{6(g)}$	2690.7

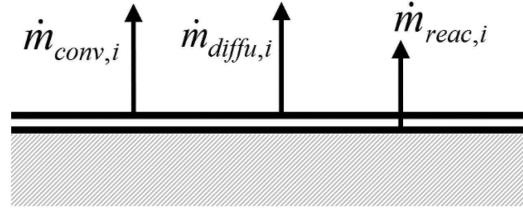


Fig. 28 Mass balance at wall.

Fig. 28 shows mass fluxes flow in and out of the reaction surface. Near the wall where the chemical reaction occurs, the composition of each chemical species changes due to the surface reactions, which result in the mass fraction gradient to surface normal direction. The mass fraction gradients generate the mass fluxes by molecular diffusion. It supplies reactant to the reaction surface and discharges products from the surface. On the surface where only the catalytic recombination occurs without ablation, only the mass fluxes due to diffusion exists. On the other hand, if the solid phase reactant was involved in the reaction, that is, ablation occurs at the surface, mass flow is injected to the flow from the surface, therefore flow velocity at the surface becomes no more zero. In this situation, the mass fluxes of each species generated by the surface reaction should satisfy a mass balance equation as follow.

$$\dot{m}_{reac,i} = \dot{m}_{conv,i} + \dot{m}_{diffu,i} \quad [kg / m^2 s] \quad (44)$$

Here $\dot{m}_{conv,i}$, $\dot{m}_{diffu,i}$, $\dot{m}_{reac,i}$ represent the mass fluxes of species i transported from the surface by convection, diffusion, and surface reaction respectively. If these mass fluxes were summed up for all the chemical species, the new equation established is as follows.

$$\dot{m}_{reac} = \dot{m}_{conv} = \rho_w v_w \quad (45)$$

This is because the sum of the mass fluxes of the chemical species by diffusion is

zero. Therefore, if all of the mass fluxes released by the surface reaction at the wall were summed up, it would become the convective mass flux emitted from the wall, which is equal to the amount of tungsten lost by ablation.

The mass flux by of each chemical species by diffusion can be represented as follows:

$$\dot{m}_{diffu,i} = -\rho_w D_i \frac{\partial \alpha_i}{\partial n} \quad (46)$$

On a structured grid, $\frac{\partial \alpha_i}{\partial n}$ can be calculated as follows using the values at the first cell and the wall.

$$\dot{m}_{diffu,i} = -\rho_w D_i \frac{(\alpha_{c,i} - \alpha_{w,i})}{\Delta n} \quad (47)$$

Here, subscripts c and w represent the cell center and wall respectively. The direction of mass flux by diffusion in is from the wall as drawn in Fig. 28, and Δn is the distance from the center of the first cell to the wall.

The mass flux of each chemical species by convection is expressed as the product of the mass fraction to the total mass flux, and can be written as follows:

$$\dot{m}_{conv,i} = \rho_w v_w \alpha_{w,i} = \dot{m}_{conv} \alpha_{w,i} = \dot{m}_{reac} \alpha_{w,i} \quad (48)$$

That is, once the mass flux by the reaction is determined, the species mass flux by convection can be expressed as a function of the surface mass fraction of each species.

Lastly, species mass flux by surface reaction can be separated into mass flux by catalytic recombination and oxidation.

$$\dot{m}_{reac,i} = J_i^{oxi} + J_i^{cat} \quad [kg / m^2 s] \quad (49)$$

In the above equation, J_i^{oxi} and J_i^{cat} represent mass fluxes of species i generated by oxidation and catalytic recombination respectively. In this study, every J can be represented with surface mass fraction of species. First, catalytic recombination

includes surface reactions of oxygen and nitrogen as shown in Table 9. For example, recombination of O that is the forward reaction of the above equation reduces O atoms and produces O₂ molecules at the surface. The reverse equation is the opposite. As a result, the mass fluxes of O and O₂ generated at the surface by the above reaction are expressed as follows.

$$J_O^{cat} = -\frac{1}{4}\eta_O^{cat}\rho_w\alpha_{w,O}C_O + \frac{1}{4}\eta_{O_2}^{cat}\rho_w\alpha_{w,O_2}C_{O_2} \quad (50)$$

$$J_{O_2}^{cat} = \frac{1}{4}\eta_O^{cat}\rho_w\alpha_{w,O}C_O - \frac{1}{4}\eta_{O_2}^{cat}\rho_w\alpha_{w,O_2}C_{O_2} \quad (51)$$

J_N^{cat} , $J_{N_2}^{cat}$ are expressed in the same manner with Eq. (50) and Eq. (51).

The mass flux due to oxidation is also calculated in a similar way. In the oxidation, since oxygen atom and molecule can produce several oxides, following generalized chemical equation is considered.



Total mass flux of O due to oxidation is represented by the sum of the fluxes due to the oxidation reactions that produce each oxide and the reverse reactions of them.

$$J_O^{oxi} = -\frac{1}{4}\sum_x(\eta_{O,x}^{oxi}\rho_w\alpha_{w,O}C_O - \frac{am_O}{m_x}\eta_{x,O}^{oxi}\rho_w\alpha_{w,x}C_x) \quad (54)$$

And the mass flux of a tungsten oxide due to oxidation is expressed as follows.

$$J_x^{oxi} = -\frac{1}{4}\left(\eta_{x,O}^{oxi}\rho_w\alpha_{w,x}C_x - \frac{m_x}{am_O}\eta_{O,x}^{oxi}\rho_w\alpha_{w,O}C_O\right) \quad (55)$$

In the equations above, $\frac{1}{4}\rho_w\alpha_{w,i}C_i$ represents the arrival rate of mass fluxes of i species striking the wall per unit surface area per second. C_i represents average molecular speed, and it is calculated as follows:

$$C_i = \sqrt{\frac{8kT}{\pi m_i}} = \sqrt{\frac{8\bar{R}T}{\pi M_i}} \quad [m / s] \quad (56)$$

$$M_i = m_i N_A \quad [kg / kmol] \quad (57)$$

Since four oxidation reactions that generate different oxides, WO, WO₂, WO₃, and W₂O₆, were considered, the total mass flux of oxygen by oxidation reactions can be calculated as the sum of mass fluxes by each oxidation reaction.

$$J_O^{oxi} = J_{O,WO}^{oxi} + J_{O,WO_2}^{oxi} + J_{O,WO_3}^{oxi} + J_{O,W_2O_6}^{oxi} = \sum_x J_{O,x}^{oxi} \quad (58)$$

The mass flux of each species can be obtained by multiplying the reaction probability η_i^r that the atoms or molecules of i species will participate in the r reactions with the incident mass fluxes. For example, in Eq. (50), η_O^{cat} is the reaction probability that O particles incident on the surface will participate in the catalytic recombination that produces O₂ molecules, and its value varies depending on the surface conditions, including material, roughness, and temperature of the surface. In the case of a fully catalytic wall without oxidation, the value of η_O^{cat} is unity, while for a non-catalytic wall, it is zero.

$$\begin{cases} \eta_O^{cat} = 1 & (\text{fully catalytic without oxidation}) \\ \eta_O^{cat} = 0 & (\text{non-catalytic}) \end{cases} \quad (59)$$

Coefficients of reverse reaction, $\eta_{O_2}^{cat}$, is calculated with the equilibrium coefficients from the JANAF Table [49]. Since the rate of forward and reverse reaction must be the same when the chemical equilibrium state is reached, following equation can be established.

$$\frac{1}{4} \eta_O^{cat} \rho_w \alpha_{w,O}^E C_O = \frac{1}{4} \eta_{O_2}^{cat} \rho_w \alpha_{w,O_2}^E C_{O_2} \quad (60)$$

If we sort the shared terms and rewrite the equation,

$$\eta_{O_2}^{cat} = \eta_O^{cat} \left(\frac{P_O}{P_{O_2}} \right)^E \sqrt{\frac{M_O}{M_{O_2}}} \quad (61)$$

where,

$$\rho_w \alpha_{w,i} = \rho_{w,i} = \frac{P_i}{(\bar{R} / M_i) T} \quad (62)$$

Here, $P_O^E / P_{O_2}^E$ can be found from the partial pressure of each species at the surface and equilibrium constant on JANAF table.

In the Eq. (50) and Eq. (51), substituting $\gamma_{s,i}$ for the terms multiplied before alpha yields:

$$J_O^{cat} = \gamma_{O,O}^{cat} \alpha_{w,O} + \gamma_{O_2,O}^{cat} \alpha_{w,O_2} \quad (63)$$

$$J_{O_2}^{cat} = \gamma_{O,O_2}^{cat} \alpha_{w,O} + \gamma_{O_2,O_2}^{cat} \alpha_{w,O_2} \quad (64)$$

Similarly, mass fluxes of oxygen and tungsten oxides by oxidation can be summarized with α and γ as follows.

$$J_O^{oxi} = \sum_x \left(\gamma_{O,x}^{oxi} \alpha_{w,O} + \gamma_{x,O}^{oxi} \alpha_{w,x} \right) \quad (65)$$

$$J_x^{oxi} = \gamma_{O,x}^{oxi} \alpha_{w,O} + \gamma_{x,O}^{oxi} \alpha_{w,x} \quad (66)$$

In addition, unlike in catalytic recombination, mass loss of tungsten solid occurs due to oxidation. The mass flux of tungsten consumed by surface reactions is calculated as follows.

$$J_W^{oxi} = \dot{m}_{reac} = \frac{1}{4} \rho_w \sum_x \left(\frac{m_x - am_o}{am_o} \eta_{O,x}^{oxi} C_O \alpha_O - \frac{m_x - am_o}{m_x} \eta_{x,O}^{oxi} C_x \alpha_x \right) \quad (67)$$

In the above equation, substituting delta for the terms multiplied before alpha yields:

$$\dot{m}_{reac} = \delta_O \alpha_O + \sum_x \delta_x \alpha_x = \sum_s \delta_s \alpha_s \quad (68)$$

Where,

$$\delta_O = \frac{1}{4} \sum_x \left(\frac{m_x - am_O}{am_O} \eta_{O,x}^{oxi} \rho_w C_O \right) \quad (69)$$

$$\delta_{O_2} = \frac{1}{4} \sum_x \left(\frac{m_x - cm_{O_2}}{cm_{O_2}} \eta_{O_2,x}^{oxi} \rho_w C_{O_2} \right) \quad (70)$$

$$\delta_x = -\frac{1}{4} \frac{m_x - am_O}{m_x} \eta_{x,O}^{oxi} \rho_w C_x \quad (71)$$

The mass fluxes of each chemical species due to both oxidation and catalytic recombination can be summarized with $\gamma_{s,i}$ as follows.

$$\dot{m}_{reac,i} = \sum_s \gamma_{s,i} \alpha_{w,s} \quad (72)$$

$$\gamma_{s,i} = \gamma_{s,i}^{cat} + \gamma_{s,i}^{oxi} \quad (73)$$

Consequently, $\gamma_{s,i} \alpha_{w,s}$ is defined as the amount of mass flux of species i produced by species s .

Now, by substituting the above equations expressed with the species mass fraction, α_i , for the mass balance equation, the following equations are established.

$$\sum_s \gamma_{s,i} \alpha_{w,s} = \left(\sum_s \delta_s \alpha_{w,s} \right) \alpha_{w,i} - \rho D_i \frac{\alpha_{c,i} - \alpha_{w,i}}{\Delta n} \quad (74)$$

$$\left(\frac{\rho D_i}{\Delta n} + \sum_s \delta_s \alpha_{w,s} \right) \alpha_{w,i} - \sum_s \gamma_{s,i} \alpha_{w,s} = \frac{\rho D_i}{\Delta n} \alpha_{c,i} \quad (75)$$

Above equations are nonlinear differential equations, thus we linearized them by replacing $\sum_s \delta_s \alpha_{w,s}$ inside the parenthesis to the value of former time step and performed iterative calculation for $\alpha_{w,i}$.

$$\left(\frac{\rho D_i}{\Delta n} + \sum_s \delta_s \alpha_{w,s}^{n-1} \right) \alpha_{w,i}^n - \sum_s \gamma_{s,i} \alpha_{w,s}^n = \frac{\rho D_i}{\Delta n} \alpha_{c,i} \quad (76)$$

Eq. (76) is N simultaneous equations for the mass fractions of chemical species at

the surface and expressed in matrix form as follows.

$$A\bar{x} = \bar{b} \quad (77)$$

$$A = \begin{bmatrix} \frac{\rho_w D_1}{\Delta n} + \sum_s (\delta_s \alpha_{w,s}^{n-1}) - \gamma_{1,1} & \cdots & -\gamma_{N,1} \\ \vdots & \ddots & \vdots \\ -\gamma_{1,N} & \cdots & \frac{\rho_w D_N}{\Delta n} + \sum_s (\delta_s \alpha_{w,s}^{n-1}) - \gamma_{N,N} \end{bmatrix},$$

$$\bar{x} = \begin{pmatrix} \alpha_{w,1} \\ \vdots \\ \alpha_{w,N} \end{pmatrix}, \quad \bar{b} = \begin{pmatrix} \frac{\rho_w D_1}{\Delta n} \alpha_{c,1} \\ \vdots \\ \frac{\rho_w D_N}{\Delta n} \alpha_{c,N} \end{pmatrix} \quad (78)$$

By solving Eq. (77), we can find the mass fraction of each species at the surface.

B. Ablation models for tungsten and tungsten composites

Pure tungsten

In case of pure tungsten, since a total of four oxidation reactions are considered, four different values of reaction coefficient denoted as $\eta_{O,x}^{oxi}$ for each oxide x produced by oxidation are needed. These reaction coefficients vary mainly depending on the surface temperature, yet, their exact values are not clearly known. In the present study, it was impossible to accurately model the reaction rate for each oxidation reaction; thus, we assumed that oxygen mass fluxes incident on the surface were equally consumed to produce four different tungsten oxides. That is, each reaction coefficient is simply a quarter of the total oxidation coefficient.

$$\eta_{O,x}^{oxi} = \frac{1}{4} \eta_O^{oxi} \quad (79)$$

The total oxidation coefficient, $\eta_{O,x}^{oxi}$, was expressed as a function of surface temperature in Arrhenius form. Consequently, in the present study, an oxidation coefficient for pure tungsten was modeled as follows.

$$\eta_O^{oxi} = C_A \times \min[1.0, 31250 \times (T_w / 1000)^{-C_B} \exp(-27610 / T_w)] \quad (80)$$

Here, coefficients C_A and C_B was deduced to 0.3 and 0.8 respectively, by comparing several results of recession rate over time calculated with different coefficients to that of experimental results shown in Fig. 15. Graphs of various oxidation probability functions with different values of C_A and C_B are drawn in Fig. 29.

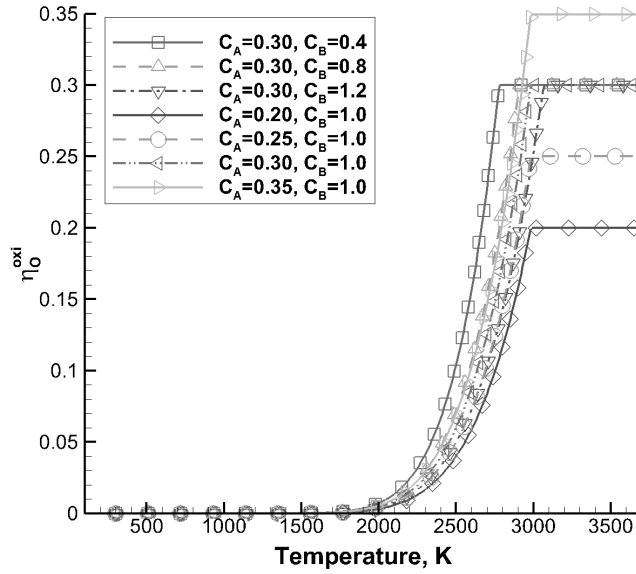


Fig. 29 Graphs of the oxidation probability functions with different coefficients.

Tungsten composites

From the ablation test with W-HfC and W-ZrC, it was confirmed that adding those reinforcements suppresses the ablation of tungsten, and the effect of them increases as the content of the reinforcement increases. In this study, the thermochemical ablation model for those tungsten composites are expressed as a form multiplying a weighting factor about reinforcement volume contents to pure tungsten's oxidation probability function.

$$\left[\eta_O^{oxi} \right]_{Composite} = \omega(f_{re}) \times \left[\eta_O^{oxi} \right]_{PureW} \quad (81)$$

Here, $\omega(f_{re})$ represents weighting function for the volume percent of reinforcement, f_{re} , deduced from the ablation test results of W-HfC and W-ZrC. The weighting factor for each composites are expressed as follows.

$$\omega(f_{re}) = 1.1^{-(f_{re}+5.1862)} + 0.39 \quad (\text{for W-HfC}) \quad (82)$$

$$\omega(f_{re}) = 1.05^{-(f_{re}+24.677)} + 0.7 \quad (\text{for W-ZrC}) \quad (83)$$

These models for tungsten composites were deduced from the total ablation rate of the composites with different contents up to 30vol%, thus they are applicable for the contents of reinforcement less than 30vol%. Additionally, as observed in the W-ZrC ablation test with different manufacturing methods, there can be a difference of ablation speeds depending on the composite's manufacturing method. To build a general ablation model for these composites, additional tests and corresponding validations and corrections should be performed for the larger contents of HfC and ZrC reinforcements.

C. Energy balance at the surface

Ablation simulation could be divided into a conventional flow analysis and a solid internal temperature analysis. To calculate the surface temperature, which is the interface of the flow and the solid, following energy balance equations were considered at the surface.

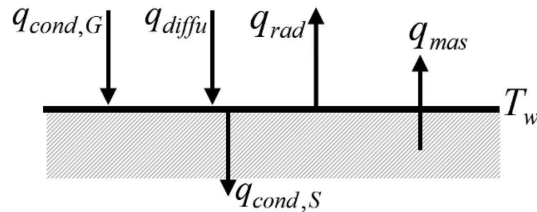


Fig. 30 Energy balance at wall.

Fig. 30 represents energy balance at the solid surface between heat fluxes come in and go out of the wall. From the energy balance at the wall, we can figure out the

temperature of the surface over time in the solid solver. As shown in the figure, the heat flux from the surface into the solid should be equal to the sum of the incoming heat fluxes to the surface minus the amount of heat transferred out from the surface by cooling. This energy balance equation at the surface can be represented as follows.

$$q_{cond,S} = q_{cond,G} + q_{diffu} - q_{rad} - q_{mas} \quad (84)$$

This energy balance equation was solved iteratively by Newton method for a variable, T_w .

$$F(T_w) = q_{cond,S} - q_{cond,G} - q_{diffu} + q_{rad} + q_{mas} \quad (85)$$

$$T_w^{n+1} = T_w^n - \frac{F(T_w)}{F'(T_w)} \quad (86)$$

To solve this equation, we need to express all the heat flux terms and the derivative of them for T_w .

First, $q_{cond,S}$ and $q_{cond,G}$ represent heat fluxes due to conduction inside solid and gas near the surface respectively. They are simply calculated from the temperature distribution as follows.

$$q_{cond,S} = -k_S \left(\frac{\partial T_S}{\partial n} \right)_w \quad (87)$$

$$q_{cond,G} = -k_G \left(\frac{\partial T_G}{\partial n} \right)_w \quad (88)$$

q_{diffu} , q_{rad} , and q_{mas} represent heat fluxes due to species diffusion, radiation, and heat of formation when the solid species turn into gas state by the reaction.

$$q_{diffu} = \left(\sum_i \rho_G D_i \frac{\partial \alpha_i}{\partial n} h_{G,i} \right)_w \quad (89)$$

$$q_{rad} = \varepsilon \sigma T_w^4 \quad (90)$$

$$q_{mas} = \sum_i \dot{m}_{conv,i} h_{G,i} - \rho_w v_w h_S = \rho_w v_w \left(\sum_i \alpha_{w,i} h_{G,i} - h_S \right) \quad (91)$$

In Eq. (84), $q_{cond,G}$, q_{diffu} , and q_{mas} are calculated as shown in Eqs. (88), (89), and (91) from the flow solver and treated as constants when the energy balance equation are solved to find the boundary conditions for solid solver iteration. Meanwhile, $q_{cond,S}$ and q_{rad} are calculated in the solid solver and they are expressed as functions of the surface temperature, T_w . Considering grid system which is not normal to the surface, $q_{cond,S}$ was calculated as follows. First, near the surface, we assumed temperature distribution as a function as follows.

$$T_s = C_1x + C_2y + C_3 \quad (92)$$

Then, from the Eq. (87), the heat flux by conduction inside solid surface becomes,

$$q_{cond,S} = -k_s \left(C_1 \frac{\partial x}{\partial n} + C_2 \frac{\partial y}{\partial n} \right) \quad (93)$$

The coefficients C_1 and C_2 in Eq. (93) are calculated from the temperature at three different points including a point at the surface as shown in Fig. 31.

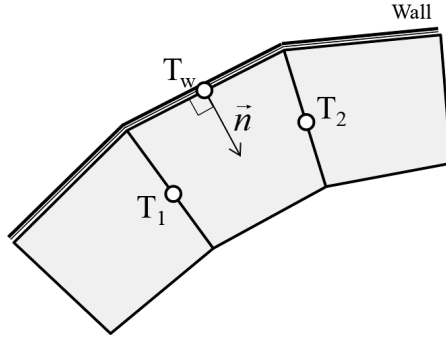


Fig. 31 Points used to calculate the temperature gradient at the surface.

If we assign the values of temperature and location of those points to Eq. (92), following matrix equations are established.

$$\begin{bmatrix} x_1 & y_1 & 1 \\ x_2 & y_2 & 1 \\ x_w & y_w & 1 \end{bmatrix} \begin{pmatrix} C_1 \\ C_2 \\ C_3 \end{pmatrix} = \begin{pmatrix} T_1 \\ T_2 \\ T_w \end{pmatrix} \quad (94)$$

$$\begin{pmatrix} C_1 \\ C_2 \\ C_3 \end{pmatrix} = \begin{bmatrix} x_1 & y_1 & 1 \\ x_2 & y_2 & 1 \\ x_w & y_w & 1 \end{bmatrix}^{-1} \begin{pmatrix} T_1 \\ T_2 \\ T_w \end{pmatrix} = B \begin{pmatrix} T_1 \\ T_2 \\ T_w \end{pmatrix} = \begin{bmatrix} b_{11} & b_{12} & b_{13} \\ b_{21} & b_{22} & b_{23} \\ b_{31} & b_{32} & b_{33} \end{bmatrix} \begin{pmatrix} T_1 \\ T_2 \\ T_w \end{pmatrix} \quad (95)$$

Finally, $q_{cond,S}$ becomes,

$$q_{cond,S} = -k_S \left((b_{11}T_1 + b_{12}T_2 + b_{13}T_w) \frac{\partial x}{\partial n} + (b_{21}T_1 + b_{22}T_2 + b_{23}T_w) \frac{\partial y}{\partial n} \right) \quad (96)$$

Derivative of $q_{cond,S}$ and q_{rad} for T_w are calculated as follows.

$$\frac{\partial q_{cond,S}}{\partial T_w} = -k_S \left(b_{13} \frac{\partial x}{\partial n} + b_{23} \frac{\partial y}{\partial n} \right) \quad (97)$$

$$\frac{\partial q_{rad}}{\partial T_w} = 4 \times \epsilon \sigma T_w^3 \quad (98)$$

Because other heat fluxes are assumed to be independent to T_w , their derivatives for T_w equal zero.

3.4 Numerical Schemes

Coupling of flow and solid solver for ablation analysis

To solve the above mentioned governing equations, various numerical methods were applied. In this paper, the numerical solver consists of the flow analysis part and the solid analysis part. In the flow solver, surface temperature of the specimen is the boundary condition which is calculated from the solid analysis. Conversely, during the solid analysis, the surface heat transfer rate calculated from flow analysis is applied as a boundary condition. Since the surface temperature and the heat transfer rate influences each other, the coupling between the flow analysis and the solid analysis is necessary in order to calculate temperature change over time.

In this paper, the flow solver performs time integration with relatively larger time step than solid solver by applying dual-time stepping method [50]. Flow solver calculates the surface heat transfer rate from the converged solution with the fixed surface temperature value at each physical time step.

Meanwhile, the solid solver calculates unsteady solution over time applying the heat flux distribution along the surface as a boundary condition that is interpolated from two different time steps in the flow analysis. As shown in Fig. 32, flow calculation at n th time step and solid calculation from $n-1$ th to n th physical time step repeated until the converged T_w is obtained. After the T_w was converged, $n+1$ th flow calculation with initial boundary condition with extrapolated T_w is progressed and the whole process repeated. This iterative coupling of solid and flow analysis is possible only if T_w and q_w are in negative feedback.

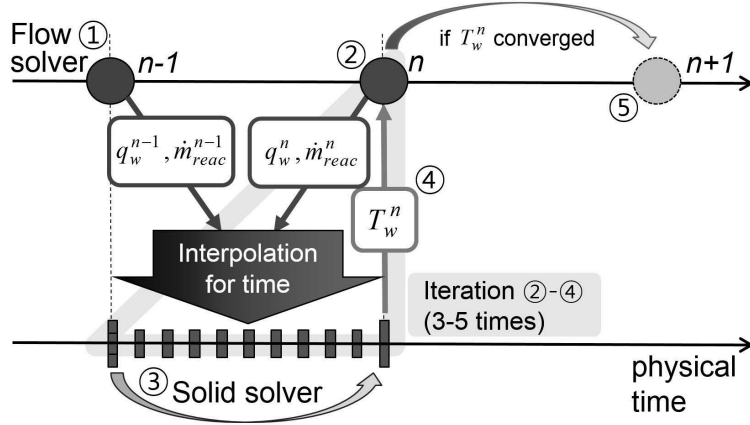


Fig. 32 Iteration strategy of the ablation solver.

Numerical schemes for flow solver

As mentioned above, dual-time stepping method was applied in the flow solver. Applying dual time stepping method, the flow was assumed to be steady state: thus LU-SGS [51] was applied to find a converged solution as a time-integration scheme. In order to find solutions for the non-equilibrium compressible supersonic flow, AUSMPW+ scheme [52-55] and 2nd order MUSCL approach were employed. Viscous fluxes were calculated with 2nd order central differencing scheme. In addition, in order to capture the shock and calculate the surface heat transfer rate accurately and stably, shock-aligned grid technique (SAGT) [56] was applied. The SAGT aligned the grid system automatically along the shock for different grids.

Determining of time step for chemically reacting non-equilibrium flow.

$$\frac{1}{\Delta t} = \frac{1}{\Delta t_{euler}} + \frac{1}{\Delta t_{vis}} + \frac{1}{\Delta t_{chem}} \quad (99)$$

$$\frac{1}{\Delta t_{euler}} = |U| + c\sqrt{\zeta_x^2 + \zeta_y^2} + |V| + c\sqrt{\eta_x^2 + \eta_y^2} \quad (100)$$

$$\frac{1}{\Delta t_{vis}} = \frac{4\mu}{\rho Re} \left[\frac{\gamma}{Pr} (\zeta_x^2 + \zeta_y^2 + \eta_x^2 + \eta_y^2) + \frac{7}{3} (\zeta_x \eta_x + \zeta_y \eta_y) + \frac{1}{3} \sqrt{(\zeta_x^2 + \zeta_y^2)(\eta_x^2 + \eta_y^2)} \right] \quad (101)$$

When we consider the non-equilibrium chemical reactions, the time step for stable convergence is given by [57].

$$\Delta t_{chem} = 0.1 \times \min \left(\left| \frac{\rho_i}{W_i} \right| \right) \quad (102)$$

Here, the factor 0.1 is a coefficients for stability in the reference [57].

Schemes for solid solver

In order to solve a 2-Dimensional and axi-symmetric heat conduction equation, Alternating Direction Implicit (ADI) method was applied. Using Crank-Nicholson discretization and considering metric in Cartesian grid, the governing equation of solid solver could be solved accurately and stably.

$$\frac{\partial \rho_s c_s T_s}{\partial t} + \frac{\partial q_{sx}}{\partial x} + \frac{\partial q_{sy}}{\partial y} + \alpha \frac{q_{sy}}{y} = S_s \quad (103)$$

$$\rho_s c_s \frac{\Delta T_s}{\Delta t} + \frac{1}{2} \left[\frac{\partial (\Delta q_{sx})}{\partial x} + \frac{\partial (\Delta q_{sy})}{\partial y} + \alpha \frac{\Delta q_{sy}}{y} \right] = S_s - \left(\frac{\partial q_{sx}^n}{\partial x} + \frac{\partial q_{sy}^n}{\partial y} + \alpha \frac{q_{sy}^n}{y} \right) \quad (104)$$

$$\frac{\partial q_{sx}}{\partial x} = \zeta_x (q_{sx,i+1/2} - q_{sx,i-1/2}) + \eta_x (q_{sx,j+1/2} - q_{sx,j-1/2}) \quad (105)$$

$$\frac{\partial q_{sy}}{\partial y} = \zeta_y (q_{sy,i+1/2} - q_{sy,i-1/2}) + \eta_y (q_{sy,j+1/2} - q_{sy,j-1/2}) \quad (106)$$

$$q_{sx,i+1/2} = -k_{i+1/2} \left[\zeta_{x,i+1/2} (T_{i+1} - T_i) + \frac{1}{2} \eta_{x,i+1/2} (T_{i+1,j+1} + T_{j+1} - T_{i+1,j-1} - T_{j-1}) \right] \quad (107)$$

$$q_{sx,j+1/2} = -k_{j+1/2} \left[\frac{1}{2} \zeta_{x,j+1/2} (T_{i+1,j+1} + T_{i+1} - T_{i-1,j-1} - T_{i-1}) + \eta_{x,j+1/2} (T_{j+1} - T_j) \right] \quad (108)$$

$$q_{sy,i+1/2} = -k_{i+1/2} \left[\zeta_{y,i+1/2} (T_{i+1} - T_i) + \frac{1}{2} \eta_{y,i+1/2} (T_{i+1,j+1} + T_{j+1} - T_{i+1,j-1} - T_{j-1}) \right] \quad (109)$$

$$q_{sy,j+1/2} = -k_{j+1/2} \left[\frac{1}{2} \zeta_{y,j+1/2} (T_{i+1,j+1} + T_{i+1} - T_{i-1,j-1} - T_{i-1}) + \eta_{y,j+1/2} (T_{j+1} - T_j) \right] \quad (110)$$

Heat fluxes at the points $(i-1/2)$ and $(j-1/2)$ are calculated similarly. Unlike the general discretization in the uniform grid, the values at $(i-1,j-1)$, $(i-1,i+1)$, $(i+1,j-1)$,

and $(i+1, j+1)$ exist. In this study, these values are replaced with the values of neighboring points.

Shock Aligned Grid Technique (SAGT)

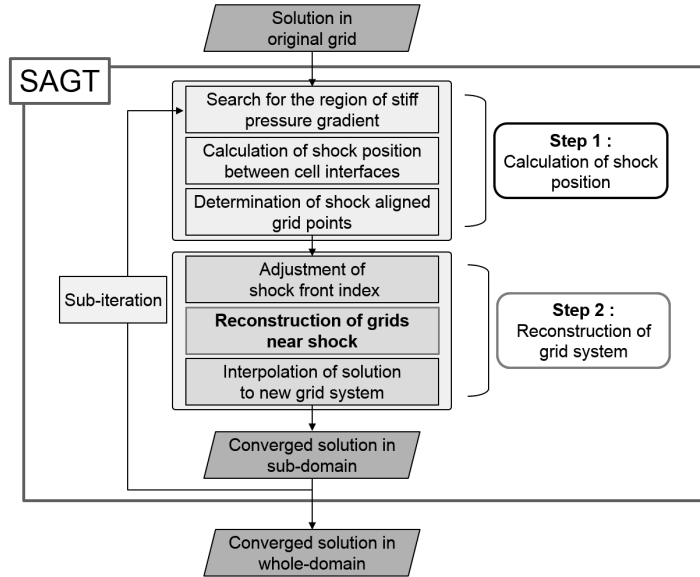


Fig. 33 Flow chart of SAGT.

Among the whole process of the ablation analysis, one of the essential parts which determine the accuracy is to calculate heat transfer rate accurately. The calculation of accurate heat transfer rate at the surface in the problem including strong shock and high enthalpy flow demands more fine and well generated grid system than the calculation of aerodynamic coefficients such as surface pressure coefficients. Especially, when the shock does not coincide with the grid line, the error occurred through the shock wave are transferred to the stagnation point, then the accuracy of heat transfer rate increased and convergence of the calculation decreased. In a steady simulation, these problems can be solved by regenerating grids along the shock manually through a few repeated calculation. However, in ablation analysis, the shape of surface and the grid around the specimen change at every time step. Since it is impossible to regenerate grid manually at every time step, about 20–100 steps,

grid regenerating scheme was needed. Applying SAGT, the grid system was automatically regenerated and refined along the shock.

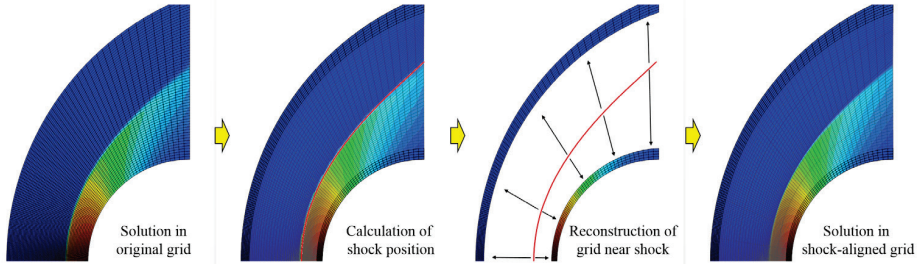


Fig. 34 Grid deformation process of SAGT.

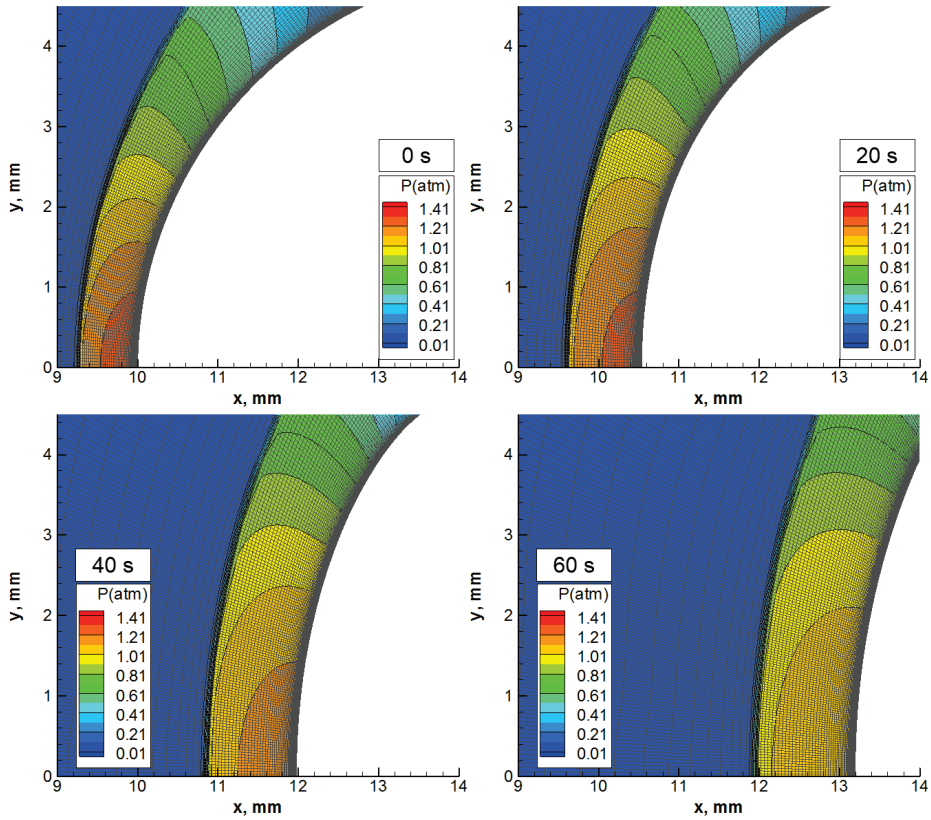


Fig. 35 SAGT applied during an ablation calculation.

Chapter 4. Numerical Results

4.1 Non-equilibrium flow solver validation

Gokcen's Arc Jet Case

In order to validate chemical reaction model and two-temperature model to consider non-equilibrium behavior of the flow in ablation tests, Gokcen's arc jet simulation results [58] was used. In the reference, the flow over a hemispherical heat transfer probe of 0.476 cm radius was considered. In order to establish a frozen boundary layer flow, the freestream density of the gas is decreased and the nose radius is increased in a manner to keep the binary scaling factor ($\rho_\infty R$) constant. In the reference, the nose radius was set to 1 m. Eleven chemical species of air (N, O, NO, N₂, O₂, N⁺, O⁺, NO⁺, N₂⁺, O₂⁺, e⁻) and the reactions between these species were considered. Park's reaction rate coefficients [37] and two-temperature model [39] were adopted.

Surface temperature was set to 293 K, and fully-catalytic wall conditions was calculated. The flow conditions are listed in Table 10.

Table 10 Freestream flow conditions of the 7.2 MJ/kg arc jet

Parameter	Value
h_0 , MJ/kg	7.2
u_∞ , m/s	2780
p_∞ , Pa	1.403E+02
ρ_∞ , kg/m ³	2.267E-04
T_∞ , K	2050
$T_{v\infty}$, K	2050
α_N	0
α_O	0.0520
α_{NO}	0.0670
α_{N_2}	0.7367*
α_{O_2}	0.1443

*In the reference, it is written with 0.7637, which makes the sum of mass fraction to 1.027.

Fig. 36 shows a grid system used in the calculation. The number of grid points is 101 in the direction normal to the wall and 61 along the surface.

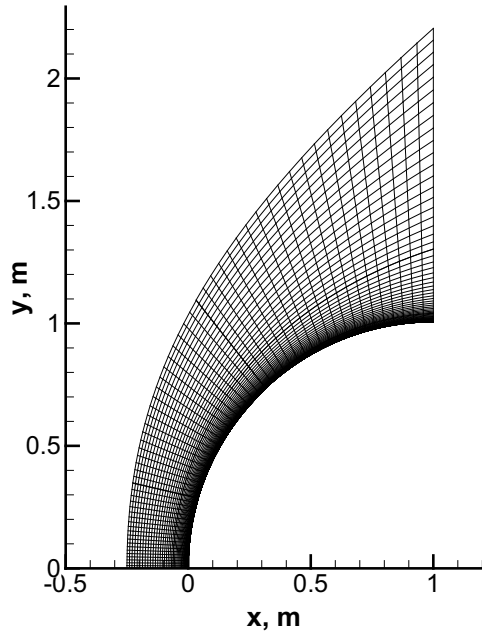


Fig. 36 Initial grid system for Gokcen's case.

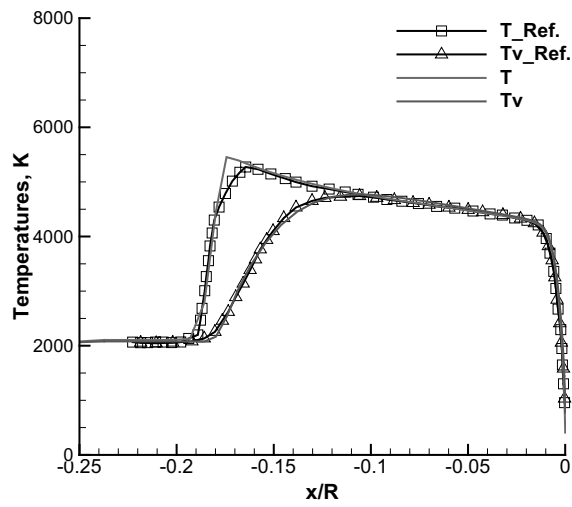


Fig. 37 Translational and rotational temperature along the centerline.

In order to check the validity of a two-temperature model applied in the present program for the calculation of non-equilibrium flow, temperatures along the centerline were compared to the reference value and they are drawn in Fig. 37. As

shown in the figure, both translational and rotation temperature calculated by the present program were well-matched with those of the reference.

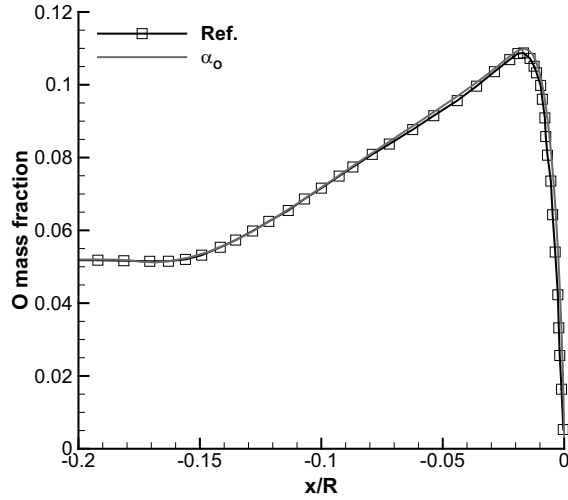


Fig. 38 Mass fraction of oxygen along the centerline.

Similarly, to check the chemical reaction model in non-equilibrium solver, mass fraction of oxygen along the centerline was compared in Fig. 38. Calculated mass fraction also well matched with the reference value.

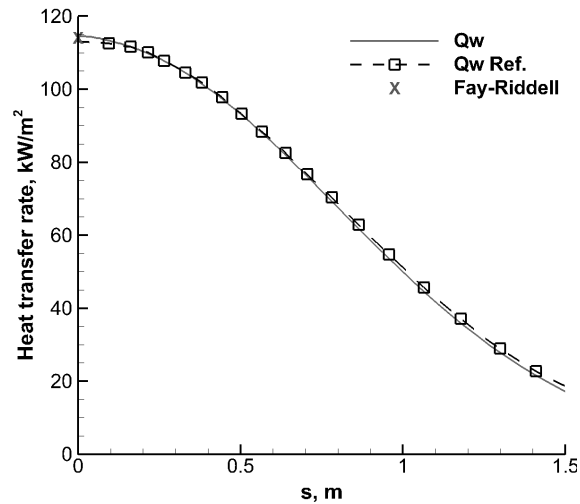


Fig. 39 Surface heat transfer rate.

Lastly, heat transfer distributions along the surface from the stagnation point were compared and they are shown in Fig. 39. In addition, the value of stagnation point heat transfer rate calculated by the relation of Fay-Riddell [31] was also denoted. In the case of frozen boundary layer with a fully catalytic wall, Fay-Riddell's relation for the stagnation heat transfer rate on spherical nose is expressed as follows.

$$q_w = 0.76Pr^{-0.6}(\rho_e \mu_e)^{0.4}(\rho_w \mu_w)^{0.1} \sqrt{\left(\frac{du_e}{dx}\right)_s} (h_{0e} - h_w) \left[1 + (Le^{0.52} - 1) \left(\frac{h_d}{h_{0e}}\right)\right] \quad (111)$$

It was confirmed that the heat transfer distribution calculated by the present program and the value of the reference were well matched each other.

Suzuki Arc Jet Ablation Case

In order to validate the developed program, another validation case [59] was tested. In the reference, ablation tests on carbon phenolic specimen for 30 seconds were conducted in 1 MW arc-jet and numerical simulations for the test condition were conducted. The flow conditions of the reference are tabulated in Table 11.

Table 11 Freestream condition of Suzuki case

Parameter	Value
Density, kg/m ²	2.122x10 ⁻⁴
Velocity, m/s	4956
Translational temperature, K	562.0
Vibrational temperature, K	3377.0
Total enthalpy, MJ/kg	25.2
Pressure, Pa	50.35
α_N	0.24688
α_O	0.23286
α_{NO}	0.00011
α_{N2}	0.52014
α_{O2}	0.00001

The grid system for ablation analysis was shown in Fig. 40. Separated two grid systems were used: one for the flow calculation and another for the solid calculation. Shape of the solid mesh is the same as the specimen shape and consist of 80×60 cells. Flow mesh consist of 80×100 cells and share the grid points with the solid mesh at

the surface line.

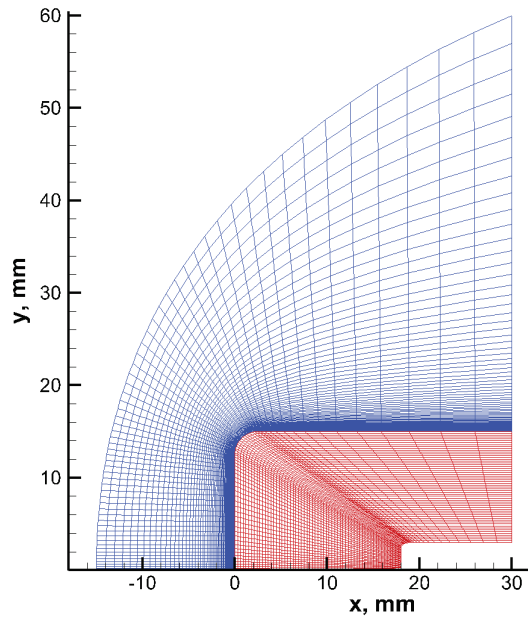


Fig. 40 Grid system for Suzuki case.

Heat transfer rate at the surface is affected by errors generated in shock region. In order to minimize the errors occurring at shock region and to obtain accurate wall heat flux, SAGT was applied. Fig. 41 shows pressure contours in both original and shock aligned grid. In the right figure, grid system aligned to the shock line can be observed.

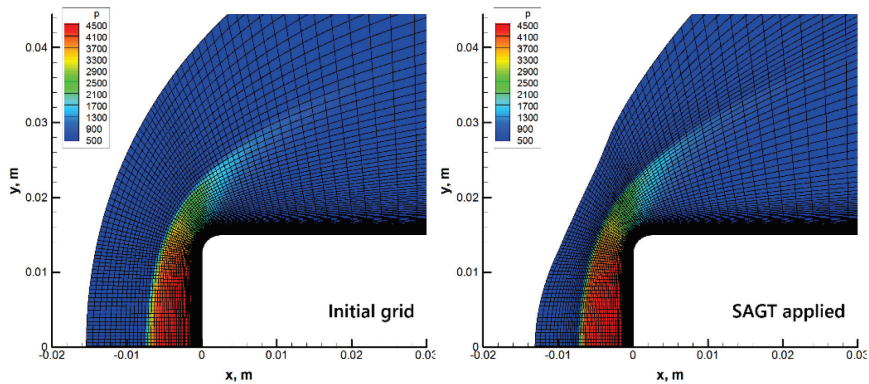


Fig. 41 Pressure contour in original grid (left) and SAGT applied grid (right).

Fig. 42 shows calculated convective heat flux along the surface line in initial state compared with that of the reference. As shown in the figure, heat flux distribution was in a good agreement. At the stagnation point, the value of heat flux was greater than that of the reference for only about 2 %.

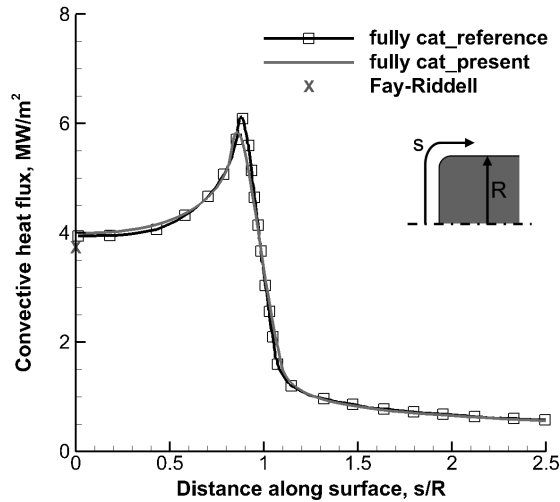


Fig. 42 Heat transfer distribution along the surface.

Fig. 43 shows the net heat flux at the stagnation point at each time step. It is the highest at initial and decreases along time. When a specimen is heated, surface temperature increases and convective heat flux decreases along time, while, radiative cooling and heat transfer by mass flux increases. As a result, the net heat flux and surface temperature converges to a certain value as time passes. As shown in the figure, the net heat flux of the present calculation was slightly higher than the value of the reference. At 30 seconds, the test was over and convective heat flux was assumed to be zero, then the specimen surface was cooled by radiation. During the whole process including ablation and cooling, stagnation point heat flux calculated in the present study was pretty well matched to the reference value, considering the uncertainty of high temperature thermal properties of the material.

In Fig. 44, surface line at 30 sec were compared to the reference. The recession by

ablation was slightly greater in the present result. As mentioned above, these disagreement might have been caused by thermal properties of the material. From the above results, it was observed that despite of the uncertainty in thermal properties, the present ablation analysis program predicts surface heat transfer rate and ablation rate quite well.

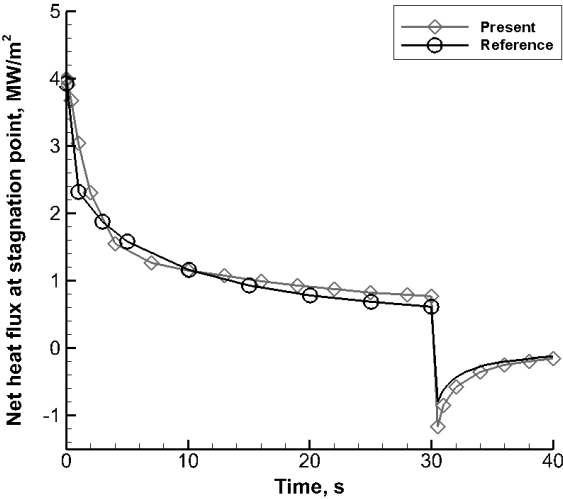


Fig. 43 The net heat flux at stagnation point along time.

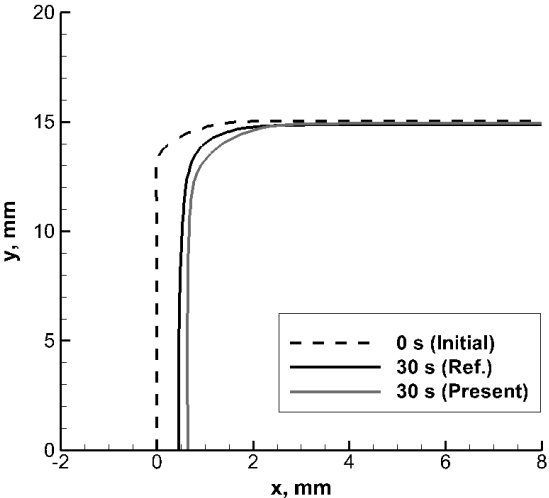


Fig. 44 Surface recession at t = 30 sec.

4.2 Numerical calculation on ablation test conditions

Before ablation simulations were conducted, flow conditions of pure tungsten tests and heat transfer rate along the surface was calculated. Fig. 45 shows grid systems used to calculate the heat transfer distribution at the surface of pure tungsten specimens. In the figure, grid (a) was used to calculate Base cases. Grid (b) was used for VM, VC, and Dist1 cases, (c) for Dist2, and (d) for Dist3. Those grids have different nozzle sizes and distances between the nozzle and the specimen.

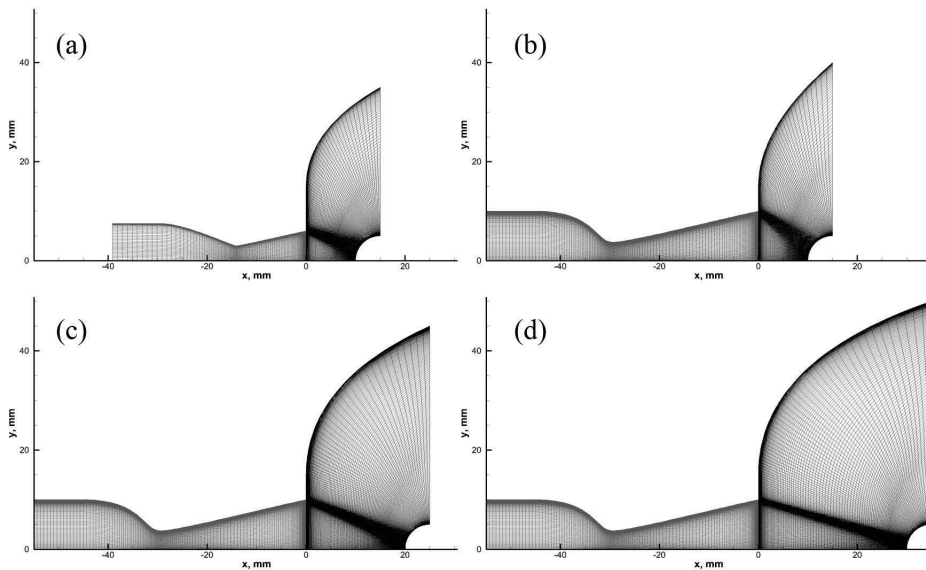


Fig. 45 Grid systems for heat transfer rate calculation.

All the test conditions of pure tungsten used in numerical simulation are listed in Table 12. In the case of repeated tests, averaged flow conditions were used. First, using Eq. (1), enthalpy in the heater chamber was calculated from the nozzle throat area, the pressure of heater chamber, and the air flow rate. As mentioned, flow in the heater chamber can be assumed to be equilibrium state, once enthalpy and pressure were given, other thermodynamic properties including temperature and species mass fraction can be calculated. In this study, Gibb's free energy minimization method [60] was employed to calculate the equilibrium state characteristics from the given

pressure and enthalpy value. The pressure, temperature, velocity and mass fraction of the species are tabulated in Table 13 for each test case.

At the heater chamber before the nozzle, the sectional area increases slightly after the constrictor resulting in cooling of the air, and the temperature before the nozzle is not high enough to cause ionization of air species, existence of the ionized species can be neglected. Actually, from the equilibrium calculation including ionized species, the maximum mass fraction of them was 0.0001 or less. Therefore in the numerical calculation, only 5 species of air were considered for the nozzle inlet condition as tabulated in Table 13.

These thermodynamic values of the heater chamber were used as boundary conditions for the nozzle inlet to conduct numerical simulation of the non-equilibrium flow from the nozzle inlet to the test chamber.

Table 12 Heater chamber conditions and stagnation point pressure

Test cases		D* (mm)	Pch (atm)	Air flow rate (g/s)	Enthalpy (MJ/kg)	Stagnation Pressure (Pa)
Base1	Run1-3	6	5.70	10.09	5.480	121235
Base2	Run4-6	6	6.23	10.15	6.755	132400
Base3	Run7-9	6	5.57	9.00	6.899	118498
VM1	Run1-3, 0-20 s	7.5	3.85	7.57	12.984	62127
	Run1-3, 20-40 s	7.5	4.99	10.21	11.755	80594
	Run1-3, 40-60 s	7.5	5.64	11.74	11.243	91214
VM2	Run4-6, 0-20 s	7.5	3.83	7.80	11.868	61981
	Run4-6, 20-40 s	7.5	5.01	10.37	11.413	81013
	Run4-6, 40-60 s	7.5	5.68	11.91	11.048	91918
VC1	Run1-3, 0-20 s	7.5	3.95	8.27	11.079	64091
	Run1-3, 20-40 s	7.5	3.94	8.26	11.062	63936
	Run1-3, 40-60 s	7.5	4.05	8.29	11.735	65529
VC2	Run4-6, 0-20 s	7.5	5.67	12.14	10.489	91592
	Run4-6, 20-40 s	7.5	5.81	12.14	11.155	93980
	Run4-6, 40-60 s	7.5	5.83	12.15	11.199	94287
Dist1	Run1-2, 10mm	7.5	5.62	11.65	11.385	90835
Dist2	Run3-4, 20mm	7.5	5.62	11.65	11.385	67185
Dist3	Run5-6, 30mm	7.5	5.62	11.65	11.385	52685

Table 13 Heater chamber conditions calculated by equilibrium assumption

Test Case	Pch (Pa)	Tch (K)	Uch (m/s)	Mass fraction				
				O	N	NO	O ₂	N ₂
Base1	574238	3710	114.3	6.629E-2	1.047E-4	7.245E-2	1.280E-1	7.332E-1
Base2	627607	4096	122.8	1.123E-1	4.480E-4	7.541E-2	8.037E-2	7.314E-1
Base3	561115	4119	123.6	1.195E-1	5.158E-4	7.357E-2	7.416E-2	7.322E-1
VM1-1	388326	6022	141.2	2.201E-1	5.829E-2	2.162E-2	1.329E-3	6.987E-1
VM1-2	503318	5787	136.6	2.152E-1	3.440E-2	2.841E-2	2.564E-3	7.194E-1
VM1-3	568884	5663	134.4	2.120E-1	2.585E-2	3.248E-2	3.591E-3	7.261E-1
VM2-1	386313	5765	136.7	2.173E-1	3.778E-2	2.539E-2	2.082E-3	7.175E-1
VM2-2	505337	5692	135.0	2.138E-1	2.894E-2	3.020E-2	3.055E-3	7.240E-1
VM2-3	572919	5603	133.4	2.109E-1	2.305E-2	3.380E-2	4.031E-3	7.283E-1
VC1-1	398419	5549	133.1	2.139E-1	2.499E-2	2.958E-2	3.202E-3	7.283E-1
VC1-2	397411	5543	133.0	2.139E-1	2.475E-2	2.965E-2	3.229E-3	7.285E-1
VC1-3	408504	5741	136.2	2.165E-1	3.521E-2	2.648E-2	2.291E-3	7.195E-1
VC2-1	571913	5415	130.5	2.069E-1	1.597E-2	3.795E-2	5.749E-3	7.334E-1
VC2-2	586031	5641	134.0	2.113E-1	2.446E-2	3.336E-2	3.839E-3	7.270E-1
VC2-3	588049	5655	134.2	2.115E-1	2.507E-2	3.313E-2	3.752E-3	7.265E-1
Dist	566866	5709	135.1	2.128E-1	2.820E-2	3.151E-2	3.289E-3	7.242E-1

Fig. 46 shows calculated density contour and flow streamlines in Base1 condition. As passing through the nozzle, flow expands and accelerate to supersonic speed. Since it was under expanded nozzle, flow kept expanding after the nozzle exit. Fig. 47 shows pressure distribution around the specimen. In front of the specimen, strong bow shock was captured clearly by AUSMPW+ scheme and SAGT. After the shock, pressure rises to about 1.2 atm. In the other cases, numerical simulations were conducted in the same way and stagnation point pressure were calculated. The stagnation point pressure are also listed in Table 12.

Heat transfer rate along the surface line calculated by CFD are shown in Fig. 48 for all cases. In Base cases, the heat transfer rate increases as the enthalpy increases. In VM cases, as the mass flow rate increases, heat transfer rate increases. This shows even though enthalpy is less, heat flux can be greater due to stagnation point pressure. In VC cases, heat flux was decided by enthalpy but the difference was very small. In Dist cases, as the distance from the nozzle exit to the specimen increases, both the stagnation point pressure and the heat transfer rate decrease. This is a characteristic of the facility, that has conical nozzle and under expanded flow condition.

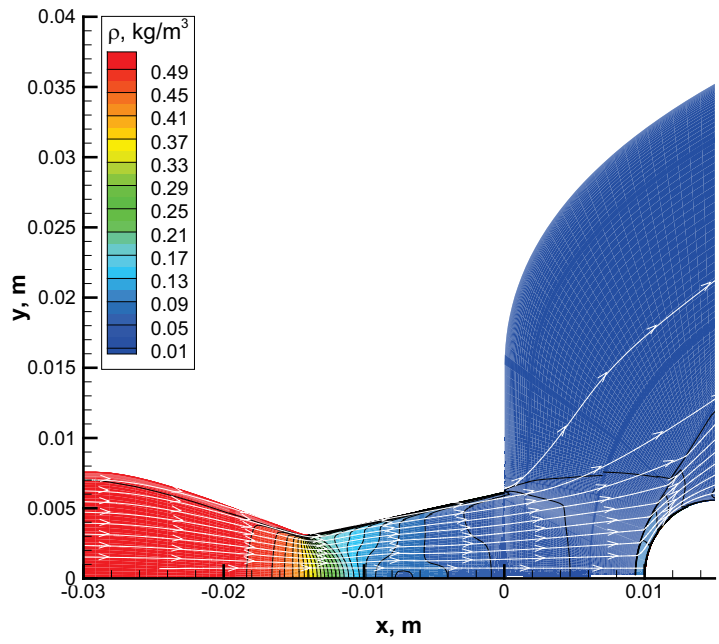


Fig. 46 Density distribution and streamlines (Base1).

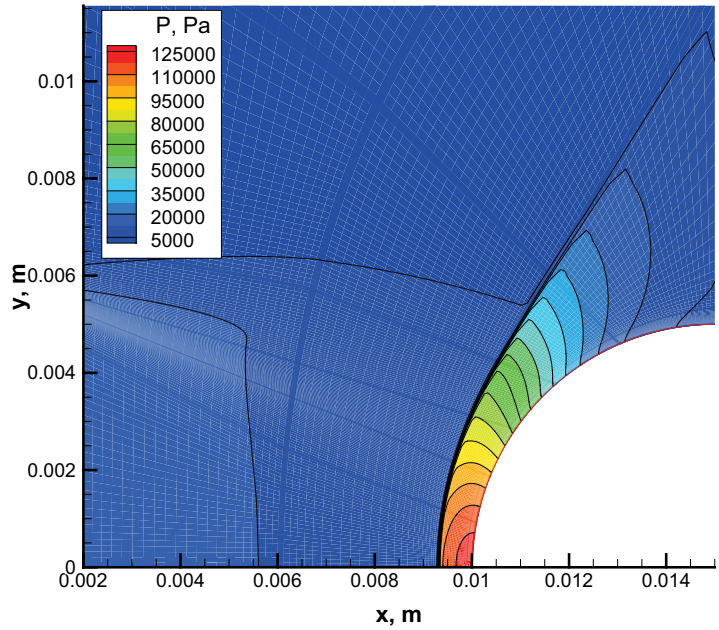


Fig. 47 Pressure distributions around the specimen (Base1).

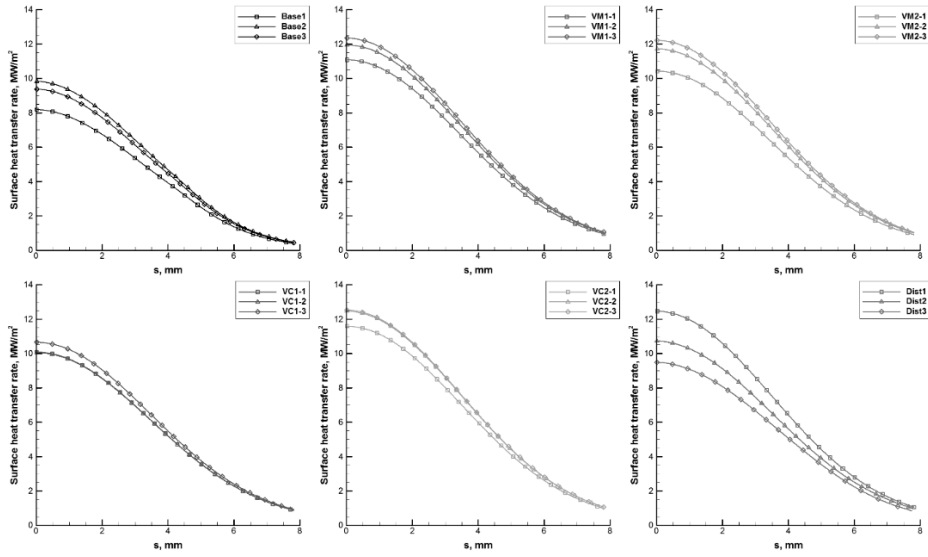


Fig. 48 Heat transfer rate at the surface in different test cases.

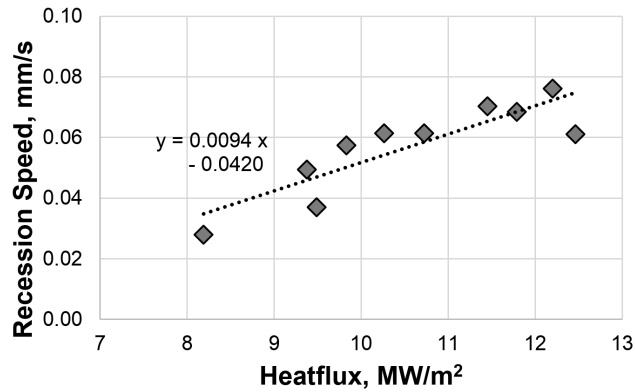


Fig. 49 Recession rate versus stagnation point heatflux.

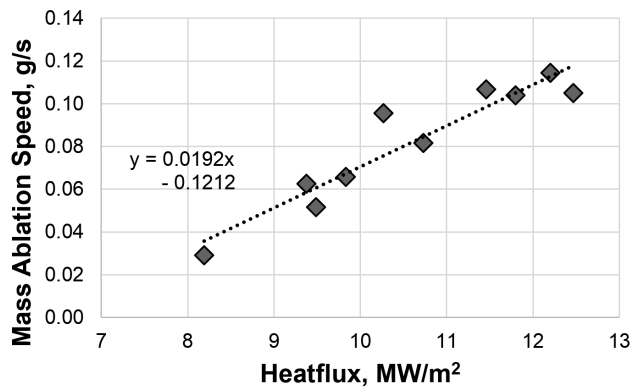


Fig. 50 Mass ablation rate versus stagnation point heatflux.

From those heat transfer rate values calculated in each flow condition, the ablation rates versus stagnation point heat flux at initial were presented. They are shown in Fig. 49 and Fig. 50. In the figures, recession rates in depth and mass are simply calculated by dividing the change in length and mass after the test respectively by total test time. In VM and VC cases, an averaged value of the heat fluxes were used. As a result, it was appeared that ablation rates in both recession and mass loss have tendency to be proportional to the initial stagnation point heat fluxes. From these results, a simple linear equation expresses the relations between ablation rate and heat flux was deduced as follows.

$$R_{length} [mm / s] = 0.0094 \times q_w [MW / m^2] - 0.042 \quad (112)$$

$$R_{mass} [g / s] = 0.0192 \times q_w [MW / m^2] - 0.1212 \quad (113)$$

These results can be used to predict ablation rate of tungsten roughly, when the primary ablation mechanism is thermochemical ablation, particularly oxidation. However, those results have many limitations and uncertainties to be used in other applications with different conditions or specimens shapes. In order to develop an ablation model which can be used more generally, more detailed model which can predict an ablation rate at the chemical reaction level was needed.

4.3 Parametric study on ablation test conditions

In order to develop a thermochemical ablation model for tungsten, more detailed flow conditions and parameters at the surface of tungsten were needed. Various numerical simulations were performed to calculate those flow parameters including heat transfer rate, which could not be measured during the experiment, and calibrate the experimental results for the development of the ablation model. It was conducted in Base cases—Run3, Run6, and Run9 for a test time frame of 60 seconds. Through the simulation, various flow properties including density, temperature, pressure, and mass fractions of each species at each point in the grid were obtained. In addition, the simulation helped to verify the overall aspect of the flow which could further act as groundwork for future experiments. Table 14 lists the calculated flow conditions at the center of the nozzle exit in each test case.

Table 14 Flow conditions at the center of nozzle exit

	Run3	Run6	Run9	
ρ , kg/m ³	0.04594	0.04344	0.03814	
u, m/s	2255	2428	2437	
p, Pa	23449	25285	22173	
h, MJ/kg	5.55	6.91	7.04	
T, K	1667	1826	1813	
T _v , K	2307	2478	2548	
Mach	2.73	2.74	2.75	
	N	1.587E-7	9.464E-7	1.041E-6
Mass fraction	O	0.069166	0.117968	0.125263
	NO	0.074769	0.069649	0.067667
	N ₂	0.732121	0.734566	0.735484
	O ₂	0.123943	0.077815	0.071584

Different between equilibrium and non-equilibrium calculations

As mentioned before, the simulation helped to calculate the mass fraction of the gas species, which could not be measured during the test. Fig. 51 shows mass fraction of O atoms along the centerline near the specimen. Solid lines represent the mass fraction calculated using the non-equilibrium solver, while the dash-dotted lines

represent the mass fraction calculated using the equilibrium assumption with temperature and pressure of each point. In the case of equilibrium flow, it is not necessary to calculate the mass fraction of the chemical species independently to know their composition because it can be obtained from the temperature and pressure. However, when the flow shows strong non-equilibrium characteristics, as in this study, the mass fraction should be measured separately in the experiment or calculated using the non-equilibrium flow solver, which includes chemical species continuity equations and a vibrational energy equation, in computational fluid dynamics (CFD) analysis.

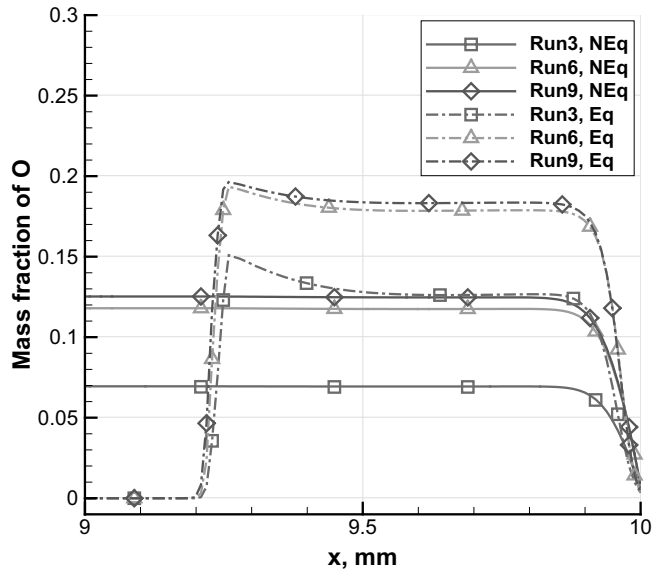


Fig. 51 Mass fraction of O along the centerline.

Since the flow in the test chamber was non-equilibrium—close to frozen—the mass fraction remained almost constant along the centerline unlike that calculated from the equilibrium assumption. The mass fraction of the non-equilibrium calculation changed slightly, passing the shock, and then decreased significantly near the wall because of catalytic recombination. As shown in the figure, there is a large difference in the slope of the mass fraction of O atoms at the surface between equilibrium and non-equilibrium calculation. This affected the rates of diffusion and

recombination, and consequently, the heat transfer rate significantly.

Heat transfer rate on fully catalytic and non-catalytic wall

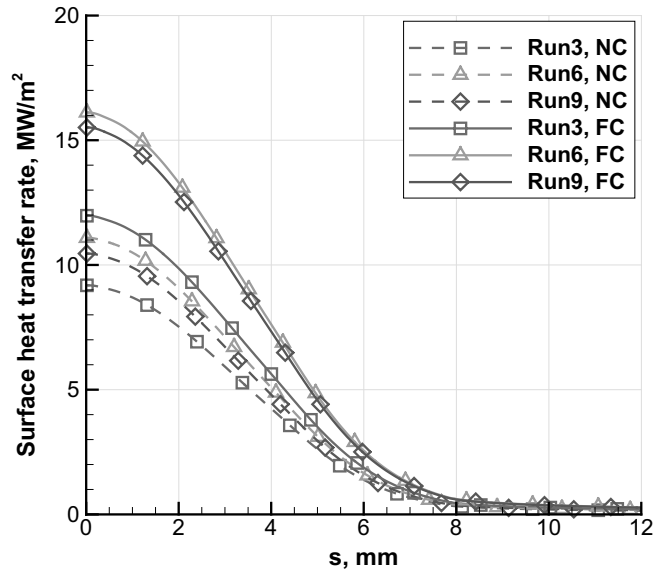


Fig. 52 Heat transfer rate along surface line on 300 K fully and non-catalytic surface.

Fig. 52 shows the calculated heat transfer rate with different wall conditions along the surface line from the stagnation point when the surface temperature was 300 K. As expected, the surface heat transfer rate was the highest at the stagnation point, and it gradually decreases along surface line to the side surface. The rate was at its highest in the Run6 flow conditions, and at its lowest in Run3. The heat transfer rate was much higher at the fully catalytic surface than at the non-catalytic surface due to exothermic catalytic recombination.

Heat transfer rate against different surface temperature

The heat transfer rate into the stagnation point versus surface temperature was investigated and displayed in Fig. 53. Without oxidation, only fully catalytic and non-catalytic conditions were considered with surface temperatures ranging from 300 K to 3,500 K with 500 K intervals. The solid lines represent heat transfer rate at

the fully catalytic surface and the dashed lines represent the value at the non-catalytic surface respectively. As shown in Fig. 53, the heat transfer rate is greater in the fully catalytic condition than in the non-catalytic condition, and it decreases linearly as the surface temperature increases. At 300 K, the heat transfer rate was the highest in Run6 and lowest in Run3.

In the figure, dash-dotted lines with small filled symbols show the expected heat transfer rate on the actual surface considering the oxidation of tungsten. At low surface temperatures, the catalytic condition of the tungsten surface was close to the non-catalytic condition, and at high surface temperatures, it was expected to show higher heat flux than the fully catalytic wall due to oxidation reaction.

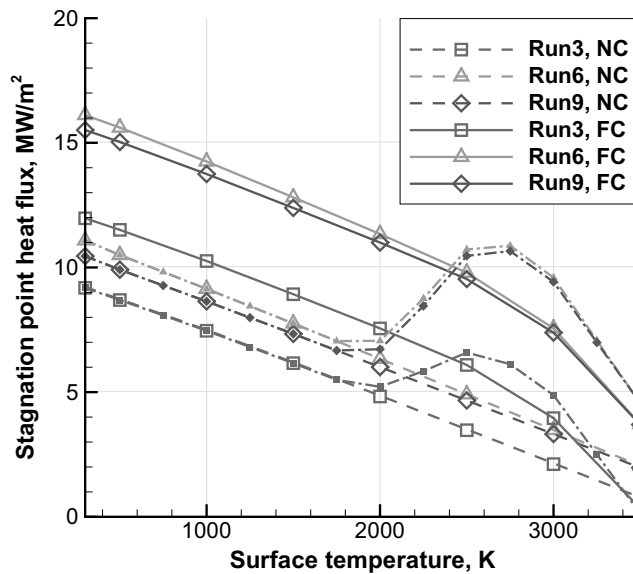


Fig. 53 Stagnation point heat transfer rate versus surface temperature.

Effect of oxidation coefficient

The effect of oxidation coefficient, η_O^{oxi} , on the heat transfer rate was investigated, and is presented in Fig. 54. Surface temperature was set to 2,500 K that seems high enough for oxidation to occur. Since the sum of η_O^{oxi} and η_O^{cat} could not exceed unity, surface catalycity was set to 0.2, and oxidation coefficient was varied from 0 to 0.8. Since oxidation is an exothermic reaction, the surface heat transfer rate increased rapidly at the beginning with the increase in oxidation coefficient. Later, it saturated at an oxidation coefficient of approximately 0.2.

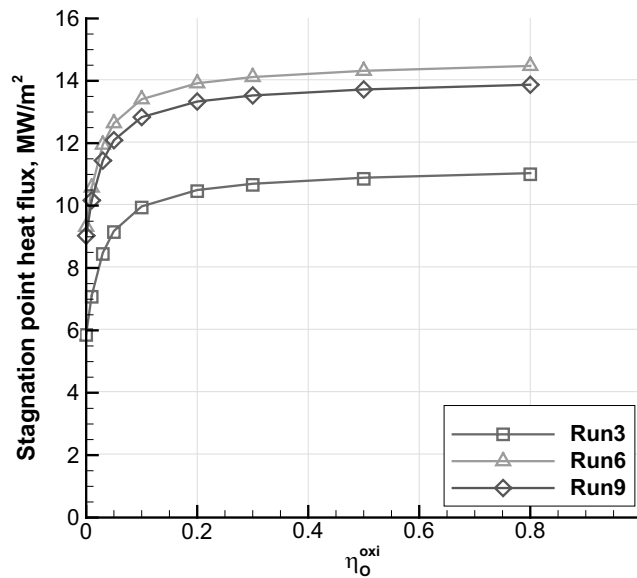


Fig. 54 Stagnation point heat transfer rate versus oxidation coefficient.

Shape change of the specimen

The ablation test confirmed that ablation caused the specimen shape to change with time. In order to evaluate the effects of the change in shape of the specimen, the analyses were performed on various grid systems of different specimen shapes with different parameters shown in Fig. 55.

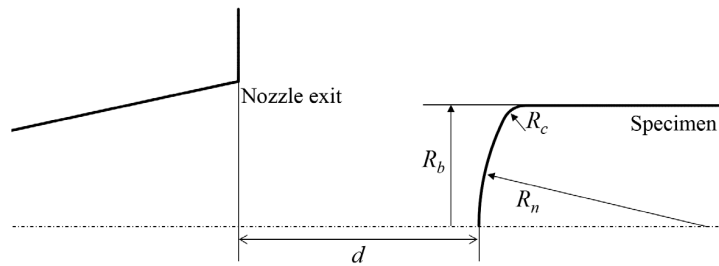


Fig. 55 Shape parameters for different grid systems.

First, considering the recession of the stagnation point from the initial position due to ablation, the rate of heat transfer was calculated. The surface temperature was fixed at 2,500 K, and both η_O^{oxi} and η_O^{cat} were set to 0.2. Considering the maximum recession in the experiment (3.53 mm at 60 seconds in Run6), the rates of heat transfer was calculated from $d=10$ to $d=14$ mm, which were identical to the range between initial point and recession of 4 mm.

In Fig. 56, it can be observed that the heat transfer rate decreases almost linearly as the specimen distance increases. When the specimen was moved 4 mm from the initial position, the heat flux decreased about 11% from the initial value.

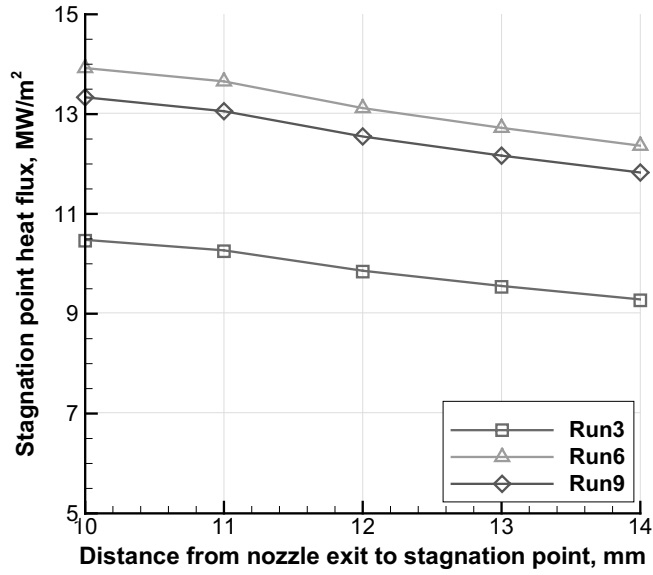


Fig. 56 Stagnation point heat transfer rate versus specimen distance.

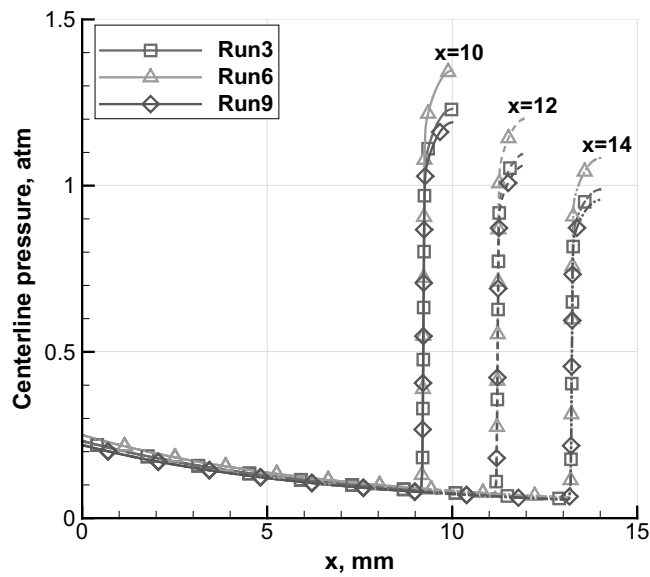


Fig. 57 Pressure distribution along the center line for different distances.

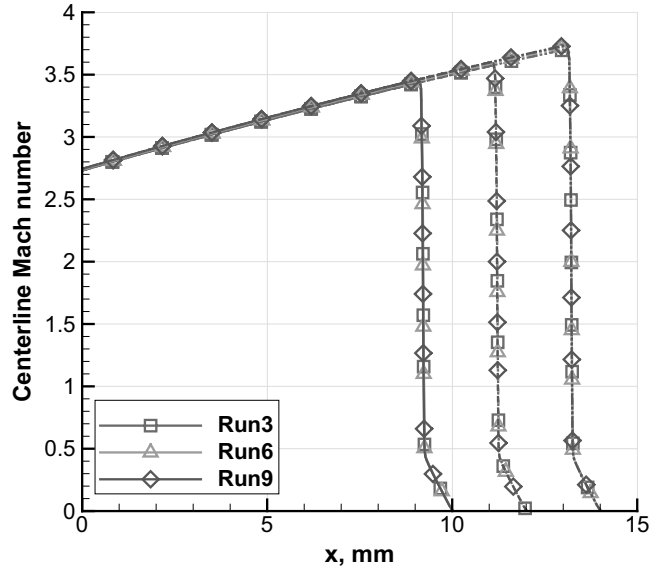


Fig. 58 Mach number distribution along the center line for different distances.

Fig. 57 and Fig. 58 show a plot of the pressure and Mach number distribution along the center line outside the nozzle exhaust region for different distances of the specimen. In the same flow conditions, the stagnation pressure was found to have decreased with the increase in distance between the specimen and the nozzle exhaust. Since the flow kept expanding towards the specimen from the nozzle exit, the Mach number was found to have increased as the distance increased. It is known that a larger Mach number causes greater shock intensity, and consequently, a greater pressure loss through the shock. A change in the rate of heat transfer due to a change in distance is supposed to be a characteristic of the facility, such as nozzle shape (conical) and under-expanded flow at nozzle exit due to low pressure at the test section. In addition, for this experimental facility, calculating in advance the heat transfer rate for different specimen position may enable the application of the desired experimental condition to future ablation tests.

The effect of nose radius was also investigated. As mentioned in the previous section, nose radius, R_n , was varied from 5 to 25 mm while corner radius, R_c , and cylinder radius, R_b , were fixed to 1 and 5 mm respectively. In Fig. 59, a plot of stagnation point heat flux versus nose radius is shown. It can be observed that the

heat flux decreases gradually as the nose radius increases. According to Fay and Riddell [15], the stagnation point heat transfer rate on a hemisphere is known to be inversely proportional to the square root of its radius.

$$q_w \propto \frac{1}{\sqrt{R}} \quad (114)$$

The specimen used in this study, however, unlike the perfect sphere, has a uniform body radius. Therefore the effective radius from [27] was adopted. Fig. 60 shows a plot of stagnation point heat flux versus the inverse of square root of effective radius deduced from the values of R_n , R_b and R_c , which shows a linear increase as expected.

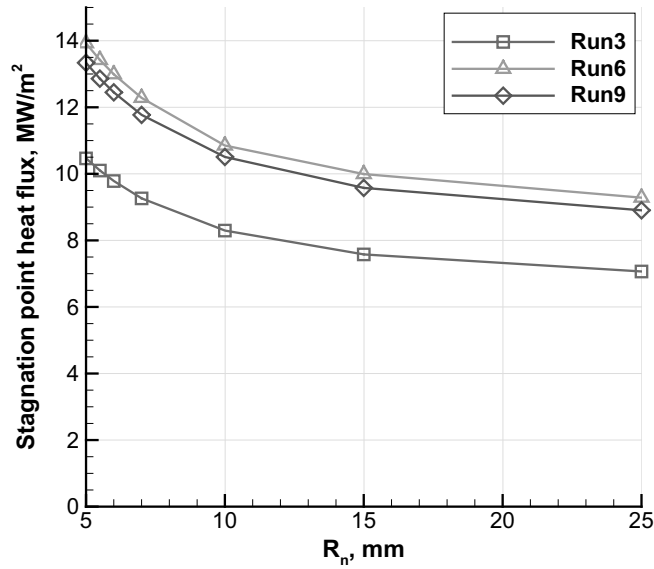


Fig. 59 Stagnation point heat flux versus nose radius of the specimen.

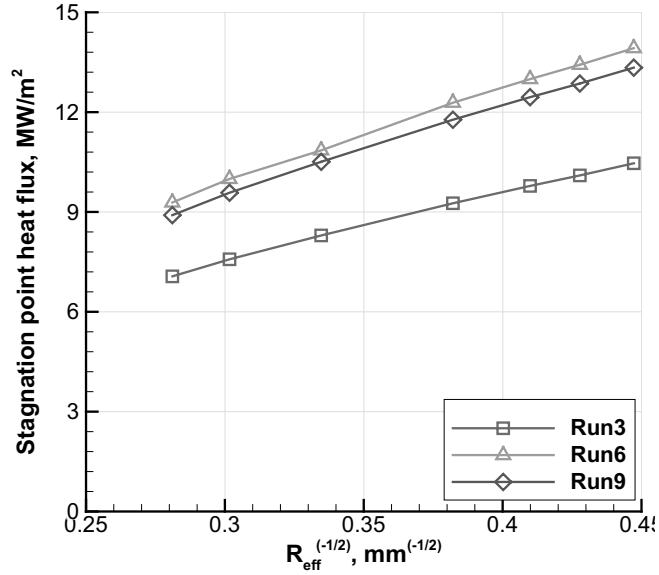


Fig. 60 Stagnation point heat flux versus inverse root of nose radius.

In the experiment, the shape of the specimen at the final state with an ablation time frame of 60 seconds has a nose radius of 10–13 mm. In Fig. 60, the heat transfer rate sees a 21% reduction from that in the initial state for R_n of 10 mm, and a 28% reduction for R_n of 15 mm. The reduction in heat transfer rate due to increase in nose radius was approximately twice the reduction obtained due to increase in distance. This result was considerably greater than expected; thus, the effect of change in nose shape on the rate of heat transfer or recession should be considered when conducting ablation test for a specimen with blunt nose.

In addition, a numerical simulation was conducted for the final state of the experiment and compared with the results from the initial state. As mentioned earlier, grid systems were generated based on the high-speed camera image taken at the final state in the test Run3, Run6, and Run9. They are shown in Fig. 61. When η_O^{oxi} equals 0.2, the stagnation point heat transfer rate decreased by 29%, 35%, and 34% from the initial state in Run3, Run6 and Run9, respectively. Since the ablation rate was at its highest in Run6, the Run6 specimen, of all the test specimens, has the biggest nose radius and the longest distance from the nozzle exit, which is why the reduction

of heat flux at final state compared to the initial state is the largest in Run6 and the least at Run3. This result, confirms that the reduction of stagnation point heat flux due to the change in shape of the specimen by ablation was approximately 30% and above. This figure is too large to be ignored when we try to make ablation model from the experiment. In addition, similar to the heat transfer rate, ablation rate decreased with the change in shape of the specimen. In the experiment, the decrement in recession rate in Base cases shown in Fig. 15 is also thought to be due to shape deformation of the specimen.

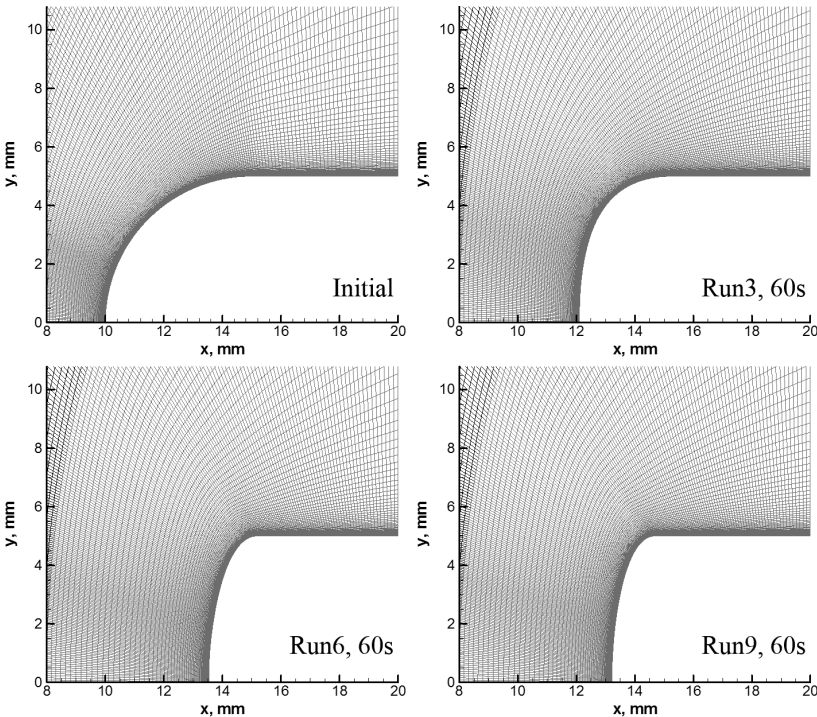


Fig. 61 Grids near the specimen with different shape.

4.4 Simulation of Tungsten Ablation

With the data of recession rate deduced above, a numerical model for chemical ablation of tungsten was developed. To do this, a numerical simulation of the entire ablation test of 60 seconds window was conducted by an ablation analysis program that combined a non-equilibrium flow solver and a thermal response analysis solver with ablation model of tungsten. Whole computational domain are shown in Fig. 62. Both flow and solid grids are shown in the figure. The flow grid starts from the nozzle inlet after a heater chamber and ends at the middle of the specimen. It consists of a nozzle section and a test chamber section, which have 180×60 and 180×220 cells respectively.

Fig. 63 shows a solid grid system. The solid grid also consists of two parts, inner and outer grids. They consist of 90×180 and 220×60 cells respectively. Only the outer grid is deformed by ablation while the inner grid is preserved.

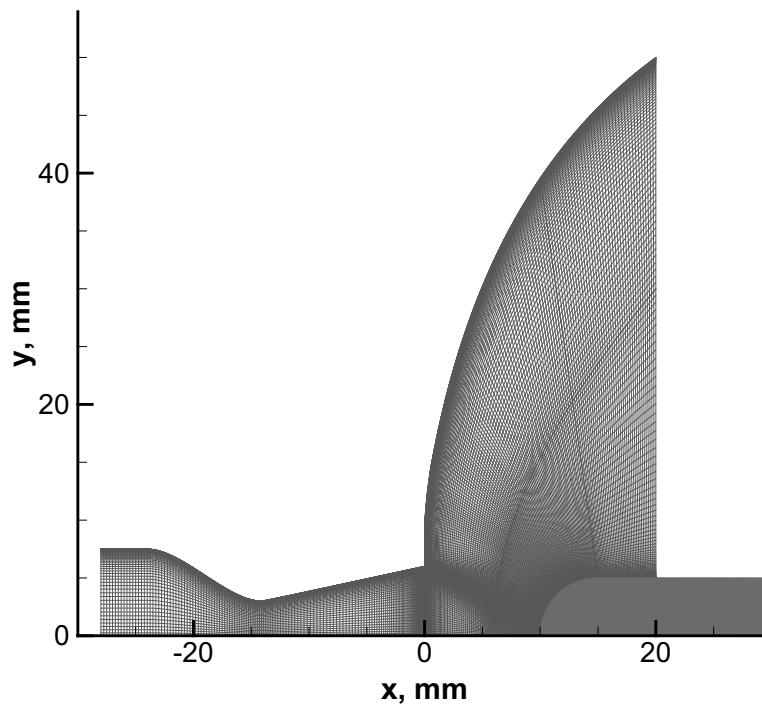


Fig. 62 Grid systems for ablation calculation.

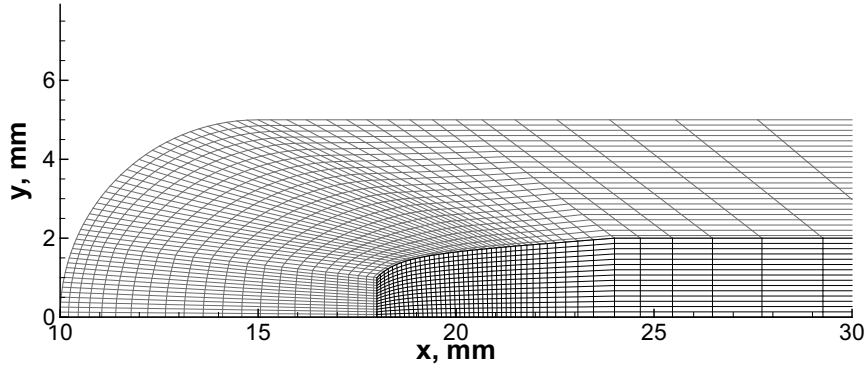


Fig. 63 Grid system of solid specimen (skip=4).

On the above grid system, as numerical results when $t = 60$ s, pressure contour and Mach number contour on whole computational domain are shown in Fig. 64 and Fig. 65 respectively. As explained earlier, since the flow condition was under-expanded at the nozzle exit, the flow keep expanded and accelerated to the specimen. A strong bow shock is observed before the specimen. By ablation, the specimen is located farther than its original position, $x = 10$ mm, and its shape was deformed. These can be seen in Fig. 67 more clearly. In Fig. 67, pressure contours around the specimen are drawn with 10 seconds interval from initial to $t = 60$ s in all the simulation cases. The stagnation point pressures were high in the order of Base2, Base1, and Base3. After about 20 seconds, the shape of specimen starts to be deformed. As the time increases, the stagnation point recesses and stagnation pressure also decreases. The ablation amount were high in order of Base2, Base3, and Base1 as observed in the experiment.

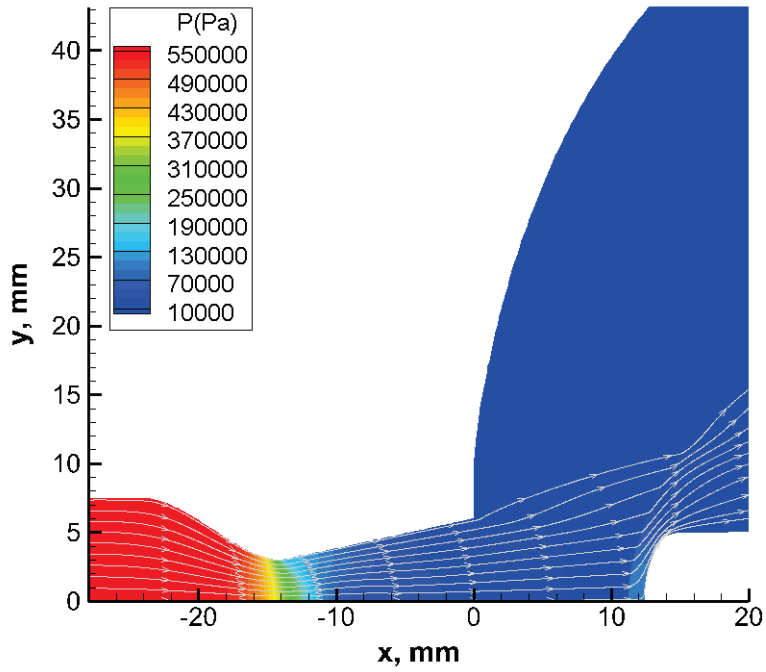


Fig. 64 Pressure contour on whole region (Base1).

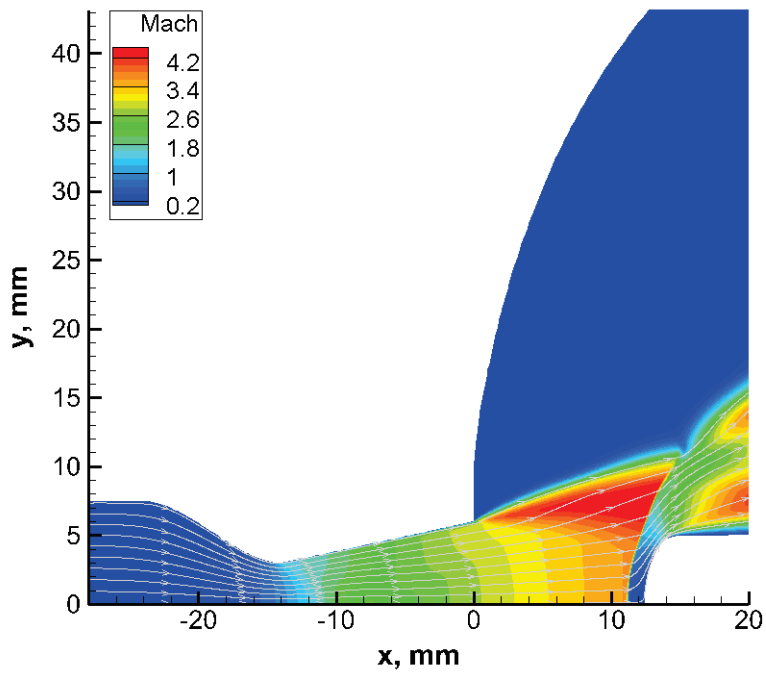


Fig. 65 Mach number contour on whole region (Base1).

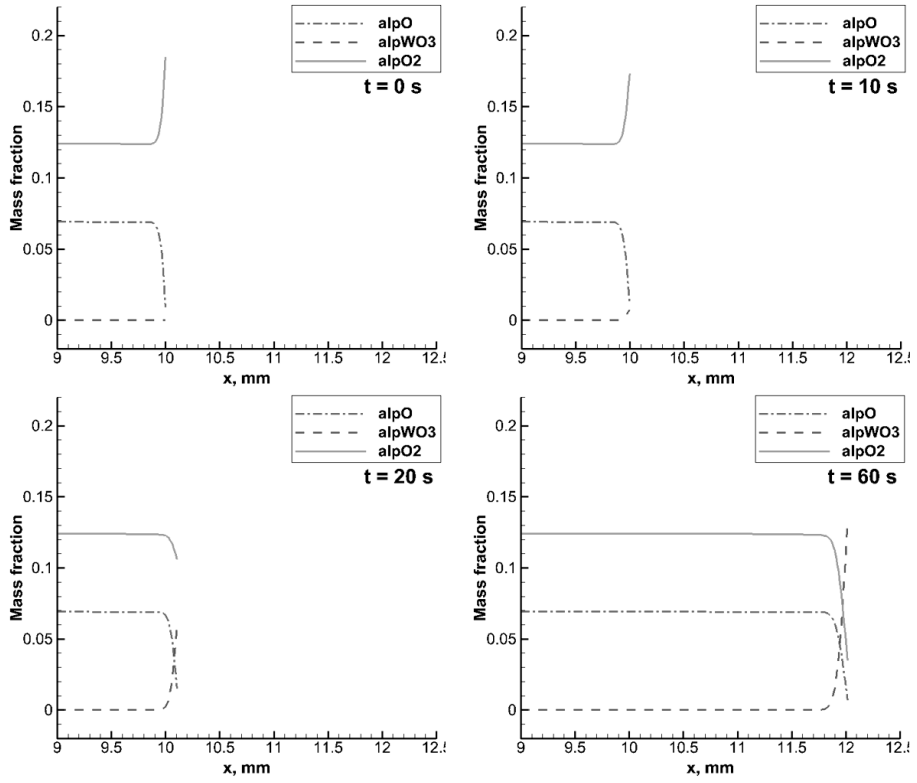


Fig. 66 Centerline mass fraction at different time steps (Base1).

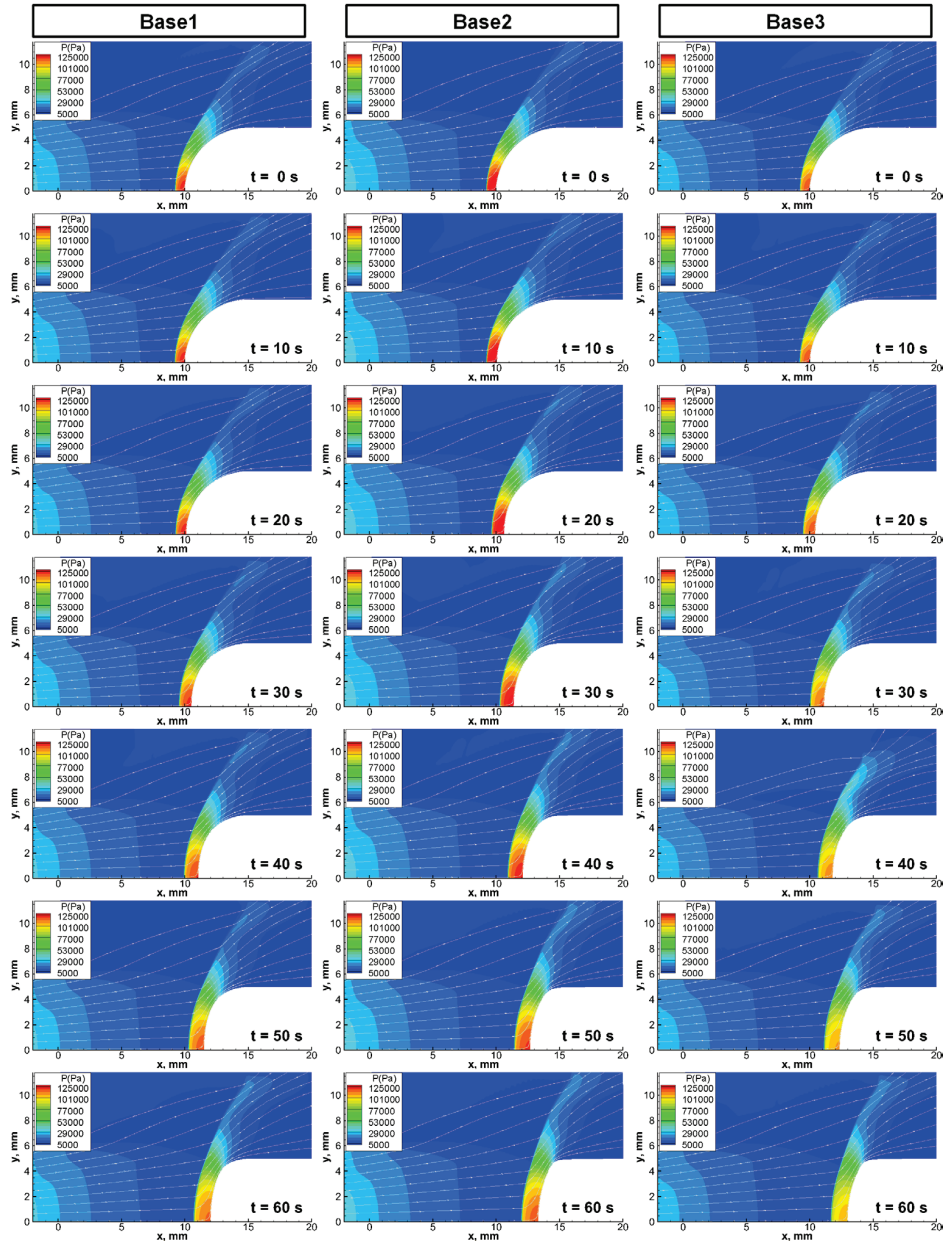


Fig. 67 Pressure contours around specimen over time.

Fig. 66 shows mass fractions of O, O₂, and WO₃ along the centerline at different time steps. At initial, incident O atoms generate O₂ molecules at the surface by the surface catalytic recombination. Thus vicinity of the wall, the mass fraction of O₂ increases while that of O decreases. WO₃ is not produced yet. At 10 seconds, as the

surface temperature increases, WO_3 starts to be formed gradually. As the recombination is suppressed by the temperature increase, O_2 mass fraction at the surface is slightly smaller than initial state. At 20 seconds, oxidation of tungsten occurs actively, thus mass fraction WO_3 increases noticeably. In addition, O_2 molecules starts to be dissociated, not to be recombined. Since those O atoms are used to generate WO_3 , mass fraction of O is still low at the surface. These tendency can be observed much stronger at 60 seconds. Most of O and O_2 molecules are consumed to generated WO_3 and other tungsten oxides at the surface.

Fig. 68 shows analysis results of tungsten internal temperature along time with 10 seconds intervals in all three flow conditions. It can be noticeable that the temperature inside the specimen increases rapidly at initial, then saturated after about 30 seconds. The change of specimen shape also can be observed clearly in the figure. The amount of ablation was large in the order of Base2, Base3, and Base1, which was in the same order of temperature increase. In all the cases, ablation occurs the most around the stagnation point, then the nose radius of the specimen increases as the ablation processed.

In Fig. 69, a plot of variation of stagnation point temperature and heat flux over time is shown. In this figure, temperature (dashed lines) increases rapidly at initial and then saturates with time. Meanwhile, heat transfer rate decreases at initial as surface temperature increases, then rises temporarily after the local minimum point then decreases again gradually. At the local minimum point, the surface reaction and ablation begin to occur actively, thus the heat transfer rate also increases temporarily. In the latter stage in which the surface temperature is saturated, the linear decrement in heat transfer rate is due to change in shape of the specimen.

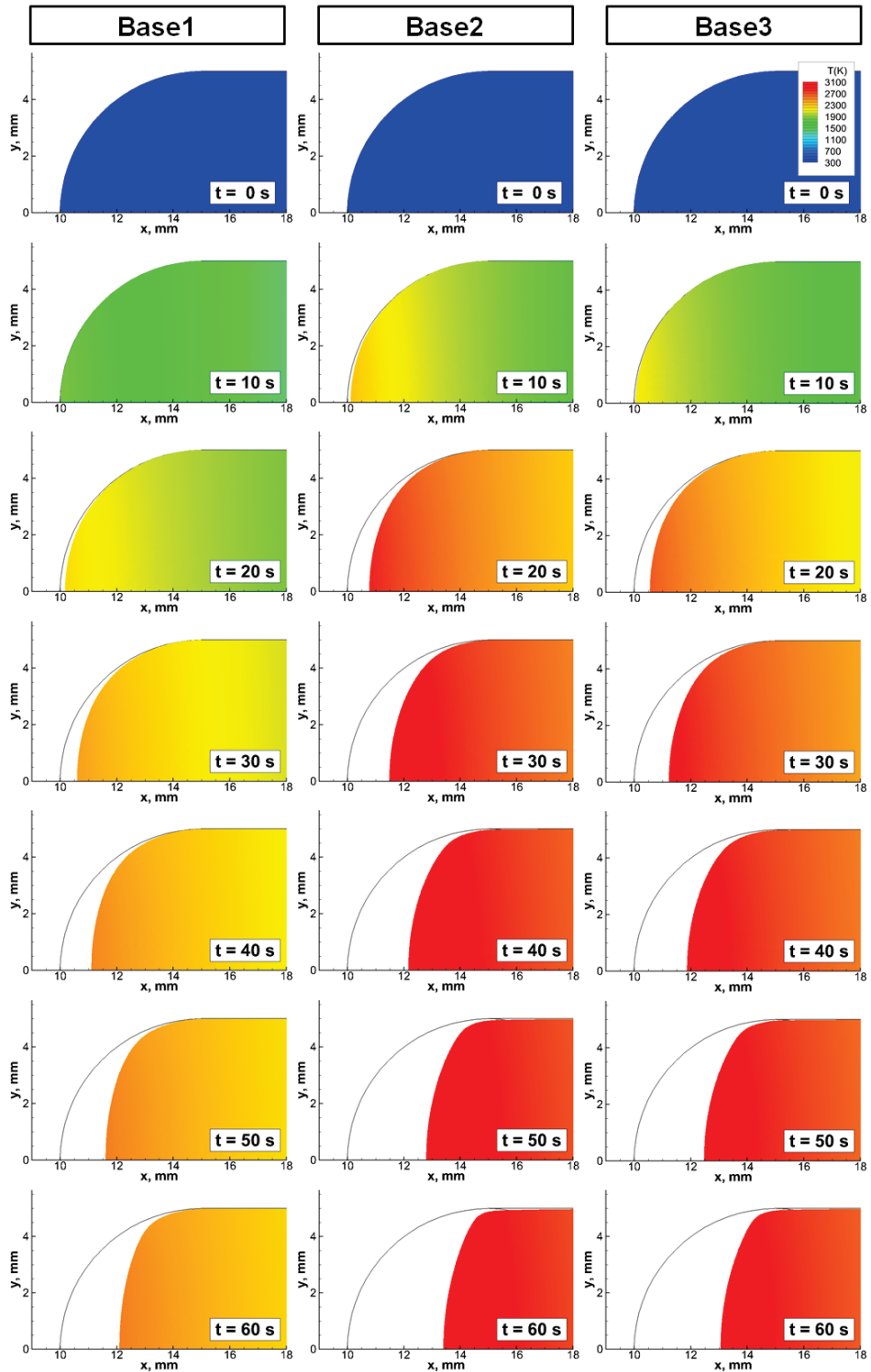


Fig. 68 Calculated specimen shapes and internal temperatures over time.

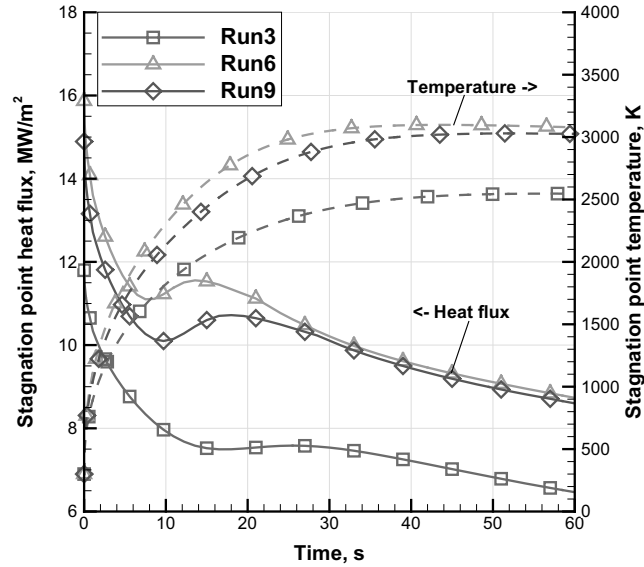


Fig. 69 Calculated stagnation point heat flux and temperature versus time.

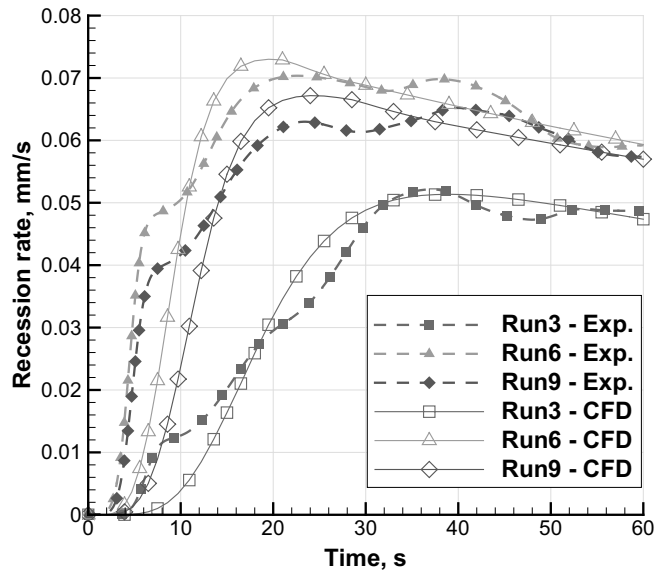


Fig. 70 Calculated mass flow rate at stagnation point versus time.

Finally, the recession rate of numerical simulation was compared to the experimental result. In Fig. 70, the solid lines represent the calculated stagnation point recession rate due to ablation against time. The experimental result is also displayed together with dashed lines. In each flow condition, the calculated recession rate increases over time, after which it decreases almost linearly. In the ablation

model used in this study, oxidation rate increases with the surface temperature. As a result, the recession rate also increases at the initial stage with the surface temperature. On the other hand, the decrement of recession rate is, as mentioned before, due to the shape change by the ablation. Unless the ablation causes a change in shape, the recession rate will saturate and remain constant due to limits imposed by diffusion rate. Compared to the experimental result, this effect of shape change was more pronounced in the simulation results. Additionally, the recession rate calculated in the numerical simulation starts to increase slower than the experiment at the initial stage, and this is so because in the model, the ablation of tungsten oxides by melt run-off was not considered. Considering those uncertainties, the ablation model developed in this study is regarded to describe chemical ablation of tungsten pretty well.

Lastly, not only the stagnation point recession, but the change in shape of the whole specimen was compared. In Fig. 71–Fig. 73, calculated shape change and pressure contours are drawn in multi-colored line with the high speed camera images at $t = 30$ s and $t = 60$ s respectively. It can be observed that calculated surface lines are well matched with the surface lines in the image taken by high speed camera during the ablation test. This result proves that the ablation model developed in this study can be used to predict the shape change of tungsten by ablation, so that it can be used for applications such as design of tungsten products considering high temperature ablation.

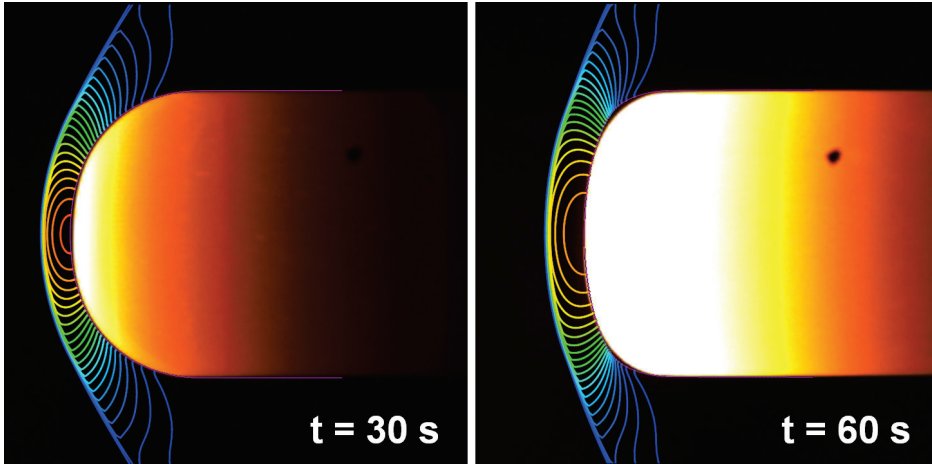


Fig. 71 Calculated pressure contours and high speed camera images (Base1).

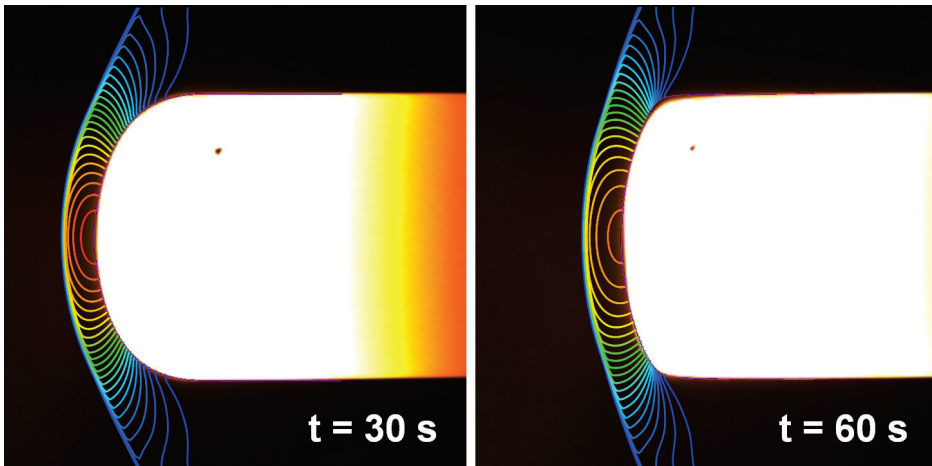


Fig. 72 Calculated pressure contours and high speed camera images (Base2).

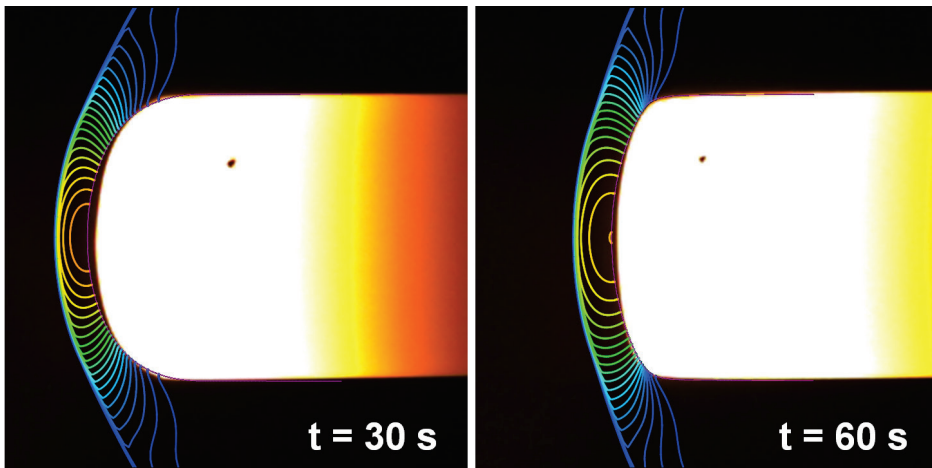


Fig. 73 Calculated pressure contours and high speed camera images (Base3).

Chapter 5. Conclusion

To develop a thermochemical ablation model for tungsten and corresponding analysis program, ablation tests on pure tungsten and tungsten composites were conducted in the 150-kW arc heater facility. After the test, a non-equilibrium flow simulation on the test condition was conducted to calculate the parameters that could not be measured in the experiments, such as surface heat transfer rate and species mass fraction. Through this study, the following results were obtained.

1. The relation between the total ablation rate of pure tungsten and the initial heat flux was deduced, which was linearly proportional. Changes in mass and length of the specimen were measured after the tests under 10 different flow conditions, and for those test conditions, the initial heat transfer rates at surface were calculated through non-equilibrium flow calculation. At this stage, the ablation rate was calculated simply dividing the total ablation amount by the test time.
2. The ablation-suppressing effect of HfC and ZrC reinforcements were confirmed by ablation test on W-HfC and W-ZrC composites. Tungsten composite specimens containing 10, 20, and 30vol% of each reinforcement were tested, and their effects were remarkable. The ablation rate decreased by 60% with the 30vol% of HfC, and it decreased by 28% with the same volume percent of ZrC. In addition, after those experiments, microstructure analysis of specimen were conducted.
3. The flows generated from the 150-kW arc heater was highly non-equilibrium, especially from the nozzle throat to the specimen. It was confirmed that the mass fraction of oxygen found by non-equilibrium calculation shows considerable difference from that found by equilibrium calculation. Especially in a small-sized plasma test like the one used in the present study, non-equilibrium effects should be considered carefully to predict surface oxidation rate accurately.
4. The surface heat transfer rate and ablation rate decreased by the shape change of

specimen during the ablation test. When the actual shape changes of the ablated specimen in the tests of Base cases that ran for 60 seconds were considered, the heat transfer rate decreased by 29%, 35%, and 34% in the flow conditions of Run3, Run6, and Run9 respectively, due to the shape changes by ablation. In this study, this effect of shape change of specimen was divided into two aspects: distance and nose radius.

5. When the distance increased from 10 mm to 14 mm at the conical nozzle, the flow expanded greatly, the Mach number before the shock increased from 3.45 to 3.72, and the heat transfer rate at the stagnation point decreased by approximately 11%. Therefore, in a similar facility, in which there is a conical nozzle and the flow keeps expanding after the nozzle, the effect of increasing distance on the heat transfer rate or ablation rate during the test should be checked.
6. Meanwhile, the reduction in the heat transfer rate due to the increased nose radius was calculated to be around 21% and 28% when the nose radius were increased from 5 mm to 10 mm and from 5 mm to 15 mm, respectively. This reduction in the heat transfer rate and ablation rate due to the change in shape during the ablation test can be easily overlooked, therefore it should be considered carefully, especially when the ablation amount is large.
7. Stagnation point recession data over time were deduced from the high-speed camera images using a Matlab code. From the observations stated above, it was expected that the time-dependent changes in ablation rate due to the shape change would also be existed in the present experiment and actually, the decrease of recession rate was observed from the stagnation point recession data. These data were used to derive a function describing thermochemical ablation, which is mainly oxidation, of tungsten at the surface.
8. Finally, an ablation model and an ablation analysis program which consist of a non-equilibrium flow solver coupled with a solid thermal response solver was developed. This program successfully described ablation test results on pure

tungsten specimens with hemispherical nose, not only for 1-dimensional stagnation point recession rate, but also the shape changes of the specimen. Through additional validations against wider range of ablation tests, this program is expected to be used in various high enthalpy tungsten application including ablation phenomena, especially designing and predicting the ablation amount of the parts made of tungsten or tungsten composites.

Additionally, when an ablation test is conducted in order to develop an ablation model for thermal protection of high Mach-regime aerospace vehicles, more detailed and reliable data, including heat transfer rate, can be obtained by performing both numerical analysis and practical experiment. As shown in this study, heat transfer rate changes over time due to various reasons; thus all the effects should be considered to build a more accurate ablation model and ablative materials. In this process, numerical simulation can be an efficient tool that can compensate the experimental data by calculating otherwise unmeasurable parameters.

In the future, additional ablation test on various tungsten composites made of different reinforcement materials, contents, and manufacturing method, can be conducted in order to increase the reliability of the developed ablation model. In the additional ablation test, thermocouples will be installed inside or back of the specimen to measure the temperature data over time. This internal temperature data can be utilized to validate thermal response calculation results of solid solver, and can improve the reliability of the developed ablation analysis program.

Appendix

A. Coefficients for non-equilibrium reaction rates.

In this section, non-equilibrium reaction models for dissociated and ionized air of following 11 species were described: N, O, NO, N₂, O₂, N⁺, O⁺, NO⁺, N₂⁺, O₂⁺, e.

Park's Model 1993 [37]

In the Park's model, the reaction coefficients for forward reactions are given in the following form.

$$k_f(T_x) = CT_x^n \exp(-E / kT_x) \quad [cm^3 / (mol \cdot s)]$$

There are several documents of Park [37], [61], [39] which describe the reaction coefficients for ionized air. The numbers for the reaction coefficients of these documents has slight difference one another. In this dissertation, the values of the reference [37] were tabulated.

Reaction	<i>M</i>	<i>T_x</i>	<i>C</i>	<i>n</i>	<i>E/k</i>
Dissociation (1-31)					
<i>N₂ + M ↔ N + N + M</i> (1-11)	<i>N₂, O₂, NO</i>	<i>T_a**</i>	7.00E+21	-1.60	113,200
	<i>N, O</i>		3.00E+22	-1.60	113,200
	<i>N₂⁺, O₂⁺, NO⁺</i>		7.00E+21	-1.60	113,200
	<i>N⁺, O⁺</i>		3.00E+22	-1.60	113,200
	<i>e</i>		1.20E+25*	-1.60	113,200
<i>O₂ + M ↔ O + O + M</i> (12-21)	<i>N₂, O₂, NO</i>	<i>T_a</i>	2.00E+21	-1.50	59,500
	<i>N, O</i>		1.00E+22	-1.50	59,500
	<i>N₂⁺, O₂⁺, NO⁺</i>		2.00E+21	-1.50	59,500
	<i>N⁺, O⁺</i>		1.00E+22	-1.50	59,500
<i>NO + M ↔ N + O + M</i> (22-31)	<i>N₂, O₂</i>	<i>T_a</i>	5.00E+15	0.00	75,500
	<i>N, O, NO</i>		1.10E+17	0.00	75,500
	<i>N₂⁺, O₂⁺, NO⁺</i>		5.00E+15	0.00	75,500
	<i>N⁺, O⁺</i>		1.10E+17	0.00	75,500
Electron-impact ionization (32-33)					
<i>N + e ↔ N⁺ + e + e</i>	(32)	<i>T_e</i>	2.50E+34	-3.82	168,600
<i>O + e ↔ O⁺ + e + e</i>	(33)		3.90E+33	-3.78	158,500

NO exchange (34-35)					
$N_2 + O \leftrightarrow NO + N$	(34)	T	6.40E+17	-1.00	38,400
$NO + O \leftrightarrow O_2 + N$	(35)		8.40E+12	0.00	19,450
Associative ionization [†] (36-38)					
$N + O \leftrightarrow NO^+ + e$	(36)	T	8.80E+08	1.00	31,900
$N + N \leftrightarrow N_2^+ + e$	(37)		4.40E+07	1.50	67,500
$O + O \leftrightarrow O_2^+ + e$	(38)		7.10E+02	2.70	80,600
Charge exchange (39-49)					
$O^+ + N_2 \leftrightarrow N_2^+ + O$	(39)	T	9.10E+11	0.36	22,800
$O^+ + NO \leftrightarrow N^+ + O_2$	(40)		1.40E+05	1.90	26,600 [‡]
$NO^+ + O_2 \leftrightarrow O_2^+ + NO$	(41)		2.40E+13	0.41	32,600
$NO^+ + N \leftrightarrow N_2^+ + O$	(42)		7.20E+13	0.00	35,500
$NO^+ + O \leftrightarrow N^+ + O_2$	(43)		1.00E+12	0.50	77,200
$O_2^+ + N \leftrightarrow N^+ + O_2$	(44)		8.70E+13	0.14	28,600
$O_2^+ + N_2 \leftrightarrow N_2^+ + O_2$	(45)		9.90E+12	0.00	40,700
$NO^+ + N \leftrightarrow O^+ + N_2$	(46)		3.40E+13	-1.08	12,800
$NO^+ + O \leftrightarrow O_2^+ + N$	(47)		7.20E+12	0.29	48,600
$O_2^+ + O \leftrightarrow O^+ + O_2$	(48)		4.00E+12	-0.09	18,000
$N^+ + N_2 \leftrightarrow N_2^+ + N$ [§]	(49)		1.00E+12	0.50	12,200

* This value is different to the value of [61]

† These values are from the table 2 in reference [37], which are different in Eq. (5)-(7)

‡ This value is different to the value of [61], need to be checked.

§ This reaction was not used in this dissertation, because the coefficients for equilibrium constant curve fit could not be found in [61].

** $T_a = (T \times T_v)^{0.5}$

Reaction coefficients for backward reactions are calculated from equilibrium constants as follows:

$$k_b(T_y) = \frac{k_f(T_y)}{K_{eq}(T_y)}$$

Here, equilibrium constant, K_{eq} , can be calculated from the following curve fit with five coefficients of Park.

$$K_{eq}(T) = \exp \left[A_1 \left(\frac{T}{10000} \right) + A_2 + A_3 \ln \left(\frac{10000}{T} \right) + A_4 \left(\frac{10000}{T} \right) + A_5 \left(\frac{10000}{T} \right)^2 \right]$$

The coefficients for equilibrium constants are tabulated for different mixture

number density, N. In the program, interpolated values were used.

Reaction	N(1/cm ³)	A1	A2	A3	A4	A5
Dissociation						
$N_2 + M \leftrightarrow N + N + M$ (1-11)	1.0E+14	3.4907	0.83133	4.0978	-12.728	0.07487
	1.0E+15	2.0723	1.3897	2.0617	-11.828	0.015105
	1.0E+16	1.6060	1.5732	1.3923	-11.533	-0.00454
	1.0E+17	1.5351	1.6061	1.2993	-11.494	-0.00698
	1.0E+18	1.4766	1.6291	1.2153	-11.457	-0.00944
	1.0E+19	1.4766	1.6291	1.2153	-11.457	-0.00944
$O_2 + M \leftrightarrow O + O + M$ (12-21)	1.0E+14	1.8103	1.9607	3.5716	-7.3623	0.083861
	1.0E+15	0.91354	2.316	2.2885	-6.7969	0.046338
	1.0E+16	0.64183	2.4253	1.9026	-6.6277	0.035151
	1.0E+17	0.55388	2.46	1.7763	-6.572	0.031445
	1.0E+18	0.52455	2.4715	1.7342	-6.5534	0.030209
	1.0E+19	0.50989	2.4773	1.7132	-6.5441	0.029591
$NO + M \leftrightarrow N + O + M$ (22)	1.0E+14	2.1649	0.078577	2.8508	-8.5422	0.053043
	1.0E+15	1.0072	0.53545	1.1911	-7.8098	0.004394
	1.0E+16	0.63817	0.68189	0.66336	-7.5773	-0.011025
	1.0E+17	0.55889	0.71558	0.55396	-7.5304	-0.014089
	1.0E+18	0.515	0.73286	0.49096	-7.5025	-0.015938
	1.0E+19	0.50765	0.73575	0.48042	-7.4979	-0.016247
Electron-impact ionization						
$N + e \leftrightarrow N^+ + e + e$ (32)	1.0E+14	-1.9094	-3.0267	-3.6935	-16.044	-0.050183
	1.0E+15	-1.2002	-3.3059	-2.6755	-16.494	-0.020301
	1.0E+16	-0.96709	-3.3976	-2.3408	-16.642	-0.010477
	1.0E+17	-0.93184	-3.414	-2.2946	-16.661	-0.009269
	1.0E+18	-0.9026	-3.4255	-2.2526	-16.679	-0.008037
	1.0E+19	-0.9026	-3.4255	-2.2526	-16.679	-0.008037
$O + e \leftrightarrow O^+ + e + e$ (33)	1.0E+14	0.08045	-5.7393	-1.4195	-15.844	-0.001087
	1.0E+15	0.52883	-5.917	-0.77795	-16.127	0.017675
	1.0E+16	0.66478	-5.9716	-0.58486	-16.212	0.023273
	1.0E+17	0.70879	-5.989	-0.52169	-16.24	0.025127
	1.0E+18	0.72341	-5.9947	-0.5007	-16.249	0.025743
	1.0E+19	0.73078	-5.9976	-0.49012	-16.254	0.026054
NO exchange						
$N_2 + O \leftrightarrow NO + N$ (34)	1.0E+14	1.3261	0.75268	1.2474	-4.1857	0.02184
	1.0E+15	1.0653	0.85417	0.87093	-4.0188	0.010721
	1.0E+16	0.96794	0.89131	0.7291	-3.9555	0.006488
	1.0E+17	0.97646	0.89043	0.74572	-3.9642	0.007123
	1.0E+18	0.96188	0.89617	0.72479	-3.955	0.006509
	1.0E+19	0.96921	0.89329	0.73531	-3.9596	0.006818
$NO + O \leftrightarrow O_2 + N$ (35)	1.0E+14	0.35438	-1.8821	-0.72111	-1.1797	-0.030831
	1.0E+15	0.093613	-1.7806	-1.0975	-1.0128	-0.041949
	1.0E+16	-0.003732	-1.7434	-1.2394	-0.94952	-0.046182
	1.0E+17	0.004815	-1.7443	-1.2227	-0.95824	-0.045545
	1.0E+18	-0.009758	-1.7386	-1.2436	-0.949	-0.046159
	1.0E+19	-0.002428	-1.7415	-1.2331	-0.95365	-0.04585
Associative ionization						
$N + O \leftrightarrow NO^+ + e$ (36)	1.0E+14	-2.1852	-6.6709	-4.2968	-2.2175	-0.050748
	1.0E+15	-1.0276	-7.1278	-2.637	-2.95	-0.0021
	1.0E+16	-0.65871	-7.2742	-2.1096	-3.1823	0.01331
	1.0E+17	-0.57924	-7.3079	-1.9999	-3.2294	0.016382
	1.0E+18	-0.53538	-7.3252	-1.937	-3.2572	0.01823
	1.0E+19	-0.52801	-7.3281	-1.9264	-3.2618	0.01854

	-4.3785	-4.2726	-7.8709	-4.4628	-0.12402	-4.3785
	-2.9601	-4.831	-5.8348	-5.3621	-0.064252	-2.9601
$N + N \leftrightarrow N_2^+ + e$	-2.4938	-5.0145	-5.1654	-5.6577	-0.044602	-2.4938
(37)	-2.4229	-5.0474	-5.0724	-5.6961	-0.042167	-2.4229
	-2.3644	-5.0704	-4.9885	-5.7332	-0.039703	-2.3644
	-2.3644	-5.0704	-4.9885	-5.7332	-0.039703	-2.3644
	-0.11682	-7.6883	-2.2498	-7.7905	-0.011079	-0.11682
	0.77986	-8.0436	-0.96678	-8.3559	0.02644	0.77986
$O + O \leftrightarrow O_2^+ + e$	1.0516	-8.153	-0.58082	-8.5251	0.037629	1.0516
(38)	1.1395	-8.1876	-0.45461	-8.5808	0.041333	1.1395
	1.1689	-8.1991	-0.41245	-8.5995	0.042571	1.1689
	1.1835	-8.2049	-0.39146	-8.6087	0.043187	1.1835
	-0.96795	2.2979	-2.3531	-1.3463	-0.048042	-0.96795
	-1.4164	2.4756	-2.9947	-1.0636	-0.066805	-1.4164
$O^+ + N_2 \leftrightarrow N_2^+ + O$	-1.5522	2.5303	-3.1876	-0.97903	-0.072396	-1.5522
(39)	-1.5962	2.5476	-3.2507	-0.95116	-0.074249	-1.5962
	-1.6108	2.5533	-3.2718	-0.94186	-0.074867	-1.6108
	-1.6181	2.5562	-3.2823	-0.93721	-0.075176	-1.6181
	-1.6355	0.83058	-2.9952	-1.3794	-0.079927	-1.6355
	-1.6355	0.83058	-2.9952	-1.3794	-0.079927	-1.6355
$O^+ + NO \leftrightarrow N^+ + O_2$	-1.6355	0.83058	-2.9952	-1.3794	-0.079927	-1.6355
(40)	-1.6355	0.83058	-2.9952	-1.3794	-0.079927	-1.6355
	-1.6355	0.83058	-2.9952	-1.3794	-0.079927	-1.6355
	-1.6355	0.83058	-2.9952	-1.3794	-0.079927	-1.6355
	1.7139	0.86469	2.7679	-4.3932	0.070493	1.7139
	1.7139	0.86469	2.7679	-4.3932	0.070493	1.7139
$NO^+ + O_2 \leftrightarrow O_2^+ + NO$	1.7139	0.86469	2.7679	-4.3932	0.070493	1.7139
(41)	1.7139	0.86469	2.7679	-4.3932	0.070493	1.7139
	1.7139	0.86469	2.7679	-4.3932	0.070493	1.7139
	1.7139	0.86469	2.7679	-4.3932	0.070493	1.7139
	-2.1934	2.3983	-3.5743	-2.2452	-0.073271	-2.1934
	-1.9325	2.2968	-3.1978	-2.4121	-0.062149	-1.9325
$NO^+ + N \leftrightarrow N_2^+ + O$	-1.8352	2.2597	-3.056	-2.4754	-0.057919	-1.8352
(42)	-1.8438	2.2606	-3.0726	-2.4667	-0.058554	-1.8438
	-1.8292	2.2548	-3.0517	-2.4759	-0.05794	-1.8292
	-1.8365	2.2577	-3.0622	-2.4713	-0.058248	-1.8365
	-1.5349	1.6836	-2.969	-6.464	-0.083316	-1.5349
	-1.0864	1.5059	-2.3273	-6.7468	-0.064551	-1.0864
$NO^+ + O \leftrightarrow N^+ + O_2$	-0.95072	1.4513	-2.1346	-6.8313	-0.058964	-0.95072
(43)	-0.90672	1.434	-2.0714	-6.8592	-0.05711	-0.90672
	-0.89206	1.4282	-2.0504	-6.8685	-0.056493	-0.89206
	-0.88472	1.4254	-2.0398	-6.8731	-0.056184	-0.88472
	-3.603	2.701	-5.0155	-0.89125	-0.12297	-3.603
	-2.8938	2.4218	-3.9975	-1.3409	-0.093088	-2.8938
$O_2^+ + N \leftrightarrow N^+ + O_2$	-2.6607	2.33	-3.6628	-1.4887	-0.083264	-2.6607
(44)	-2.6252	2.3136	-3.6163	-1.5079	-0.082048	-2.6252
	-2.596	2.3021	-3.5744	-1.5264	-0.080816	-2.596
	-2.596	2.3021	-3.5744	-1.5264	-0.080816	-2.596
	-2.5811	2.2863	-5.0946	-2.0378	-0.12192	-2.5811
	-2.5811	2.2863	-5.0946	-2.0378	-0.12192	-2.5811
$O_2^+ + N_2 \leftrightarrow N_2^+ + O_2$	-2.5811	2.2863	-5.0946	-2.0378	-0.12192	-2.5811
(45)	-2.5811	2.2863	-5.0946	-2.0378	-0.12192	-2.5811
	-2.5811	2.2863	-5.0946	-2.0378	-0.12192	-2.5811
	-2.5811	2.2863	-5.0946	-2.0378	-0.12192	-2.5811
	-1.2255	0.10039	-1.2212	-0.89883	-0.025232	-1.2255

	-0.51629	-0.17877	-0.20321	-1.3485	0.004649	-0.51629
	-0.28311	-0.27056	0.13152	-1.4963	0.014474	-0.28311
	-0.24765	-0.28699	0.17802	-1.5155	0.015692	-0.24765
$NO^+ + N \leftrightarrow O^+ + N_2$	-0.21842	-0.29849	0.21998	-1.534	0.016923	-0.21842
(46)	-0.21842	-0.29849	0.21998	-1.534	0.016923	-0.21842
	2.0681	-1.0173	2.0466	-5.5728	0.039655	2.0681
	1.8073	-0.91584	1.6701	-5.4058	0.028533	1.8073
$NO^+ + O \leftrightarrow O_2^+ + N$	1.71	-0.87869	1.5282	-5.3426	0.024301	1.71
(47)	1.7185	-0.87958	1.5449	-5.3513	0.024936	1.7185
	1.7039	-0.87383	1.5239	-5.342	0.024321	1.7039
	1.7112	-0.87672	1.5345	-5.3467	0.024631	1.7112
	-1.61320	-0.011626	-2.7416	-0.69145	-0.07388	-1.61320
	-1.16480	-0.18931	-2.1000	-0.9742	-0.055116	-1.16480
$O_2^+ + O \leftrightarrow O^+ + O_2$	-1.02900	-0.24394	-1.9072	-1.0587	-0.049527	-1.02900
(48)	-0.98502	-0.26125	-1.8440	-1.0866	-0.047674	-0.98502
	-0.97037	-0.26702	-1.8230	-1.0959	-0.047056	-0.97037
	-0.96302	-0.26991	-1.8125	-1.1005	-0.046747	-0.96302
$N^+ + N_2 \leftrightarrow N_2^+ + N$						
(49)				To be updated		

Gupta's model [43]

In Gupta's model, reaction coefficients for both forward and backward reactions are given in the same way as follows:

$$k_f = CT_x^n \exp(-E/kT_x) \quad [cm^3 / (mol \cdot s)]$$

$$k_b = CT_x^n \exp(-E/kT_x) \quad [cm^3 / (mol \cdot s) \text{ or } cm^6 / (mol^2 \cdot s)]$$

No.	Reaction	Forward			Backward		
		C	n	E/k	C	n	E/k
1	$O_2 + O \leftrightarrow 3O$	3.61E18	-1.0	5.94E04	3.01E15	-0.5	0
2	$O_2 + N \leftrightarrow 2O + N$	3.61E18	-1.0	5.94E04	3.01E15	-0.5	0
3	$2O_2 \leftrightarrow 2O + O_2$	3.61E18	-1.0	5.94E04	3.01E15	-0.5	0
4	$O_2 + N_2 \leftrightarrow 2O + N_2$	3.61E18	-1.0	5.94E04	3.01E15	-0.5	0
5	$O_2 + NO \leftrightarrow 2O + NO$	3.61E18	-1.0	5.94E04	3.01E15	-0.5	0
6	$N_2 + O \leftrightarrow 2N + O$	1.92E17	-0.5	1.13E05	1.09E16	-0.5	0
7	$N_2 + O_2 \leftrightarrow 2N + O_2$	1.92E17	-0.5	1.13E05	1.09E16	-0.5	0
8	$2N_2 \leftrightarrow 2N + N_2$	1.92E17	-0.5	1.13E05	1.09E16	-0.5	0
9	$N_2 + NO \leftrightarrow 2N + NO$	1.92E17	-0.5	1.13E05	1.09E16	-0.5	0
10	$N_2 + N \leftrightarrow 3N$	4.15E22	-1.5	1.13E05	2.32E21	-1.5	0
11	$NO + O \leftrightarrow N + 2O$	3.97E20	-1.5	7.56E04	1.01E20	-1.5	0
12	$NO + N \leftrightarrow 2N + O$	3.97E20	-1.5	7.56E04	1.01E20	-1.5	0
13	$NO + O_2 \leftrightarrow N + O + O_2$	3.97E20	-1.5	7.56E04	1.01E20	-1.5	0
14	$NO + N_2 \leftrightarrow N + O + N_2$	3.97E20	-1.5	7.56E04	1.01E20	-1.5	0
15	$2NO \leftrightarrow N + O + NO$	3.97E20	-1.5	7.56E04	1.01E20	-1.5	0
16	$NO + O \leftrightarrow O_2 + N$	3.18E09	1.0	1.97E04	9.63E11	0.5	3600
17	$N_2 + O \leftrightarrow NO + N$	6.75E13	0.0	3.75E04	1.50E13	0.0	0
18	$N + O \leftrightarrow NO^+ + e^-$	9.03E09	0.5	3.24E04	1.80E19	-1.0	0
19	$O + e^- \leftrightarrow O^+ + 2e^-$	3.60E31	-2.91	1.58E05	2.20E40	-4.5	0
20	$N + e^- \leftrightarrow N^+ + 2e^-$	1.10E32	-3.14	1.69E05	2.20E40	-4.5	0
21	$2O \leftrightarrow O_2^+ + e^-$	1.60E17	-0.98	8.08E04	8.02E21	-1.5	0
22	$O + O_2^+ \leftrightarrow O_2 + O^+$	2.92E18	-1.11	2.80E04	7.80E11	0.5	0
23	$N_2 + N^+ \leftrightarrow N + N_2^+$	2.02E11	0.81	1.30E04	7.80E11	0.5	0
24	$2N \leftrightarrow N_2^+ + e^-$	1.40E13	0.0	6.78E04	1.50E22	-1.5	0
25	$O_2 + N_2 \leftrightarrow NO + NO^+ + e^-$	1.38E20	-1.84	1.41E05	1.00E24	-2.5	0
26	$NO + O_2 \leftrightarrow NO^+ + O_2 + e^-$	2.20E15	-0.35	1.08E05	2.20E26	-2.5	0
27	$NO + N_2 \leftrightarrow NO^+ + N_2 + e^-$	2.20E15	-0.35	1.08E05	2.20E26	-2.5	0

28	$O + NO^+ \leftrightarrow NO + O^+$	3.63E15	-0.6	5.08E04	1.50E13	0.0	0
29	$N_2 + O^+ \leftrightarrow O + N_2^+$	3.40E19	-2.00	2.30E04	2.48E19	-2.2	0
30	$N + NO^+ \leftrightarrow NO + N^+$	1.00E19	-0.93	6.10E04	4.80E14	0.0	0
31	$O_2 + NO^+ \leftrightarrow NO + O_2^+$	1.80E15	0.17	3.30E04	1.80E13	0.5	0
32	$O + NO^+ \leftrightarrow O_2 + N^+$	1.34E13	0.31	7.73E04	1.00E14	0.0	0

B. Milikan and White coefficients for vibrational relaxation

Relaxation time by Milikan and White can be calculated as follows

$$\tau_{is} = \frac{101325}{P_i} \exp \left[A_{is} \left(T^{-1/3} - B_{is} \right) - 18.42 \right]$$

Coefficient A and B are tabulated below.

Vibrator(i)	Partner(s)	A _{is}	B _{is}	Vibrator(i)	Partner(s)	A _{is}	B _{is}
N ₂	N ₂	221.53	0.029	N ₂ ⁺	N ₂	221.53	0.029
N ₂	O ₂	228.76	0.0295	N ₂ ⁺	O ₂	228.76	0.0295
N ₂	N	180.88	0.0262	N ₂ ⁺	N	180.88	0.0262
N ₂	O	72.4	0.015	N ₂ ⁺	O	188.89	0.0268
N ₂	NO	225.3	0.0293	N ₂ ⁺	NO	225.3	0.0293
N ₂	N ₂ ⁺	221.53	0.029	N ₂ ⁺	N ₂ ⁺	221.53	0.029
N ₂	O ₂ ⁺	228.76	0.0295	N ₂ ⁺	O ₂ ⁺	228.75	0.0295
N ₂	N ⁺	180.88	0.0262	N ₂ ⁺	N ⁺	180.88	0.0262
N ₂	O ⁺	188.89	0.0268	N ₂ ⁺	O ⁺	188.88	0.0268
N ₂	NO ⁺	225.3	0.0293	N ₂ ⁺	NO ⁺	225.3	0.0293
N ₂	e	1.39	0.0023	N ₂ ⁺	e	1.39	0.0023
O ₂	N ₂	131.32	0.0295	O ₂ ⁺	N ₂	131.32	0.0295
O ₂	O ₂	135.91	0.03	O ₂ ⁺	O ₂	135.91	0.03
O ₂	N	72.4	0.015	O ₂ ⁺	N	106.06	0.0265
O ₂	O	47.7	0.059	O ₂ ⁺	O	110.97	0.0271
O ₂	NO	133.71	0.0298	O ₂ ⁺	NO	133.71	0.0298
O ₂	N ₂ ⁺	131.32	0.0295	O ₂ ⁺	N ₂ ⁺	131.32	0.0295
O ₂	O ₂ ⁺	135.91	0.03	O ₂ ⁺	O ₂ ⁺	135.9	0.03
O ₂	N ⁺	106.06	0.0265	O ₂ ⁺	N ⁺	106.05	0.0265
O ₂	O ⁺	110.97	0.0271	O ₂ ⁺	O ⁺	110.97	0.0271
O ₂	NO ⁺	133.71	0.0298	O ₂ ⁺	NO ⁺	133.7	0.0298
O ₂	e	0.8	0.0023	O ₂ ⁺	e	0.8	0.0023
NO	N ₂	49.5	0.042	NO ⁺	N ₂	175.67	0.0293
NO	O ₂	49.5	0.042	NO ⁺	O ₂	181.61	0.0298
NO	N	49.5	0.042	NO ⁺	N	142.62	0.0264
NO	O	49.5	0.042	NO ⁺	O	149.09	0.027
NO	NO	49.5	0.042	NO ⁺	NO	178.76	0.0295
NO	N ₂ ⁺	175.67	0.0293	NO ⁺	N ₂ ⁺	175.67	0.0293
NO	O ₂ ⁺	181.6	0.0298	NO ⁺	O ₂ ⁺	181.6	0.0298
NO	N ⁺	142.62	0.0264	NO ⁺	N ⁺	142.62	0.0264
NO	O ⁺	149.08	0.027	NO ⁺	O ⁺	149.08	0.027
NO	NO ⁺	178.76	0.0295	NO ⁺	NO ⁺	178.76	0.0295
NO	e	1.08	0.0023	NO ⁺	e	1.08	0.0023

C. Transport properties for each species

In the Blottner's work [46], the viscosity is calculated with three different coefficients for each species as follows:

$$\mu_i = 0.1 \times T^{(A_i \log(T) + B_i)} \exp(C_i) \quad [N \cdot s / m^2]$$

The coefficients in the equation are listed in the following table.

Species	A_i	B_i	C_i
N	1.16E-02	6.03E-01	-1.24E+01
O	2.03E-02	4.29E-01	-1.16E+01
NO	4.36E-02	-3.36E-02	-9.58E+00
N ₂	2.68E-02	3.18E-01	-1.13E+01
O ₂	4.49E-02	-8.26E-02	-9.20E+00
N ₂ ⁺	2.68E-02	3.18E-01	-1.13E+01
O ₂ ⁺	4.49E-02	-8.26E-02	-9.20E+00
NO ⁺	3.02E-01	-3.50E+00	-3.74E+00
N ⁺	1.16E-02	6.03E-01	-1.24E+01
O ⁺	2.03E-02	4.29E-01	-1.16E+01
e ⁻	0.00E+00	0.00E+00	-1.20E+01
C	-1.00E-04	7.93E-01	-1.34E+01
C ₂	-3.10E-03	6.92E-01	-1.26E+01
C ₃	-1.47E-02	8.81E-01	-1.35E+01
CO	-1.95E-02	1.01E+00	-1.40E+01
CN	2.50E-03	6.81E-01	-1.25E+01
CO ₂	-1.95E-02	1.05E+00	-1.43E+01
CO ⁺	-1.95E-02	1.01E+00	-1.40E+01
C ⁺	-8.33E-03	7.70E-01	-1.27E+01

When the Blottner's curve fit was used, thermal and vibrational conductivities are calculated from Eucken's formula[62] generally.

$$k_s = \mu_s \left(\frac{5}{2} c_{v,tr} + c_{v,rot} \right) = \begin{cases} \frac{15}{4} \mu_s R & (\text{Monomolecular molecule}) \\ \frac{19}{4} \mu_s R & (\text{Binary molecule}) \end{cases}$$

$$k_{v,s} = \mu_s c_{v,vib,s} = \mu_s \frac{\theta_v^2 \exp(\theta_v / T_v)}{[\exp(\theta_v / T_v) - 1]^2} R$$

Or for simplicity,

$$k_{v,s} = \mu_s c_{v,vib,s} = \mu_s \frac{R\theta_{v,s}}{T_v [\exp(\theta_{v,s} / T_v) - 1]}$$

In the Svehla's work [47], specific heat, viscosity, and thermal conductivity of each gas species are tabulated along the temperature from 100 to 5,000 K in 100 degrees intervals. Vibrational conductivity was calculated in the same way as those of Blottner's curve fit.

References

- [1] DiCRISTINA, V., and RICHARDS, B., "Heat Transfer Studies on Ablation Protected Nosedtips at Reentry Simulated Conditions," *12th Thermophysics Conference*. 1977, p. 781.
- [2] Hsing, Y., Chang, M., Wu, S., and Kuo, J., "Experimental Determination of the Ablation Rate of a Blunt-Wedge in Gas Particle Nozzle Flow," *AIAA, SAE, ASME, and ASEE, 27th Joint Propulsion Conference*. 1991.
- [3] Chiang, T. L., HOFFMANN, K., and Siddiqui, M., "Analysis of Nosedtip Recession of the Tungsten Projectiles in Hypersonic Flight," *AIAA, Aerospace Sciences Meeting & Exhibit*, 8p. 1993.
- [4] Havstad, M., and Carter, P., "Thermo-Chemical Ablation During Reentrant and High Altitude Skipping Flight," *AIAA Paper*, 2000, pp. 01-0979
- [5] Bazylev, B., and Wuerz, H., "Melt Layer Erosion of Metallic Armour Targets During Off-Normal Events in Tokamaks," *Journal of nuclear materials*, Vol. 307, 2002, pp. 69-73
- [6] Thakre, P., and Yang, V., "Chemical Erosion of Refractory-Metal Nozzle Inserts in Solid-Propellant Rocket Motors," *Journal of Propulsion and Power*, Vol. 25, No. 1, 2009, pp. 40-50
- [7] Auerbach, I., "Ablation Performance of Tungsten, Copper-Infiltrated Tungsten and Other Metal Systems in Arc Heated Jets," *15th Aerospace Sciences Meeting*. 1977, p. 239. doi: 10.2514/6.1977-239
- [8] Moody, H., Smith, D., Haddock, R., and Dunn, S., "Tungsten and Molybdenum Ablation Modeling for Reentry Applications," *Proc. 13th AIAA Aerospace Sciences Meeting*. 1975.
- [9] Moody, H., Smith, D., Haddock, R., and Dunn, S., "Tungsten and Molybdenum Ablation Modeling for Re-Entry Applications," *Journal of Spacecraft and Rockets*, Vol. 13, No. 12, 1976, pp. 746-753. doi: 10.2514/6.1975-112
- [10] Sherman, M., and Schutzler, J., "Design Development of Segmented Tungsten Nosedtips for High Performance Flight Vehicles," *12th Thermophysics Conference*. 1977, p. 789. doi: 10.2514/6.1977-789
- [11] Kim, H., Oh, P., Kang, B., Lim, H., Moon, S., and Hong, B., "Ablation Properties of Plasma Facing Materials Using Thermal Plasmas," *Fusion Engineering and Design*, Vol. 124, 2017, pp. 460-463
- [12] ETEMAD, G., and HOLLY, D., "The Oxidation and Mechanical Performance of Tungsten at High Temperatures and High Pressures(Oxidation and Mechanical Performance of Tungsten and Composite Tungsten Systems at High Temperatures and Pressures, Determining Surface Recession Rate up to 6750 Degrees R)," 1965,
- [13] Guo, L.-j., Peng, J., Guo, C., Huo, C.-x., Sun, R.-j., and Zhang, Y.-x., "Ablation Performance of Supersonic Atmosphere Plasma Sprayed Tungsten Coating under Oxyacetylene Torch and Plasma Torch," *Vacuum*, Vol. 143, 2017, pp.

- [14] Lee, D., Umer, M. A., Ryu, H. J., and Hong, S. H., "Elevated Temperature Ablation Resistance of Hfc Particle-Reinforced Tungsten Composites," *International Journal of Refractory Metals and Hard Materials*, Vol. 43, 2014, pp. 89-93
- [15] Umer, M. A., Lee, D., Ryu, H. J., and Hong, S. H., "High Temperature Ablation Resistance of Zrnp Reinforced W Matrix Composites," *International Journal of Refractory Metals and Hard Materials*, Vol. 42, 2014, pp. 17-22
- [16] Wang, D., Wang, Y., Wei, B., Huo, S., Song, G., and Zhou, Y., "Effect of W Content on the Ablation Properties of W-Zrc Composites Synthesized by Reactive Melt Infiltration under Oxyacetylene Flame," *International Journal of Refractory Metals and Hard Materials*, Vol. 74, 2018, pp. 28-39
- [17] Kim, M., Kim, S., Kang, J., Song, S. H., and Lee, D., "Effects of Zrn and W Particle Sizes on the Mechanical and Ablation Properties of Zrn/W Composites," *Metals and Materials International*, Vol. 25, No. 3, 2019, pp. 733-739
- [18] Song, G., Wang, Y., and Zhou, Y., "Elevated Temperature Ablation Resistance and Thermophysical Properties of Tungsten Matrix Composites Reinforced with Zrc Particles," *Journal of Materials Science*, Vol. 36, No. 19, 2001, pp. 4625-4631
- [19] Natali, M., Kenny, J. M., and Torre, L., "Science and Technology of Polymeric Ablative Materials for Thermal Protection Systems and Propulsion Devices: A Review," *Progress in Materials Science*, Vol. 84, 2016, pp. 192-275
- [20] Batty, J., and Stickney, R., "Quasiequilibrium Treatment of Gas-Solid Reactions. I. Evaporation Rates of Volatile Species Formed in the Reaction of O₂ with W, Mo, and C," *The Journal of Chemical Physics*, Vol. 51, No. 10, 1969, pp. 4475-4484
- [21] Batty, J., and Stickney, R., "Quasiequilibrium Treatment of Gas-Solid Reactions. Iii. Rate of Volatilization of Tungsten by High-Temperature Oxidation," *Oxidation of Metals*, Vol. 3, No. 4, 1971, pp. 331-355. doi: 10.1007/bf00614627
- [22] Harvey, F., "High Temperature Oxidation of Tungsten Wires in O₂-Ar Mixtures," *Metallurgical Transactions*, Vol. 4, No. 6, 1973, pp. 1513-1517
- [23] Sabourin, J. L., and Yetter, R. A., "High-Temperature Heterogeneous Reaction Kinetics of Tungsten Oxidation by Co₂, Co, and O₂," *Journal of Propulsion and Power*, Vol. 25, No. 2, 2009, p. 490. doi: 10.2514/1.38123
- [24] Sabourin, J. L., and Yetter, R. A., "Kinetic Mechanisms of High Temperature Tungsten Oxidation: Experimental Evaluation with Modeling," *45th AIAA/ASME/SAE/ASEE Joint Propulsion Conference & Exhibit*, 2009, p. 5272.
- [25] Sabourin, J. L., and Yetter, R. A., "High-Temperature Oxidation Kinetics of Tungsten-Water Reaction with Hydrogen Inhibition," *Journal of Propulsion and Power*, Vol. 27, No. 5, 2011, pp. 1088-1096
- [26] Gulbransen, E., and Andrew, K., "Kinetics of the Oxidation of Pure Tungsten from 500 to 1300 C," *Journal of the Electrochemical Society*, Vol. 107, No. 7,

1960, pp. 619-628

- [27] Gulbransen, E., Andrew, K., and Brassart, F., "Oxidation of Graphite, Molybdenum and Tungsten at 1000 to 1600 C," *Preprint*, No. 63-493, 1964,
- [28] Olcott, E. L., and Batchelor, J., "Failure Mechanisms in Dense Tungsten Alloy Rocket Nozzles," *Journal of Spacecraft and Rockets*, Vol. 1, No. 6, 1964, pp. 635-642
- [29] Zubler, E., "Kinetics of the Tungsten-Oxygen-Hydrogen Bromide Reaction," *The Journal of Physical Chemistry*, Vol. 79, No. 16, 1975, pp. 1703-1706
- [30] Gilbert, L. M., "Hypersonic, Diffusion-Controlled Oxidation of Tungsten," *Thermal Design Principles of Spacecraft and Entry Bodies*, 1969, p. 249
- [31] Fay, J. A., "Theory of Stagnation Point Heat Transfer in Dissociated Air," *Journal of the Aerospace Sciences*, Vol. 25, No. 2, 1958, pp. 73-85.doi: 10.2514/8.7517
- [32] Brune, A. J., Bruce III, W. E., Glass, D. E., and Splinter, S. C., "Computational Predictions of the Hypersonic Material Environmental Test System Arcjet Facility," *Journal of Thermophysics and Heat Transfer*, Vol. 33, No. 1, 2018, pp. 199-209
- [33] Na, J. J., and Lee, J. M., "Determination of Enthalpy in the 150kw Arc-Jet," *Journal of the Korean Society for Aeronautical & Space Sciences*, Vol. 41, No. 7, 2013, pp. 547-551
- [34] Winovich, W., *On the Equilibrium Sonic-Flow Method for Evaluating Electric-Arc Air-Heater Performance*: National Aeronautics and Space Administration, 1964.
- [35] Sutton, K., and Gnoffo, P., "Multi-Component Diffusion with Application to Computational Aerothermodynamics," *7th AIAA/ASME Joint Thermophysics and Heat Transfer Conference*. 1998, p. 2575.
- [36] Gosse, R., and Candler, G., "Diffusion Flux Modeling: Application to Direct Entry Problems," *43rd AIAA Aerospace Sciences Meeting and Exhibit*. 2005, p. 389.
- [37] Park, C., "Review of Chemical-Kinetic Problems of Future Nasa Missions. I- Earth Entries," *Journal of Thermophysics and Heat transfer*, Vol. 7, No. 3, 1993, pp. 385-398
- [38] Park, C., "Assessment of a Two-Temperature Kinetic Model for Dissociating and Weakly Ionizing Nitrogen," *Journal of Thermophysics and Heat Transfer*, Vol. 2, No. 1, 1988, pp. 8-16
- [39] Park, C., "Assessment of Two-Temperature Kinetic Model for Ionizing Air," *Journal of Thermophysics and Heat Transfer*, Vol. 3, No. 3, 1989, pp. 233-244.doi: 10.2514/3.28771
- [40] Park, C., "A Review of Reaction Rates in High Temperature Air," *24th Thermophysics Conference*. 1989, p. 1740.
- [41] Park, C., and Yoon, S., "Calculation of Real-Gas Effects on Blunt-Body Trim Angles," *AIAA journal*, Vol. 30, No. 4, 1992, pp. 999-1007

- [42] Park, C., Howe, J. T., Jaffe, R. L., and Candler, G. V., "Review of Chemical-Kinetic Problems of Future Nasa Missions. Ii-Mars Entries," *Journal of Thermophysics and Heat transfer*, Vol. 8, No. 1, 1994, pp. 9-23
- [43] Gupta, R. N., Yos, J. M., Thompson, R. A., and Lee, K.-P., "A Review of Reaction Rates and Thermodynamic and Transport Properties for an 11-Species Air Model for Chemical and Thermal Nonequilibrium Calculations to 30000 K," *NASA STI/Recon Technical Report N*, Vol. 90, 1990,
- [44] Millikan, R. C., and White, D. R., "Systematics of Vibrational Relaxation," *The Journal of chemical physics*, Vol. 39, No. 12, 1963, pp. 3209-3213
- [45] Wilke, C., "A Viscosity Equation for Gas Mixtures," *The journal of chemical physics*, Vol. 18, No. 4, 1950, pp. 517-519. doi: 10.1063/1.1747673
- [46] Blottner, F. G., Johnson, M., and Ellis, M., "Chemically Reacting Viscous Flow Program for Multi-Component Gas Mixtures." Sandia Labs., Albuquerque, N. Mex., 1971.
- [47] Svehla, R. A., "Estimated Viscosities and Thermal Conductivities of Gases at High Temperatures," 1962,
- [48] Svehla, R. A., *Transport Coefficients for the Nasa Lewis Chemical Equilibrium Program*: National Aeronautics and Space Administration, Office of Management, Scientific and Technical Information Program, 1995.
- [49] Chase, M. W., "Janaf Thermochemical Tables," *JANAF thermochemical tables, by Chase, MW Washington, DC: American Chemical Society; New York: American Institute of Physics for the National Bureau of Standards, c1986.. United States. National Bureau of Standards.*, Vol. 1, 1986,
- [50] Jameson, A., "Time Dependent Calculations Using Multigrid, with Applications to Unsteady Flows Past Airfoils and Wings," *10th Computational Fluid Dynamics Conference*. 1991, p. 1596.
- [51] Yoon, S., and Jameson, A., "Lower-Upper Symmetric-Gauss-Seidel Method for the Euler and Navier-Stokes Equations," *AIAA journal*, Vol. 26, No. 9, 1988, pp. 1025-1026. doi: 10.2514/3.10007
- [52] Kim, K. H., Kim, C., and Rho, O.-H., "Methods for the Accurate Computations of Hypersonic Flows: I. Ausmpw+ Scheme," *Journal of Computational Physics*, Vol. 174, No. 1, 2001, pp. 38-80. doi: 10.1006/jcph.2001.6873
- [53] Kim, K. H., Kim, C., and Rho, O. H., "Accurate Computations of Hypersonic Flows Using Ausmpw+ Scheme and Shock-Aligned Grid Technique," *AIAA Paper*, 1998, pp. 98-2442
- [54] Kim, K. H., and Kim, C., "Accurate, Efficient and Monotonic Numerical Methods for Multi-Dimensional Compressible Flows: Part I: Spatial Discretization," *Journal of Computational Physics*, Vol. 208, No. 2, 2005, pp. 527-569. doi: <http://dx.doi.org/10.1016/j.jcp.2005.02.021>
- [55] Kim, K. H., and Kim, C., "Accurate, Efficient and Monotonic Numerical Methods for Multi-Dimensional Compressible Flows: Part Ii: Multi-Dimensional Limiting Process," *Journal of Computational Physics*, Vol. 208, No. 2, 2005, pp. 570-615

- [56] Kim, K. H., Kim, C., and Rho, O.-H., "Methods for the Accurate Computations of Hypersonic Flows: Ii. Shock-Aligned Grid Technique," *Journal of Computational Physics*, Vol. 174, No. 1, 2001, pp. 81-119.doi: 10.1006/jcph.2001.6896
- [57] Anderson Jr, J. D., *Hypersonic and High-Temperature Gas Dynamics*: American Institute of Aeronautics and Astronautics, 2006.
- [58] Gokcen, T., "Effects of Freestream Nonequilibrium on Convective Heat Transfer to a Blunt Body," *Journal of thermophysics and heat transfer*, Vol. 10, No. 2, 1996, pp. 234-241
- [59] Suzuki, T., Sakai, T., and Yamada, T., "Calculation of Thermal Response of Ablator under Arcjet Flow Condition," *Journal of thermophysics and heat transfer*, Vol. 21, No. 2, 2007, pp. 257-266
- [60] Gordon, S., and McBride, B. J., "Computer Program for Calculation of Complex Chemical Equilibrium Compositions and Applications. Part 1: Analysis," 1994,
- [61] Park, C., *Nonequilibrium Hypersonic Aerothermodynamics*. New York: John Wiley and Sons, 1989.
- [62] Vincenti, W. G., and Kruger, C. H., *Introduction to Physical Gas Dynamics*: Wiley New York, 1965.

국문초록

극초음속 비행이나 로켓 노즐과 같은 고온 환경, 특히 산화가 주 삭마 메커니즘으로 작용하는 환경에서 순수 텅스텐과 강화재가 첨가된 텅스텐 복합재의 삭마 모델 개발을 위하여, 150-kW 아크 히터를 이용해 삭마 실험을 수행하였다.

순수 텅스텐에 대해 총 10 가지 다른 유동조건에서 실험하였으며, 실험 전후 질량 및 길이 변화를 측정하였다. 고속 카메라를 이용하여 실험과정에서 삭마에 의한 시편의 형상변화를 촬영하였으며, 이를 통해 시간에 대한 길이 삭마량을 계산하였다.

텅스텐 복합재 시편에는 하프늄 카바이드와 지르코늄 카바이드가 강화재로 사용되었다. 동일한 실험 조건에서 각각 다양한 조성을 갖는 텅스텐-하프늄 카바이드, 텅스텐-지르코늄 카바이드 시편에 대한 실험을 수행하였으며, 강화재 함량의 증가에 따른 내삭마능 증가효과를 조사하였다.

실험에 사용된 아크히터의 제약조건들로 인해 실험에서 측정하지 못한 표면 열전달량과 화학종 질량분율을 계산하기 위해 축대칭 비평형 유동 솔버를 이용하여 실험조건에 대한 수치해석을 수행하였다. 또한, 수치 해석을 이용하여 실험 도중 시편의 위치나 반지름과 같은 시편 형상의 변화가 열전달량에 미치는 영향을 연구하였다. 그 결과, 시편의 형상변화만으로도 실험도중 정체점 열전달량이 35%까지 감소할 수 있음이 확인되었다.

최종적으로, 텅스텐에 대한 삭마 모델과 함께 비평형 유동 솔버와 고체 열해석 솔버를 결합한 삭마 해석 프로그램을 개발하였다. 개발된 프로그램은 정체점에 대한 삭마 속도뿐만 아니라 시간에 따른 시편의 형상변화까지도 훌륭히 모사하였다.

주요어: 텅스텐, 삭마, 산화, 아크히터, 전산해석

학번: 2012-30169

성명: 노성준